Investigating Sensorimotor Control in Locomotion using Robots and Mathematical Models

PAR

Robin THANDIACKAL

ÉCOLE POLYTECHNIQUE
FÉDÉRALE DE LAUSANNE

Suisse
2017

Is this orange juice?
— some people will remember

In honour of past memories, mostly the good ones …

Acknowledgements

At this point, I would like to express my deepest gratitude to all the people who made this journey possible.

First and foremost, I thank Professor Auke Ijspeert for giving me the opportunity to work on so many interesting questions in the greatest of all Labs, the Biorobotics Laboratory in Lausanne. I have always appreciated his advice and his extraordinary ideas. His ways of interacting with people and teaching them in very subtle but profound ways have deeply impressed me, I learned a lot! I also thank him for being a great leader of the lab, scientifically and socially. I enjoyed our many lunch runs and all the lab events.

A long-term project like a doctoral thesis is only achievable if the corresponding funding resources are available. Therefore, I would also like to thank EPFL and the Swiss National Science Foundation for financial support.

I thank all our scientific collaborators, Akio Ishiguro, Takeshi Kano, Dimitri Ryczko and Jean-Marie Cabelguen, for many valuable discussions and inputs in the different projects. A special thanks goes to Pavan Ramdya, whose straight-to-the-point thinking I highly admire, and whose initiative has led us to a great project with very interesting outcomes.

I believe it is important that the supervision and guidance of PhD students involves not only Professors but also the experienced members of a research group. Fortunately, it was also the case for me and my mentors in this sense were namely, Kamilo Melo, Kostas Karakasiliotis and in the last year also Behzad Bayat. I very much appreciated their research related and non-research related advice and all the valuable lessons learned.

The time in Biorob has been profoundly gratifying. The topics on the one hand but especially the clever, competent, and highly knowledgeable people in the Lab made this possible. I would like to thank therefore all the current and previous lab members for a great experience. I'm afraid at this point to forget someone and will therefore not mention all you guys by name! Nonetheless, I specially thank Tomislav, who I worked with almost since the beginning. He has always been a great office mate and friend. Special thanks goes also to Ale for literally "*all*" the lab related things and his help in all the projects, Peter for his helpful mind, Simon for all the great dinner and board game evenings and Mehmet for his genuinely happy spirit.

Besides all the work related aspects, I would also thank my dear friends who supported me during all the time at EPFL. Sport has always been of great importance in my life, which is why

Acknowledgements

I'm thankful to all the friends in our football club in St.Gallen and our running team in the Lab. I specially thank Maurus and Davud for their advice and open ears, and of course Steve for all his enthusiasm in so many aspects.

I would like to thank Anni for all her love and support, and the great time we had and have together. Finally, I'm grateful for all the support from my parents, who encouraged me to be persistent and work hard.
Last but not least, little brother, I thank you for your help, for your cleverness, for football, for having fun, and foremost at any time for your honesty. Thanks Kevin!

Lausanne, 10th February 2017   R. T.

Abstract

Locomotion is a very diverse phenomenon that results from the interactions of a body and its environment and enables a body to move from one position to another. Underlying control principles rely among others on the generation of intrinsic body movements, adaptation and synchronization of those movements with the environment, and the generation of respective reaction forces that induce locomotion. We use mathematical and physical models, namely robots, to investigate how movement patterns emerge in a specific environment, and to what extent central and peripheral mechanisms contribute to movement generation. We explore insect walking, undulatory swimming and bimodal terrestrial and aquatic locomotion. We present relevant findings that explain the prevalence of tripod gaits for fast climbing based on the outcome of an optimization procedure. We also developed new control paradigms based on local sensory pressure feedback for anguilliform swimming, which include oscillator-free and decoupled control schemes, and a new design methodology to create physical models for locomotion investigation based on a salamander-like robot. The presented work includes additional relevant contributions to robotics, specifically a new fast dynamically stable walking gait for hexapedal robots and a decentralized scheme for highly modular control of lamprey-like undulatory swimming robots.

Key words: insect walking, swimming, local sensory feedback, decentralized control, bimodal locomotion, robotics

Zusammenfassung

Lokomotion ist ein sehr variantenreiches Phänomen, dass hauptsächlich aus Interaktionen eines Körpers mit seiner Umwelt resultiert und es erlaubt sich von einem Ort an den nächsten fortzubewegen. Die zugrunde liegenden Kontrollmechanismen beinhalten verschiedene Aspekte, wie die Erzeugung von wesentlichen Körperbewegungen, die Anpassung und Synchronisierung dieser Bewegungen mit der Umwelt und schlussendlich die Erzeugung von entsprechenden Reaktionskräften, welche Lokomotion induzieren. Wir benutzen mathematische und physikalische Modelle, im Speziellen Roboter, um zu untersuchen wie sich Bewegungsmuster in spezifischen Umgebungen ergeben und zu welchem Grad zentrale und periphere Mechanismen zur Bewegungsentstehung beitragen. Wir untersuchen Laufmuster in Insekten, undulierendes Schwimmen und bimodal terrestrisch-aquatische Lokomotion. In diesem Kontext präsentieren wir relevante Erkenntnisse, die die Vorherrschaft von Tripod Laufmustern für schnelles Klettern basierend auf den Resultaten einer Optimierungsprozedur erklären. Des Weiteren stellen wir neue Kontrollparadigmen vor für anguilliformes Schwimmmen, welche, basierend auf lokaler Druck-Sensorrückführung, Oszillator-freie und entkoppelte Kontrollschemen beinhalten. Letztendlich schlagen wir eine neue Designmethodologie zur Entwicklung von physikalischen Modellen zur Untersuchung von Lokomotion am Beispiel eines salamanderähnlichen Roboters vor. Die Arbeit beinhaltet zusätzlich relevante Beiträge zur Robotik mit Thesen für eine neuartige dynamisch stabile Gangart für sechsbeinige Roboter und ein dezentrales Schema für hochmodulare Kontrolle von undulierenden Schwimmrobotern.

Stichwörter: Insekten-Laufmuster, Schwimmen, lokale Sensorrückführung, Dezentrale Kontrolle, Bimodale Lokomotion, Robotik

Résumé

La locomotion est un phénomène très varié qui apparaît suite aux interactions d'un corps avec son environnement, lui permettant ainsi de se déplacer d'un point à un autre. Les principes de contrôle sous-jacents se basent entre autre sur la génération des mouvements intrinsèques du corps, sur l'adaptation et la synchronisation de ces mouvements avec l'environnement, ainsi que sur la production des forces de réaction qui induisent la locomotion. On utilise des modèles mathématiques et physiques, implémentés en tant que robots, pour examiner comment des séquences de mouvements émergent dans un environnement spécifique, et en quelle mesure les mécanismes de contrôle centraux et périphériques contribuent à engendrer le mouvement. On explore la marche des insectes, la nage ondulatoire, ainsi que la locomotion bimodale amphibie. On présente des résultats pertinents qui expliquent la prévalence des démarches tripodes pour la grimpe rapide, sur la base du résultat d'un processus d'optimisation. On a également développé de nouveaux paradigmes de contrôle pour la nage anguilliforme basés sur un feedback sensoriel local de la pression, incluant des schémas de contrôle sans oscillateur ni couplage ; ainsi qu'une nouvelle méthode de conception, basée sur un robot salamandre, pour la création de modèles physiques destinés à l'analyse de la locomotion. Le travail présenté inclut d'autres contributions au domaine de la robotique, en particulier un nouveau type de marche rapide dynamiquement stable pour robots hexapodes, ainsi qu'un schéma de contrôle décentralisé hautement modulaire utilisable avec des robots à nage ondulatoire de type lamproie.

Mots clefs : marche des insectes, nage, feedback sensoriel local, contrôle décentralisé, locomotion bimodale, robotique

Contents

Contents

List of Figures

List of Tables

Introduction

What appears to be the beginning of this thesis is at the same time the end of a very enjoyable journey. This document is the last piece of this journey which I like to see as a way to share my thoughts and insights that have developed over the last four and a half years in our unique Laboratory at EPFL in Lausanne and in collaboration with many people all around the world. If I had to frame the topic of the presented work here at day one of the project, I would probably have said, it settles around *learning about locomotion in animals and the transfer to engineering systems.* Today I'll say the same but I'll add *... and vice versa* at the end, as it has been a very valuable experience to use our engineering tools to pursue questions of why things behave as they do. Thus, please let me put this short comment and say that based on my, of course personally biased, exposure to related questions and the consequent quest for answers, I encourage anyone to apply their engineering expertise also in interdisciplinary fields. For me, this challenge to work in different subjects and with people from different fields has been very rewarding! Now that this is said, let me introduce you to the general topic of this thesis.

Locomotion, simulated Creatures and Newton

Let us start with a tale, where for almost a century, starting with Johannes Schmidt (1923), researchers have been investigating what could be called the *Eel mystery*. It described the paradox that in their larval stages the American and European Eel are located in the Sargasso sea (mid North Atlantic). However, as adults they live far far away along the North American and European coast and had never been observed migrating to the open sea or their spawning region. It was estimated that for a migration process of this kind the eels had to swim thousands of kilometers in a relatively short amount of time. Researchers collected more and more evidence to prove this, and in a breakthrough a team (Ginneken et al., 2005) was able to show under laboratory conditions in flow tanks that those eels have the capability to cover distances of about 5500 km within 173 days. As if this was not impressive enough, these eels were able to achieve this in a fasting state. A few years later this was validated by another team (Béguer-Pon et al., 2015) which was finally able to track a group of eels of which one individual migrated traveling a distance of 2400 km in a bit more than 45 days. Given their relatively small size of around 70 cm this would correspond to an average swimming speed of 0.55 body lengths per

second. This is an extraordinary achievement and one can hardly imagine the impact of a similarly efficient artificial swimming machine.

But nevertheless, the example of the eel is only one of many that shows how organisms are able to extract the most out of their bodies to excel in their specific living environment with optimal locomotion strategies. In the case of the eel, its specific style of swimming by propagating traveling waves of undulations from head to tail turns out to be very energy efficient. Other fish, although in the same aquatic environment as the eel, like e.g. the trout, use more of a tail-based propulsion, which results in different characteristic abilities such as maximally achievable speeds, maneuverability, etc (Sfakiotakis et al., 1999). Other aquatic animals have completely different locomotion strategies, such as the jellyfish, which uses almost a jet-like propulsion to navigate in water (Gemmell et al., 2015). In other environments the locomotor patterns change even further. Flapping wing birds, running horses, crawling snakes and hopping kangaroos are just a few to mention. The important point to make is that in general, animals in their respective environments have found adapted locomotor strategies for their specific body morphologies, which both have been developed and improved over the course of evolution.

It is both difficult, yet intriguing, to reason what the underlying principles of specific loco-motion control for certain morphologies and corresponding environments are. Traditionally biologists, neuroscientists, functional morphologists and biomechanists have been studying animal locomotion in a variety of (controlled) experiments. For this purpose, usually detailed measurements regarding generated dynamics (e.g. ground reaction forces) and kinematic patterns (e.g. motion capture techniques) are extracted and then related to the nervous system and the muscle apparatus (e.g. electromyography). Following this methodology, locomotion-relevant control strategies have been identified in many organisms. In this thesis, we combine traditional methods, with engineering tools as suggested among others by Ijspeert (2014): Animal locomotion control is investigated by mathematical models and by means of physical robotic models. The idea hereby is to develop or test control strategies in artificial animal bodies. This offers us additional key insights as we are able to explore and vary relevant parameters (e.g. neural connectivity, influence of sensory pathways, change in environment, etc.) and observe their effects on the locomotion. Moreover, measurements to characterize locomotion performance, e.g. energy consumption, are often much easier to extract from these artificially designed systems.

To develop models of locomotion control, many approaches have been proposed over the last years. Locomotion is generated by means of a variety of dedicated subsystems such as the nervous system, clever mechanical body properties, muscle actuation and sensors. Our focus is however less pointed on the detailed reconstruction and reproduction of each of those subsystems, but rather on higher level interaction mechanisms between the relevant subsystems and the resulting features for locomotion. As mentioned before, the environment constrains locomotor strategies to a great extent, which is why we are especially interested to analyze how gait patterns are specifically shaped by environmental influences. A key aspect in

our work is therefore to investigate *emergent* locomotor behavior in animals. Probably, one of the first to promote related ideas was Karl Sims (1994), who looked at the *emergence* of behavior and morphology in computer simulated creatures. By introducing a competitive selection criterion within an optimization procedure, he was able to evolve structures which were able to locomote in various environments using different morphologies. In this sense, the concept of *emergence* relates to the idea of letting a system evolve until a movement pattern is established. How the system evolves is highly variable and can be realized in different ways (e.g. goal-directed rules). Important is the ultimate goal to identify key components which inherently lead to locomotion as a result of the interplay between body movement and environment. Subsequently, this can help us to understand the essential underlying principles that explain why and how animals with their specific bodies locomote in their natural environment. Learning these principles will further be useful to design efficient machines and robots for locomotion in dedicated environments, but might also enable insight to evolutionary developments and why some locomotion strategies proved to be more efficient than others, especially over the course of changing environmental conditions.

Locomotion is the result of the interaction between a body and its environment. To investigate possible underlying control mechanisms it is required to identify the relevant physical principles that let a body move from one point to another. It turns out that animals and locomotor systems in general exploit Newton's third law: *For every action, there is an equal and opposite reaction.* Thus, systems that propel themselves will try to generate reaction forces in their respective environment. When these reaction forces are generated in a coordinated fashion, a non-zero resulting external force will cause the system to locomote. Depending on the environment, the types of forces will highly differ and can span a wide spectrum from aerodynamic drag for flying animals, friction forces for terrestrial runners, up to adhesive forces for climbers. All animals rely on asymmetry to achieve efficient locomotion patterns. Although, it is often not evident in symmetric or periodic movement patterns, such as flapping wing birds or crawling snakes, the key is to generate asymmetric reaction forces with respect to the desired movement direction. To improve our understanding of locomotor control in different environments, analyzing these physical interaction mechanisms is important to determine desired reaction forces and their implications for coordinating body movements. Additionally, the relevant physical interaction forces need to be known to model and simulate possible control strategies in corresponding environments.

Tightly coupled to the importance of body-environment interaction for locomotion control is the ability to generate cyclic movements with the body, which could be seen as an *analogon to the wheel in nature*. The spinal cord in vertebrates plays hereby a very dedicated role. Whereas, high-level centers such as the motor cortex combine visual information and direct overall locomotion in terms of speed, direction and navigation in general, low-level centers in the spinal cord are mainly responsible for periodic locomotion patterns. In many animals, the existence of distributed local *Central Pattern Generators (CPGs)* is well-known. These CPGs represent neuron populations that are able to produce spontaneous rhythmic outputs for other interneurons and motoneurons, which in the end coordinate muscle contractions and the consequent

movements. While movement generation itself is a prerequisite for locomotion, adaptation depending on environmental conditions is crucial for it to be efficient. In this context, sensors provide information about generated reaction forces with the environment and movement patterns can be adjusted accordingly. These feedback mechanisms often act locally which in many organisms help to react quickly to environmental changes. Rather than conducting the sensory information all the way back to the brain and back to the point of interaction, sensory information is processed in local reflex-loops in the spinal cord. Examples of such reflex behaviors are for instance stumbling corrective reflexes (Forssberg, 1979) in cats that almost instantaneously correct leg motion when an unexpected obstacle is encountered. Thus, sensory feedback loops are arguably beneficial to coordinate and adapt locomotion patterns. As we will see further in the text, movement can also be purely generated based on sensory driven cues, as it has been already shown in other work on human locomotion (Geyer and Herr, 2010) and invertebrates (Fischer et al., 2001). We will also encounter questions related to peripheral vs central control mechanisms for movement generation and coordination.

In summary, locomotion enables great performances in various types of environments. It is a very complex process that involves many components that interact with each other. A few pivotal mechanisms can be identified and therefore, we propose the following key aspects that are of great importance:

> ► *The reaction forces between the body and the immediate environment.*

> ► *The inherent generation of movements in the body.*

> ► *The adaptation and synchronization of body movements with the environment.*

Throughout this work we create and use mathematical and physical models, in order to explore questions related to these key facets of locomotion in different environments and for different body morphologies. We analyze insect walking by means of the fruit fly which is a widely used model organism for six-legged locomotion. Furthermore, at a more macroscopic scale, we look at undulatory swimming in aquatic environments and create models that are relevant for invertebrate (e.g. leech) as well as vertebrate (e.g. lamprey or eel) organisms. Finally, salamander locomotion in a bimodal terrestrial and aquatic environment is analyzed.

Our general approach follows the idea to capture the most relevant aspects of specific analyzed locomotion and develop models that are as simple as possible, though still capable to describe the important causes and mechanisms that render it feasible.

Thesis Organization and Main Contributions

The thesis is structured in three main chapters, where each of which covers a few locomotion-relevant questions in specific environments. A final chapter discusses the overall findings and draws conclusions for future work.

Chapter 1 explores insect locomotion in different environments such as adhesive surfaces and vertical walls. In-silico optimizations in simulations and robot experiments led us to possible explanations for the prevalence of tripod gaits in insects as well as to possibly more efficient locomotor strategies for six-legged robots.

Chapter 2 investigates local sensory feedback based undulatory locomotion in aquatic environments. Simulations with an elongated lamprey-like swimming model revealed feedback driven mechanisms for the generation of oscillatory body bending as well as for the establishment of coordinated swimming patterns.

Chapter 3 analyzes the proposition of a biomimetic robot design to be used in terrestrial as well as aquatic environments. Along with a design methodology, important considerations regarding scaling laws for proper reaction forces and their validation in experiments is provided.

Main Contributions

- We demonstrate that the tripod gait in insect walking satisfies the requirements of fast locomotion for climbing.
- We present a new dynamically stable bipod gait for hexapedal locomotion that is faster than the tripod gait.
- We show that *Drosophila* with blocked adhesion does not perform the tripod gait anymore, but a gait that features bipod-like characteristics.
- We show that local pressure feedback in undulatory swimming
    - can correct wrong CPG induced phase lags.
    - can coordinate and establish a traveling wave of body bending in a decoupled oscillatory network.
    - can generate rythms and traveling waves in combination with central coupling in the absence of neural oscillators.
- We propose a new design methodology with corresponding validation and analysis for a physical locomotion model by means of a salamander-like robot.

---

1 Insect Walking

Particularly in legged locomotion, very specific gait patterns adapted to specific environments and desired performance are present. It could enable us to create efficient legged locomotor machines and possibly give us insight in required control mechanisms if we understood which patterns should be used under which conditions. Therefore, we asked in this chapter how gait patterns should be selected for the case of six-legged systems. We studied insect locomotion and explored a variety of gaits in terms of variable inter-leg coordination. A corresponding insect model was created for this purpose along with a model of relevant reaction forces, such as friction, adhesion and gravitation, between the body and the ground. Based on these questions and the corresponding modeling approach we are able to present new findings explaining the prevalence of tripod gaits in insects as well as a new gait that can be used for fast locomotion in six-legged robots.

*The following sections are based on the newly published article "P. Ramdya, **R. Thandiackal*** *, R. Cherney, T. Asselborn, R. Benton, A. J. Ijspeert, D. Floreano. Climbing favours the tripod gait over alternative faster insect gaits. Nature Communications (2017)" in which I was co-lead author. Parts of the text and figures of the original paper have been reorganized in this chapter.*

My original contributions

- Work on the development of the *in silico* model
- Optimizations with the *in silico* model in different environments and different scales
- Analysis and evaluation of optimized gait patterns
- Helping to formulate research questions
- Inputs to the manuscript, in particular for the methods

1.1   Abstract

To escape danger or catch prey, running vertebrates rely on dynamic gaits with minimal ground contact. By contrast, most insects use a tripod gait with three legs on the ground. One prevailing hypothesis for this difference in fast locomotor strategies is that tripod locomotion allows insects to rapidly navigate three-dimensional terrain. To test this, we computationally discovered fast locomotor gaits for a model based on *Drosophila melanogaster*. Indeed, the tripod gait emerges to the exclusion of many other possible gaits when optimizing fast upward climbing with leg adhesion. By contrast, novel two-legged bipod gaits are fastest on flat terrain without adhesion in the model and in a hexapod robot. Intriguingly, when adhesive leg structures are covered in real *Drosophila*, animals exhibit atypical bipod-like leg coordination. We propose that the requirement to climb vertical terrain may drive the prevalence of the tripod gait over faster alternative gaits with minimal ground contact.

1.2 Introduction

Since the pioneering photographic studies of Eadweard Muybridge (1887), it has been widely appreciated that animals use distinct gaits at different locomotor speeds. These discontinuous shifts in leg coordination are hypothesized to minimize energy consumption by changing the number and relative timing of legs in motion (Hoyt and Taylor, 1981; Srinivasan and Ruina, 2005). For example, horses transition from a slow walk, lifting only one or two legs simultaneously, to a trot, canter, and, finally, a fast gallop that further reduces the number of legs on the ground at any one time (Hildebrand, 1965). Above a certain threshold speed most vertebrates use gaits that are characterized by having little to no ground contact during part of the stepping cycle and require dynamic stability to remain upright (Alexander, 2003).

Like vertebrates, insects also exhibit gait transitions as they increase locomotor speed although it is less clear to what extent these transitions are true gaits (Bender et al., 2011; Smolka et al., 2013), or continuous changes over walking speed (Graham, 1972; Bässler and Büschges, 1998; Schilling et al., 2013). For example, *Drosophila melanogaster*, a popular model for studying insect locomotion (Mendes et al., 2013; Wosnitza et al., 2013; Strauss and Heisenberg, 1990), transitions from a slow wave gait, to a tetrapod gait, and finally to a fast tripod gait (Mendes et al., 2013; Wosnitza et al., 2013; Strauss and Heisenberg, 1990; Wilson, 1966), always keeping at least five, four, or three legs on the ground at a given time, respectively. During tripod ground locomotion the front and rear legs on one side of the body move nearly synchronously with the middle leg on the other side. This tends to keep the animal's projected center of mass (COM) within a three-point polygon of support formed by the legs: a defining feature of static stability (Alexander, 2003). Therefore, in sharp contrast to fast vertebrate running gaits that have at most one or two feet in contact with the ground, an overwhelming majority of running insects do not reduce the number of legs on the ground below three. Importantly, this is not an inherent difference between hexapods and quadrupeds: in rare cases insects can have just two legs (Full and Tu, 1991), or no legs (Wahl et al., 2015) on the ground (i.e., flight phases) during tripod running. More commonly, to further increase ground locomotor speed, insects increase stride length, increase stride frequency, invoke spring-mass dynamics (Full and Tu, 1990), and reduce duty factors (Ting et al., 1994).

Fast gaits are critical for survival: they are used to hunt and to escape (Schaefer et al., 1994). Therefore, despite the capacity for other gaits (Smolka et al., 2013; Wosnitza et al., 2013), the ubiquity of the tripod gait across diverse insect species (Wilson, 1966) (e.g., flies (Wosnitza et al., 2013), ants (Zollikofer, 1994), stick insects (Graham, 1972), cockroaches (Goldman et al., 2006), and dung beetles (Smolka et al., 2013)) suggests that it has been subject to selection as a means for achieving fast locomotion. However, the factors - ethological, biomechanical, and/or developmental - causing the prevalence of this locomotor strategy over vertebrate-like gaits that minimize ground contact remain unknown. In nature, many small insects, including *Drosophila*, exhibit strong phototaxis and negative gravitaxis, compelling them to navigate and seek higher altitudes (Jander, 1963) by climbing up obstacles in their surroundings. Therefore, one long-standing but untested hypothesis for why the tripod gait is so pervasive is that

it allows insects to rapidly traverse challenging terrain, like vertically oriented vegetation, without falling off (Hughes, 1952; Reinhardt and Blickhan, 2014).

It is not yet possible to test this hypothesis by changing the gaits of real insects or by measuring the ancestral origins of extant locomotor behaviors. Therefore, computational approaches can be used to address experimentally intractable biological questions (Srinivasan and Ruina, 2005; Ackermann and Van den Bogert, 2012; Floreano and Keller, 2010; Ijspeert, 2014; Ijspeert et al., 2007; Wischmann et al., 2012). To investigate factors favoring the prevalence of the insect tripod gait, we discovered fast locomotor gaits for an *in silico* insect model using an optimization algorithm (Particle Swarm Optimization or PSO, Clerc and Kennedy 2002). Gaits can be characterized by their footfall patterns (e.g., tripod, or tetrapod), duty factors (above 0.5 for walking, or below 0.5 for running, Hildebrand 1965), and ground stability (static, or dynamic). Here we focused on footfall patterns since we were interested in understanding why insects rely on the tripod rather than alternative three-legged or even dynamically stable two-legged gaits during fast locomotion.

We find that the classic tripod gait is uniquely optimal for fast upward climbing using leg adhesion. It is also strongly favored during downward and sideways climbing. However, this is not due to adhesion alone: a variety of other gaits are also optimal for fast ground walking with leg adhesion. Furthermore, when optimizing for rapid ground locomotion in the absence of adhesion, novel dynamically stable two-legged gaits emerge. These bipod gaits are similar to the vertebrate running trot and are faster than the tripod gait in the insect model and in a hexapod robot. Intriguingly, when the structures subserving leg adhesion are blocked in real *Drosophila melanogaster*, flies abandon the tripod gait and instead exhibit atypical bipod-like leg coordination. These data suggest that the prevalence of tripod locomotion in insects – over faster, vertebrate-like gaits with minimal leg-substrate contact – is related to the requirement to climb three-dimensional surfaces using leg adhesion.

1.3 Gait optimization in an insect model

Our aim was to discover fast insect gaits for climbing, or for ground locomotion. Therefore, we designed a physics-based insect model but minimized its complexity to reduce the computational cost of gait optimization. Specifically, we used the simulation engine, Webots (Michel, 2004), to build a model based on the morphology and leg kinematics of *Drosophila melanogaster* (Fig. 1.1a-c and Fig. 1.2). To control each leg, instead of using complex neuromechanical methods (Beer and Gallagher, 1992; Daun-Gruhn and Büschges, 2011), we measured and reproduced periodic *Drosophila* leg motions during fast walking. In this way, we could isolate the contribution of gait on locomotor speed by varying the relative phases of motion of each leg while keeping stride frequency and foot trajectories fixed.

In our model, a vector of five numbers encodes a single gait: Each number represents a single leg's phase of motion relative to the left front leg which is fixed at 0° phase (Fig. 1.1b). For example, the simplest way to generate a tripod gait in our model is to fix the front left (θ_{L1}), middle right (θ_{R2}), and rear left (θ_{L3}) legs at a phase of 0° while the remaining three legs are set to 180°. The resulting gait has two power strokes per walking cycle (Fig. 1.1d) and can be characterized using a footfall or gait diagram that illustrates which legs are (stance) or are not (swing) in contact with the ground at each point in time (Fig. 1.1e). This gait produces ground reaction forces that rely on the front legs and, to some extent, the middle legs for propulsion (Supplementary Fig. A.1a; note that diverse mechanisms for propulsion have been observed across insect species (Reinhardt et al., 2009; Dallmann et al., 2016; Full et al., 1991)).

Notably, these phase lags are used for open loop control of our model. By contrast, insects are thought to depend on a distributed control mechanism whereby the movements of each leg depend on their phases relative to those of other segmental legs (e.g., hind leg movements take into account the current state of the middle legs) (Graham, 1972; Bässler and Büschges, 1998; Strauss and Heisenberg, 1990; Wilson, 1966; Hughes, 1952; Cruse, 1990; Cruse et al., 2007; Delcomyn, 2004). The advantage of our compressed method for encoding locomotor gaits with only five parameters is that it allows for a more rapid computational search for optimally fast gaits. Alternatively, if we had used existing neuromechanical insect models composed of many free parameters (Beer and Gallagher, 1992; Daun-Gruhn and Büschges, 2011; Szczecinski et al., 2014; Schmitz et al., 2001), the time for gait optimization would be have been prohibitively long, it would have been more difficult to analyze the data, and it would have been more challenging to extract general principles from the results.

During climbing, in addition to frictional forces, insects rely on adhesive forces (Mendes et al., 2014; Hüsken et al., 2015) generated by biomechanical specializations like claws and pulvilli on their legs (Goldman et al., 2006; Haas and Gorb, 2004; Federle et al., 2002). Frictional and adhesive forces differ in that they act in different directions – tangential and normal, respectively, to the contact surface – and therefore have different effects on the legs: friction reduces slipping while adhesive forces act against lift-off of the legs. Therefore, in addition to frictional forces, for some experiments we added a contact-dependent adhesion force to the

tips of the model's legs. The detailed physics of adhesion can vary depending on whether they originate from interlocking, capillary, or dry mechanisms, but at a higher level of abstraction these all generate normal forces that prevent the foot from lifting. Since different adhesion mechanisms for vertical climbing can be modeled using a common template (Goldman et al., 2006), we did not incorporate fine-scale physical mechanisms for adhesion and substrate-release into our model.

We optimized our insect model's gait for forward velocity, resulting in gaits that generate straight locomotion. Optimization for energy efficiency (via measurements of cost of transport), or using a different optimization method (genetic algorithm) yielded similar results. We began each optimization experiment by generating a population of fifty insect models with random gaits (i.e., random phases of motion for each leg). We then measured forward velocities for each model and used the fastest gaits – as well as the stochasticity inherent in PSO algorithms (Clerc and Kennedy, 2002) – to define gaits to be tested in the next iteration of the algorithm. In this way, each model's forward velocity steadily improved while the population's phase vectors converged over the course of 150 optimization iterations (Supplementary Fig. A.2). After each optimization experiment, we identified and studied the single fastest gait found over all iterations.
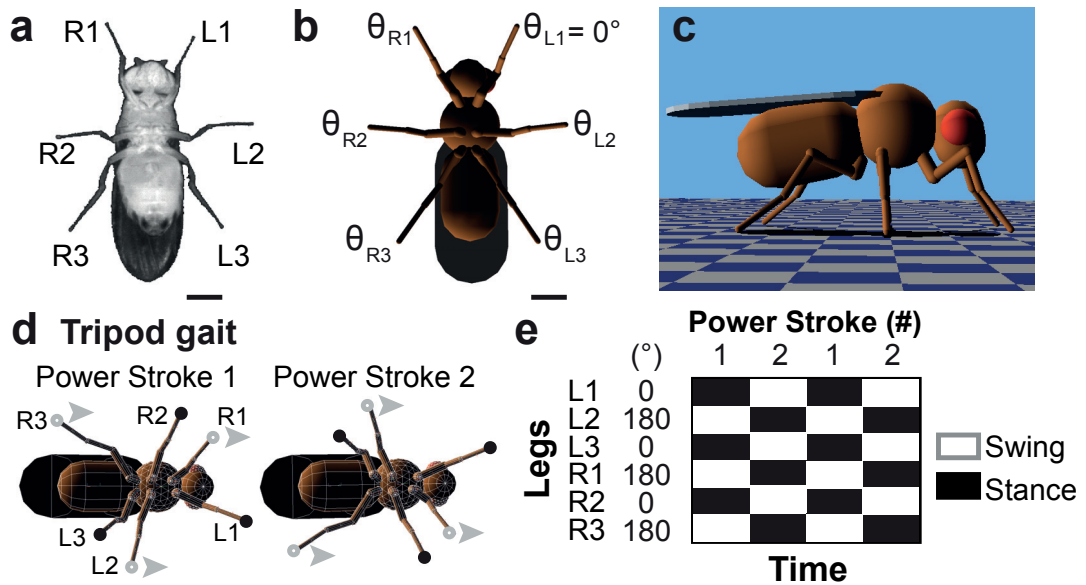
Figure 1.1 – **Gait optimization in an insect model**. **(a)** A ventral view of a *Drosophila melanogaster* female. Each leg is labeled as belonging to the right (R) or left (L) side and the prothoracic (1), mesothoracic (2), or metathoracic (3) leg pair. Scale bar is 0.4 mm. **(b)** A ventral view of the *in silico* insect model used in this study. A vector of five numbers encodes a single gait: each number represents a leg's phase of motion relative to the left front leg whose phase is fixed at 0°. Scale bar is 0.4 mm. **(c)** A side view of the insect model in its *in silico* environment. **(d)** The classic tripod gait has two power strokes per locomotor cycle. During each power stroke three legs are on the surface (stance phase, black circles) while the other three legs are off the surface (swing phase, grey circles). Grey arrowheads point in the direction of motion. **(e)** An idealized gait diagram of stance (black) and swing (white) phases for each leg during two cycles of tripod locomotion. The phase of motion for each leg is indicated. Each power stroke is numbered.

1.4 Methods

1.4.1 Insect model morphology

We designed an insect model using Webots 6.4.4 (Michel, 2004) (Cyberbotics Ltd., Lausanne Switzerland), a three-dimensional, physics simulation environment built on top of the Open Dynamics Engine (ODE). Using this software, solid geometric objects can be combined to build structures of arbitrary shape and actuated by simulated motors (see description below). We used Webots rather than a custom-designed physics engine and simulation environment to facilitate the reproduction and extension of our results by other researchers. To develop our model we combined published anatomical information (Soler et al., 2004; Sink, 2007) with microscope (Leica Microsystems, Wetzlar, Germany) images of 2 days post eclosion (dpe) awake and anaesthetized female *Drosophila melanogaster* of the Canton S background raised at 25°C. Since specimens were of variable size, we normalized measurements of each body and leg segment using the length of the thoracic segment as a reference (French et al., 1998). These values were then used to determine the size of our insect model. The mass of the model was also based on the average weight of 2 dpe *Drosophila* females (0.85mg). The head, thorax and abdomen of the model together comprise one rigid body. However, each component has its own homogeneous mass. This determines the mass and inertia of the rigid body as a whole. The head and abdomen are modeled as rigid capsules while the thorax is modeled as a rigid sphere. Each of the legs has six degrees of freedom (DOFs). Each DOF is implemented as a hinge joint. There are three hinge joints in series (i.e., overlaid joint axes) at the body-coxa junction, one hinge joint at the coxa-femur junction, one hinge joint at femur-tibia junction, and one hinge joint at tibia-tarsus junction. The segments of each leg are modeled as rigid capsules. The pretarsus, which is connected to the tarsus, is modeled as a rigid sphere. Fig. 1.2 shows an illustration of the model and the geometric dimensions of the body and the legs are given in tables 1.1 and 1.2.

Body part	Type	Diameter (mm)	Length (mm)	Thickness (mm)	Mass (mg)
Abdomen	Capsule	0.8925	0.595	-	0.0062
Thorax	Sphere	0.952	-	-	0.0124
Head	Capsules	0.595	0.1785	-	0.0124
Wing	Pill-shaped	1.19	1.2495	0.0595	$1.236 \cdot 10^{-5}$
Eye	Sphere	0.4165	-	-	(part of head)

Table 1.1 – Geometric dimensions of the insect model body

We also performed experiments with larger models (25 mm and 250 mm in length). For these models all dimensions were scaled up while keeping the density of each body part the same.

Body part	Type	Diameter (mm)	Length (mm)	Mass (mg)
Coxa	Capsule	0.1547;0.1547;0.1547	0.1547;0.0952;0.2737	0.0494
Trochanter/Femur	Capsule	0.1309;0.1309;0.1309	0.5653;0.5177;0.4879	0.0247
Tibia	Capsule	0.0952;0.0952;0.0952	0.5534;0.4879;0.4165	0.0247
Tarsus	Capsule	0.0714;0.0714;0.0714	0.6069;0.5415;0.5355	0.0247
Pretarsus	Sphere	0.1190;0.1190;0.1190	-;-;-	0.0124

Table 1.2 – Geometric dimensions of the insect model legs (hind/metathoracic; middle/mesothoracic; front/prothoracic)
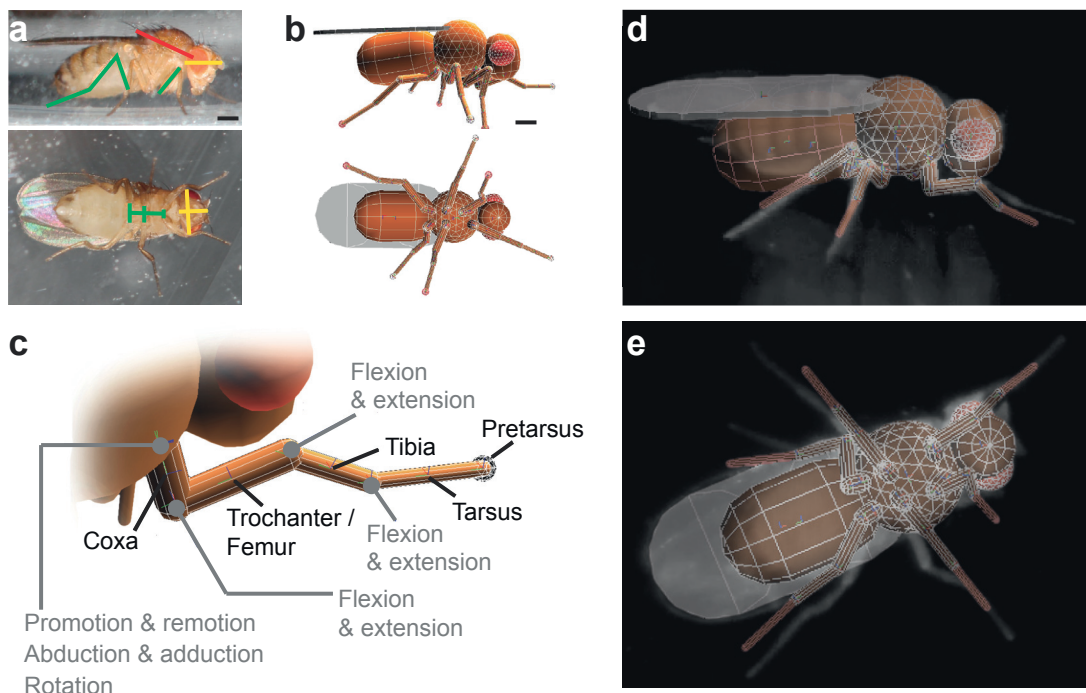
Figure 1.2 – **Insect model based on *Drosophila melanogaster*.** **(a)** Side and ventral images of adult female flies used to calculate the sizes of body and leg segments. Scale bar is 0.3 mm. Green, yellow, and red lines illustrate examples of leg, head, and thoracic measurements, respectively. **(b)** Corresponding side and ventral views of the insect model. Scale bar is 0.3 mm. **(c)** Image of the model's front right leg. Leg segments and the degrees of freedom for each joint are labeled in black and grey, respectively. **(d, e)** Sample high-speed video images of Drosophila walking (grey) are overlaid by semi-transparent images of the insect model as seen from the side **(d)** or from below **(e)**.

1.4.2 Leg motion kinematics

We use Webots position-controlled (internal P-controller) motors at each of the leg joints. These use angular position as a reference and determine the motor torque based on the P-controller. We used position control with strictly imposed leg movements since it simplifies the optimization landscape compared with more complex simulations that include muscle dynamics. Each of the leg joints is implemented as a servo node (i.e., a hinge joint with a rotational motor). The motor is operated in position control with a P-controller of constant gain. Based on the target reference position, the P-controller computes the current velocity and the necessary torque, which is then applied directly at the joint by the physics simulator. At each simulation step, the P-controller computes the current velocity v_c as in equation 1.1:

$$
v_c = \begin{cases} -v_d & v_c \leq -v_d \\ P \cdot (p_t - p_c) & -v_d < -v_c < v_d \\ v_d & v_c \geq v_d \end{cases} ,
\tag{1.1}
$$

where v_c is the current servo velocity, P is the P-control parameter specified in the `controlP` field, p_t is the target position of the servo (predefined), p_c is the current servo position, v_d is the desired velocity as specified by the `maxVelocity` field. This is a standard implementation of the ODE/Webots P-controller. We did not limit acceleration. ODE joint motors have two essential parameters: velocity and maximum torque. The maximum torque is predefined for each joint, whereas the velocity is computed by the P-controller. The effective torque that has to be applied is then computed such that the desired velocity is reached within one time step. The general and joint parameter values are given in table 1.3 as follows:

Δt	v_{max}	τ_{max}	p-gain	a	γ	δ
$0.2ms$	$100\frac{rad}{s}$	$2.1 \cdot 10^{-8} Nm$	50	not limited	0	0

Table 1.3 – General and joint parameter values for simulation of the insect model

, where Δt denotes the basic simulation time step, v_{max} the maximum speed, τ_{max} the maximum torque, a the acceleration, γ the spring constant, δ the damping constant.

We defined the range of motion for each leg joint based on observations of freely walking *Drosophila* using high-speed videography (Gloor Instruments, Uster Switzerland) and by referring to previous studies on insect locomotion and leg organization (Cruse et al., 2007; Soler et al., 2004; Sink, 2007). During ground locomotion, gravitational surface friction is the main interaction force. The movements of the legs relative to the head-thorax-abdomen rigid body are the same for all gaits. Based on observations of *Drosophila* walking in high-speed videos, the movements of each leg were preprogrammed as sinusoidal joint angle movements within an observed range of motion and fixed phase lags between the motions for each joint (Fig. 1.2). Although the movements of the legs are fixed, their duty factor - how long a foot is in

contact with the ground - varies and is free to emerge during our gait optimization. This is because foot contacts depend on the roll, pitch, and elevation movements of the whole body, which vary over time and depend on the gait. Similarly, the stride length (progress per cycle) emerges during optimization. However, the stride frequency is kept constant at 20 Hz, a stride frequency that we measured from rapidly walking *Drosophila*. For larger models (25 mm and 250 mm), stride frequencies were scaled based on the Froude number ($Fr = v/\sqrt{gl}$) and the Strouhal number ($St = fl/v$) [1]. Specifically, 20Hz in the 2.5 mm model corresponds to 6.32 Hz for the 25 mm model and 2 Hz for the 250mm model. To have an integer number of simulation steps, a frequency of 5 Hz was used for the 25 mm model.

The ranges of motion for each joint is (in degrees - intervals indicate ranges, single values indicate constant position without oscillation):

Leg Type	Body- Coxa promotion/ remotion	Body- Coxa abduction/ adduction	Body- Coxa rotation	Coxa- Femur flexion/ extension	Femur- Tibia flexion/ extension	Tibia- Tarsus flexion/ extension
Hind	[-75, -45]	[40, 59]	[-55, -20]	[40, 107.2]	[50, 135]	20.5
Middle	[-25, 25]	25.44	0	[80, 90]	[80, 90]	25.5
Front	[70, 80]	[-40, 10]	[0, 40]	[90, 160]	[55, 125]	21

Table 1.4 – Ranges of motion for the different joints in degrees. Intervals indicate ranges, single values indicate constant position without oscillation

The relative phase of oscillation for each joint is given as follows (in degrees):

Leg Type	Body- Coxa promotion remotion	Body- Coxa abduction/ adduction	Body- Coxa rotation	Coxa-Femur flexion/ extension	Femur- Tibia flexion/ extension	Tibia- Tarsus flexion/ extension
Hind	180	0	180	200	180	0
Middle	180	0	0	270	90	0
Front	0	210	0	0	20	0

Table 1.5 – Relative phase of oscillation for each joint in degrees

---

[1] *v*: speed , *g*: gravitational acceleration, *l*: body size, *f*: frequency

1.4.3 Relevant reaction forces

We computed the frictional forces with the surface according to equation 1.2:

$$F_R = \mu F_N \sim \mu m g = 1.4 \cdot 10^{-7} N \quad , \tag{1.2}$$

where the friction coefficient $\mu = 0.1$, leg mass $m = 1.42.10^{-7} kg$, and gravitational acceleration $g = 9.81 \frac{m}{s^2}$. The ODE uses a simple Coulomb friction model. Specifically, we use symmetric coulomb friction in Webots and default values for `bounce` and `bounceVelocity`. The bounce parameter defines the type of collision (1: elastic collision, < 1: inelastic collision). Our `contactProperties` node was set to the following - $\lbrack$`coulombFriction = 4; bounce = 0.5; bounceVelocity = 0.01; forceDependentSlip = 0` $\rbrack$. A friction pyramid (approximation of a friction cone) is used to determine when slipping begins. We use a friction coefficient of $\mu = 4$. This represents an upper bound rather than the classical coulomb friction coefficient. A contact point with a ground reaction force that lies within the friction cone leads to a non-slipping contact. When the ground reaction force moves out of the friction cone, a slipping contact is established. In Webots/ODE the friction cone is approximated by a friction pyramid (i.e., apex at the contact point, axis aligned with the normal force direction, base defined by two orthogonal tangential directions of ground plane). To compute the effective friction force, the ODE first assumes that the contact is frictionless and computes the resulting normal force F_n. Based on this, the maximum frictional force in either of the two tangential directions is computed as $F_{t,max} = \mu |F_n|$. The ODE then continues to solve the system based on these limits for two cases:

1. Static friction: the ground reaction force lies inside the friction pyramid. Therefore, the frictional force will be computed to compensate for tangential forces.

2. Dynamic friction: the ground reaction force lies outside the friction pyramid, therefore the frictional force is computed as $F_{t,max}$.

In addition to a universal frictional force, a leg-adhesion force is present on the pretarsus of each of the model's legs to mimic adhesive structures (claws and pulvilli). The adhesion force is applied during sticking and sliding conditions as soon as there is contact (collision) between the foot and the substrate plane. The strength of this force was determined by measuring how many pretarsi are required for *Drosophila* to suspend inverted from a cotton substrate for more than 1 s. In our experiments one pretarsus was sufficient for substrate adhesion (two pretarsi: 10/10 flies hanging > 1 s; one pretarsus: 11/11 flies hanging for > 1 s; no pretarsi: 0/10 flies hanging for > 1 s). Therefore, in our insect model, a minimal adhesive force, F_{ad}, equivalent to that required for a single contact point/pretarsus to suspend the model in an inverted orientation is considered a 100 % adhesion level. For our experiments we used 200 % adhesion since this was the minimal amount required for gait optimization to be successful

in all possible travel orientations (e.g., vertical). Although leg adhesion forces have not been formally measured for *Drosophila melanogaster*, this is likely a lower bound based on studies of other species (Federle and Endlein, 2004; Eisner and Aneshansley, 2000). Adhesive forces are implemented as constant normal forces acting on the pretarsus when it is in contact with the substrate. Since the normal force plays a role in the friction model, the adhesion force also has an impact on friction. For example, with 200 % adhesion, each leg that is in contact with the ground experiences an additional normal force due to adhesion that corresponds to twice the weight of the insect model. As explained above, this normal force, F_n, represents an upper bound inside the friction pyramid. The effective tangential friction force will be much smaller and just enough to ensure static contact. In other words, the adhesive force modifies the friction pyramid criterion to make tangential slipping much harder. Note that the issues concerning a closed kinematic chain are resolved for our model. A kinematic chain is a series of rigid bodies connected via joints whose movements are therefore coupled. A closed kinematic chain implies a series that contains at least two fixed joints, thereby creating a loop. When the model is using a tripod gait and three legs are in sticking contact with the ground, a closed kinematic chain is present with three fixed points/joints on the ground. Each leg has a predefined movement based on the model's kinematics, leaving us with three degrees of freedom for each leg's phase of motion. One might therefore expect that there are not enough degrees of freedom to achieve forward movement while using the tripod gait. However, the tripod gait can be exploited in two ways. First, in the absence of adhesion, slipping (reduced normal force) is present. Therefore, legs in contact with the substrate may be not be in sticking contact, relaxing the constraints imposed by the closed kinematic chain. Second, in the presence of leg adhesion, the P controlled joint trajectories exhibit a minimal compliant behavior that is sufficient to make the tripod gait possible. Evidence of our model's ability to overcome restrictions imposed by the closed kinematic chain can be seen in the results of our optimization experiments: the tripod gait emerges in each of the five conditions, either with or without adhesion.

We did not model air drag in our simulations. While drag is an important factor for insect flight, we found that it is not nearly as relevant as frictional forces for walking. We computed drag forces for a single leg according to equation 1.3:

$$F_D = \frac{1}{2}\rho v^2 c_D A = 2.8563 \cdot 10^{-10} N \quad , \tag{1.3}$$

where $\rho = 1.225\frac{kg}{m^3}$ (density of air), $c_D = 1.05$ (drag coefficient for a cube). The velocity was computed based on the frequency of leg motion and length of each leg: $v = 2\pi f L = 0.0628\frac{m}{s}$, where $f = 20Hz$ and $L = 0.0005m$. We considered the area of a leg as the drag area $A = d \cdot L = 5.10^{-8}m^2$, where $d = 100\mu m$. Frictional forces are therefore three orders of magnitude larger and dominate drag forces. Similar results were obtained, if drag forces are calculated for the whole body with the velocity $v = 0.02\frac{m}{s}$ (the approximate maximum walking speed of a fly)

and the drag area $A = 0.00252 m^2$ (the cross-sectional area approximated by the square of a fly's length). In this case $F_D = 1.6 \cdot 10^{-9} N$ and is still several orders of magnitude smaller than frictional forces.

1.4.4 Gait optimization

We used Particle Swarm Optimization (PSO) (Clerc and Kennedy, 2002), a stochastic optimization algorithm (Floreano and Mattiussi, 2008), to discover gaits that optimize forward velocity under different adhesion and travel orientation conditions. We implemented PSO using the inspyred (inspyred.github.com) Python (python.org) framework. Briefly, 50 candidate gaits (particles) were randomly initialized within a 5-dimensional search space of possible solutions. Each dimension represents one leg's phase of motion relative to the front left leg, which was fixed at 0° phase. During PSO, the phases of the five remaining legs could vary between 0° and 360°. For example, in this formulation a phase vector [L1 = 0°; R1 = 180°; L2 = 180°; R2 = 0°; L3 = 0°; R3 = 180°] defines the classic tripod gait – which we call tripod-A to distinguish it from alternative three-legged gaits.

Each particle was initialized with a random velocity that defined its movement within this search space during an iteration of the algorithm. Then, each particle's gait was simulated in the model. We measured its forward velocity (fitness) over 0.5 s of simulated time. This allowed us to bias optimization for straight locomotion. Notably, we did not explicitly optimize for energy efficiency but nevertheless obtained more energy efficient gaits as a by-product of speed optimization. For each iteration particle positions were adjusted according to equations 1.4 and 1.5:

$$v_i^{t+1} = w v_i^t + c_1 r_1 (p_{b,i}^t - x_i^t) + c_2 r_2 (p_{n,i}^t - x_i^t) \quad , \tag{1.4}$$

$$x_i^{t+1} = x_i^t + v_i^t \quad , \tag{1.5}$$

where v_i^{t+1} is the velocity of particle i at the time $t + 1$, v_i^t is the current velocity of the particle, x_i^t is the current position of the particle, $p_{b,i}^t$ is the position of the personal best solution of particle i, $p_{n,i}^t$ is the position of the neighborhood best solution, r_1 and r_2 are random numbers in the range [0,1], and the coefficients w (inertia weight), c_1 (cognitive rate), and c_2 (social rate) are fixed. For our simulation, we used the suggested (Clerc and Kennedy, 2002; Deb and Padhye, 2010) values $w = 0.729$, $c_1 = 1.49$, and $c_2 = 1.49$. Additionally we limited the maximum particle velocity to 0.4 (a fraction of the parameter space). The approach described here and implemented in inspyred is outlined in (Deb and Padhye, 2010). Because our search space is periodic/circular ($f(0) = f(2\pi)$), we implemented a specialized bounding function using a custom PSO class that inherits the inspyred class, and replaces the vector determination function. For each experimental condition, we ran 15 experiments with 50 particles each over 150 iterations. This number of iterations was chosen after assessing the convergence

time of the optimization process. This number of experiments was chosen to best explore the search space of possible gaits while also limiting computing time. We optimized for different geometric conditions (e.g., ground and vertical locomotion) by changing the global direction of gravitational acceleration. If a model fell off of the substrate during vertical locomotion, the forward distance traveled before falling was taken into account when calculating speed rather than setting the fitness to zero. This procedure helped smooth the fitness landscape and assisted optimization.

1.4.5 Gait classification

We classified optimized gaits based primarily on footfall patterns (as assessed using a footfall diagram) and, to a lesser extent, phase vectors. Footfall patterns were emphasized over phase vectors since gaits are highly dependent on leg adhesion conditions and locomotor orientation even for those with similar phase vectors. Therefore, footfall patterns are more closely linked to the success or failure of a given gait than the underlying phases of motion for each leg. For the sake of completeness, we also present a quantification of the degree to which a gait's phase vector approximates the ideal phase vector for each class (tripod-A, tripod-B, tripod-C, bipod-A, bipod-B, and bipod-C, Fig. 1.3). An ideal phase vector for each gait class was determined by considering the average phases across all gaits jointly comprising a class and, whenever possible, by biasing these phases to be left/right leg symmetric. Then, the phase vector for each optimized gait was compared to this ideal phase vector of a given class to generate an error metric (ϵ_m) according to equation 1.6:

$$\epsilon_m = \sum_{leg=1}^{5} |cos(\theta_{leg}^{ideal}) - cos(\theta_{leg}^{optimized})| + |sin(\theta_{leg}^{ideal}) - sin(\theta_{leg}^{optimized})| \quad , \qquad (1.6)$$

where leg is the leg being examined, θ^{ideal} is the phase vector for the ideal version of a given gait class, and $\theta^{optimized}$ is the phase vector for the optimized gait being studied. After studying each optimized gait in this way, cases with high error values were re-examined to identify potentially incorrect classifications. Ultimately, however, ambiguities in classification between two potential gait classes were resolved by examining how well footfall diagrams for each gait resembled those of each gait class. Unique, unstructured (i.e., asymmetric) gaits were classified as 'unclear'.

1.4.6 Gait analyses

We measured actual leg contacts with the surface (stance periods) to generate footfall/gait diagrams. To calculate the mean number of legs in stance phase, we averaged the number of legs in stance phase over multiple walking cycles. To measure duty factors, we averaged the relative amount of time that a given leg was in stance phase over five locomotor cycles. We measured
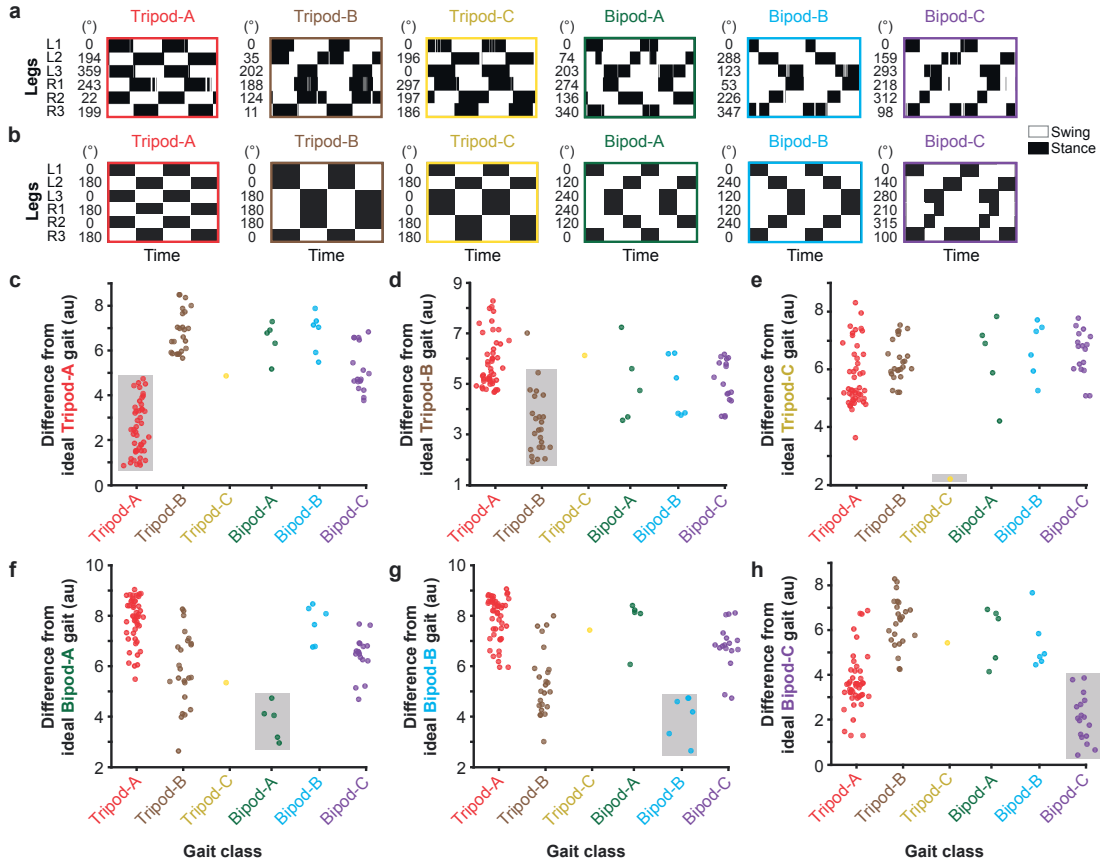
Figure 1.3 – **Gait classes and quantitative justification of gait classification. (a)** Representative and **(b)** idealized footfall diagrams showing stance (black) and swing (white) phases for each of the six gait classes identified. Two walking cycles are shown for each footfall diagram. The phase of motion for each leg is indicated. **(c-h)** Sum of the difference between leg phases of motion for each optimized gait (sorted by class) versus the idealized **(c)** tripod-A, **(d)** tripod-B, **(e)** tripod-C, **(f)** bipod-A, **(g)** bipod-B, or **(h)** bipod-C gait. Optimized gaits are color-coded by class. Data points are randomly scattered along the x-axis for clarity. Grey boxes highlight optimized gaits within their own, assigned class.

ground reaction forces (GRFs) using touch sensors on each pretarsus. These sensors measure the 3D-contact force of the ball foot with the environment. 3D-forces are first measured in the local coordinate frame of the pretarsus rigid body and then transformed to global coordinates by measuring the orientation of the pretarsus with respect to the global frame. We consider straight gaits, and therefore we can relate anterioposterior and mediolateral forces to x and y coordinates of the global frame. We smoothed noisy sensor measurements in post-processing. As a measure of the potential for static stability, we asked if the projection of the center of mass (COM) to the surface plane fell inside a convex support polygon formed by the foot endpoints in contact with the substrate (Alexander, 2003). This COM criterion can only relate to static stability for the ground case and not for vertical locomotion. Therefore, to measure the stability of gaits optimized during vertical climbing, we retested these gaits during ground locomotion with adhesion. In several instances we found that gaits optimized for vertical sideways and vertical downward locomotion were unable to support ground locomotion. These gaits failed in the first walking cycle and were excluded from subsequent analysis. We measured the percentage of time that body postures fulfilled this criterion to determine the overall stability characteristics of a particular gait. For each analyzed gait the first locomotor cycle was omitted (to achieve steady state) and the remaining 9 cycles were evaluated. Calculating metabolic cost in biological systems is complicated for a number of reasons (Full, 1997). However, as a first approximation we equated mechanical energy as metabolic cost in our insect model. Specifically, as an estimate of energy consumption, we measured the cost of transport (COT), a dimensionless value, according to equation 1.7:

$$COT = \frac{E}{mgd} \quad , \tag{1.7}$$

where E represents the energy needed to move the system along a distance d. m denotes the mass and g the gravitational acceleration. E is defined as the integral of power according to equation 1.8:

$$E = \int_0^T \Big(\sum_{i=1}^N |\tau_i \omega_i| \Big) dt \quad , \tag{1.8}$$

where τ_i and ω_i denote the applied torque and angular velocity at the i-th joint, respectively. T corresponds to the simulation time (0.5 s) and N is the number of motors across all the legs.

1.4.7 Hexapod robot experiments

To test our *in silico* results in a physical system, we built a Bioloid hexapod robot (Robotis Inc., Seoul, Korea). This robot is 57 cm long from front leg tip to rear leg tip at full leg extension and

weighs 1.9 kg. The morphology of the robot is quite different from the insect model since it is much larger and lacks a head, abdomen, and several leg segments. However, since morphologically diverse insects have similar footfall patterns we reasoned that these characteristics of locomotor gaits might be robust to morphological differences in our experiments as well. To ensure adequate friction between the robot and the ground, a piece of latex with a static friction coefficient, μ, of 0.71 was bound to the tip of each leg. The robot has three leg degrees of freedom (1 promotion/remotion and 2 flexion/extension) compared to the six degrees of freedom in the insect model (1 rotation, 1 promotion/remotion, and 4 flexion/extension). Therefore, to implement the model's cyclical motions for each leg, we discarded the rotation joint from the model, linked the promotion/remotion joints of the model directly to the robot, and used an inverse kinematics approach to map four flexion/extension joints of the model to the robot's two flexion/extension joints. To compute this mapping between the robot and insect model we first wrote a custom Python script to measure the joint angles of the model through time. With the known angles and segment lengths of our model (Supplementary Fig. A.6b), we could identify the leg tip positions in their plane of motion by solving equations 1.9 and 1.10:

$$x = a\cos(\alpha) + b\cos(\alpha + \beta) + c\cos(\alpha + \beta + \gamma) + d\cos(\alpha + \beta + \gamma + \delta) \quad , \tag{1.9}$$

$$y = a\sin(\alpha) + b\sin(\alpha + \beta) + c\sin(\alpha + \beta + \gamma) + d\sin(\alpha + \beta + \gamma + \delta) \quad , \tag{1.10}$$

where a, b, c and d are the lengths of the model's leg segments (proximal to distal) and α, β, γ, δ and are their respective joint angles. Using these data, our next goal was to find the angles, and that will place the tips of the robot's legs in the same position (x_1, y_1) as the model's legs. To do this we solved equations 1.11 and 1.12:

$$x = e\cos(\lambda) + f\cos(\lambda + \sigma) \quad , \tag{1.11}$$

$$y = e\sin(\lambda) + f\sin(\lambda + \sigma) \quad , \tag{1.12}$$

where e and f are the lengths of the robot's leg segments (proximal to distal) and λ and ω are their respective joint angles. Of the two solutions, we identified the one that was physically feasible in the robot. Additionally, a bias was added to ensure that the model's range of promotion/remotion angles could be matched in the robot. To produce different gaits, as for the insect model, we shifted the relative phase of each leg's motion cycle. The resulting trajectories of the robot's foot tips are shown in Figure A.6c. We video recorded (Canon, Melville, NY USA) the robot at 25 fps to quantify leg kinematics and speed. We then used custom Matlab scripts (The Mathworks, Natick, Massachusetts, USA) to track the motion of red markers on the leg tips, for leg kinematic measurements, or on the dorsal surface of the robot, for speed measurements. We performed ten experiments for each condition but

found very few differences between experimental replicates. Data were analyzed using the two-sample t-test since data were normally distributed. We show all the raw data points for each experiment to illustrate the variance for each condition and that this variance is the same between compared groups.

1.4.8 *Drosophila* experiments

Experiments were performed at 22°C in the late afternoon Zeitgeber Time (ZT) on 2-4 days post-eclosion female Drosophila (2.5 mm long and 0.85 mg) of the Canton S background raised at 25°C on a 12h light:12h dark cycle. We filmed individual flies in a small Poly(methyl methacrylate) arena (3 cm x 3 cm) illuminated by a dim red ring light (FALCON Illumination MV, Offenau, Germany). We continuously acquired images at 500 fps using a high-speed video camera (Gloor Instruments, Uster Switzerland). To motivate fast forward locomotion, we grazed the wings with a small metallic disc (1 mm diameter) to elicit an escape response. If a fly exhibited a long bout of straight locomotion (i.e., without premature voluntarily stopping and without encountering the arena wall), a video was captured and manually analyzed to measure stance and swing phases for each leg. This criterion for data inclusion was pre-established. No randomization or blinding was performed. Fast gaits are typically very consistent across animals. Nevertheless, we performed multiple replicates (N = 9-10) for each condition to account for trial-to-trial differences in UV polymer coating and inter-animal variability. Data were typically not normally distributed. Therefore, we used a Wilcoxon rank sum test for statistical comparisons. We show all raw Tripod Coordination Strength and Atypical bipod-like leg coordination strength data points for each experiment to illustrate the variance for each condition and that this variance is not the same between compared groups. This difference is due to the floor effect on Tripod Coordination Strength and Atypical bipod-like leg coordination metrics. For polymer coating, flies were first briefly anaesthetized with CO_2. We then placed a small drop of UV-curing glue (Ivoclar Vivadent AG, Schaan, Principality of Liechtenstein) on the pretarsus, or on the tarsus of each leg using a fine hair or tungsten wire. The polymer was then hardened by 20 s exposure to UV light. Flies were allowed to recover for 1-2 h in humidified 25°C incubators. Prior to behavior experiments, we confirmed the absence of adhesion by testing if flies could hang vertically on the smooth walls of a plastic vial. For substrate coating experiments, we dried a layer of Fluon (Whitford GmbH, Diez, Germany) on the walking surface. We also clipped each fly's wings to permit visualization of every leg from a dorsal perspective. To measure the static coefficient of friction of animals, we placed flies (with or without polymer coating) on a horizontal surface (with or without Fluon coating) and measured the tilt angle, θ, at which animals began to slide. The static coefficient of friction, μ_s, was then calculated according to equation 1.13:

$$\mu_s = tan(\theta) \quad .\tag{1.13}$$

We analyzed locomotor gaits using several metrics of leg coordination. First, we used a Tripod Coordination Strength (TCS) metric functionally similar to one used previously (Wosnitza et al., 2013) to compare measured gaits to the classic insect tripod gait. Specifically, after initiating fast touch-evoked escape walking, we measured the first frame during which the right front leg was in stance phase and, following three walking cycles, the final frame during which the front right leg was in swing phase. This period of three walking cycles was deemed t_1. Then, we measure the proportion of time, t_2, during this period during which an animal is in a tripod stance (only R1, L2, R3 are in stance, or only L1, R2, L3 are in stance). TCS values are the ratio $\frac{t_2}{t_1}$. Similarly, we quantified atypical bipod-like leg coordination by measuring the proportion of time that the contralateral front and rear legs (L1 and R3, or L3 and R1), or middle legs (L2 and R2) moved synchronously in swing phase. These kinds of leg synchronization are not normally observed during fast *Drosophila* locomotion (Mendes et al., 2013; Wosnitza et al., 2013).

1.5 Results

1.5.1 Tripod gaits are optimal for fast climbing using leg adhesion

Using this gait discovery approach, we first asked to what extent, if at all, the tripod gait would be discovered as fastest under different conditions. Specifically, we optimized gaits for (i) upward climbing, (ii) downward climbing, (iii) or sideways climbing using leg adhesion, (iv) ground locomotion with leg adhesion, or (v) ground locomotion in the absence of leg adhesion ($N = 15$ each). These five conditions allowed us to measure the influence of travel orientation and/or leg adhesion on optimally fast gaits. For each experiment, gaits were classified based primarily on the model's footfall patterns since even gaits that share similar leg motion phase vectors can behave differently depending on the model's orientation (vertical, or horizontal), and whether the model has leg adhesion. Across all five conditions we often discovered gaits with similar footfall patterns. Thus, we were able to classify most gaits as belonging to one of six categories (Fig. 1.3 and Supplementary Fig. A.3): the classic tripod gait (tripod-A), as well as alternative three-legged gaits (tripod-B, tripod-C) and two-legged gaits (bipod-A, bipod-B, bipod-C) that we later describe in more detail. Gaits discovered as optimal for upward climbing using leg adhesion had high Tripod Coordination Strength (TCS, functionally similar to the quantification used in Wosnitza et al. 2013) values (Fig. 1.4a, left), indicating that their footfall diagrams resemble that of the classic tripod gait (Fig. 1.1e). These values were only slightly lower than those measured for real *Drosophila melanogaster* during touch-evoked fast locomotion (Ramdya et al., 2015) (Fig. 1.4a, far right, 'Drosophila TCS'; $P = 0.004$, Wilcoxon rank sum test). Moreover, nearly all of the discovered gaits closely resembled one another and were classified as tripod-A since their footfall patterns were quite similar to the classic tripod gait (Fig. 1.6c). One gait had a low Tripod Coordination Strength (TCS = 0.16, experiment 5) and was also the slowest (Fig. 1.4b, left). Upward climbing gaits had on average three legs on the ground at any one time (Fig. 1.5a, left), forming a polygon of support within which the model's center of mass (projected normal to the surface) would rest when used for ground locomotion (Fig. 1.5b, left).

Interestingly, when optimizing for downward and sideways climbing using leg adhesion, in addition to the classic tripod gait, an alternative form of tripod coordination, the tripod-B gait, also emerged (Fig. 1.4, center-left and center). For the tripod-B gait, the front and middle legs on one side of the body move in near synchrony with the rear leg on the other side of the body (Fig. 1.3a-b). This too yields an average of nearly three legs on the substrate at any given moment (Fig. 1.5a, center-left and center) and the potential for static stability when used for ground locomotion (Fig. 1.5b, center-left and center). In contrast to climbing gaits, when optimizing for fast ground locomotion with leg adhesion, we discovered a variety of novel gaits that were as fast or even faster than the classic tripod gait (Fig. 1.4b, center-right) and could also have fewer legs in stance phase at any given moment (Fig. 1.5a, center-right). Taken together, these data demonstrate that a requirement to rapidly navigate vertically oriented terrain is sufficient to favor the classic tripod gait during optimization. Leg adhesion by itself has only a weak effect on the optimality of the classic tripod gait over alternative gaits.

27
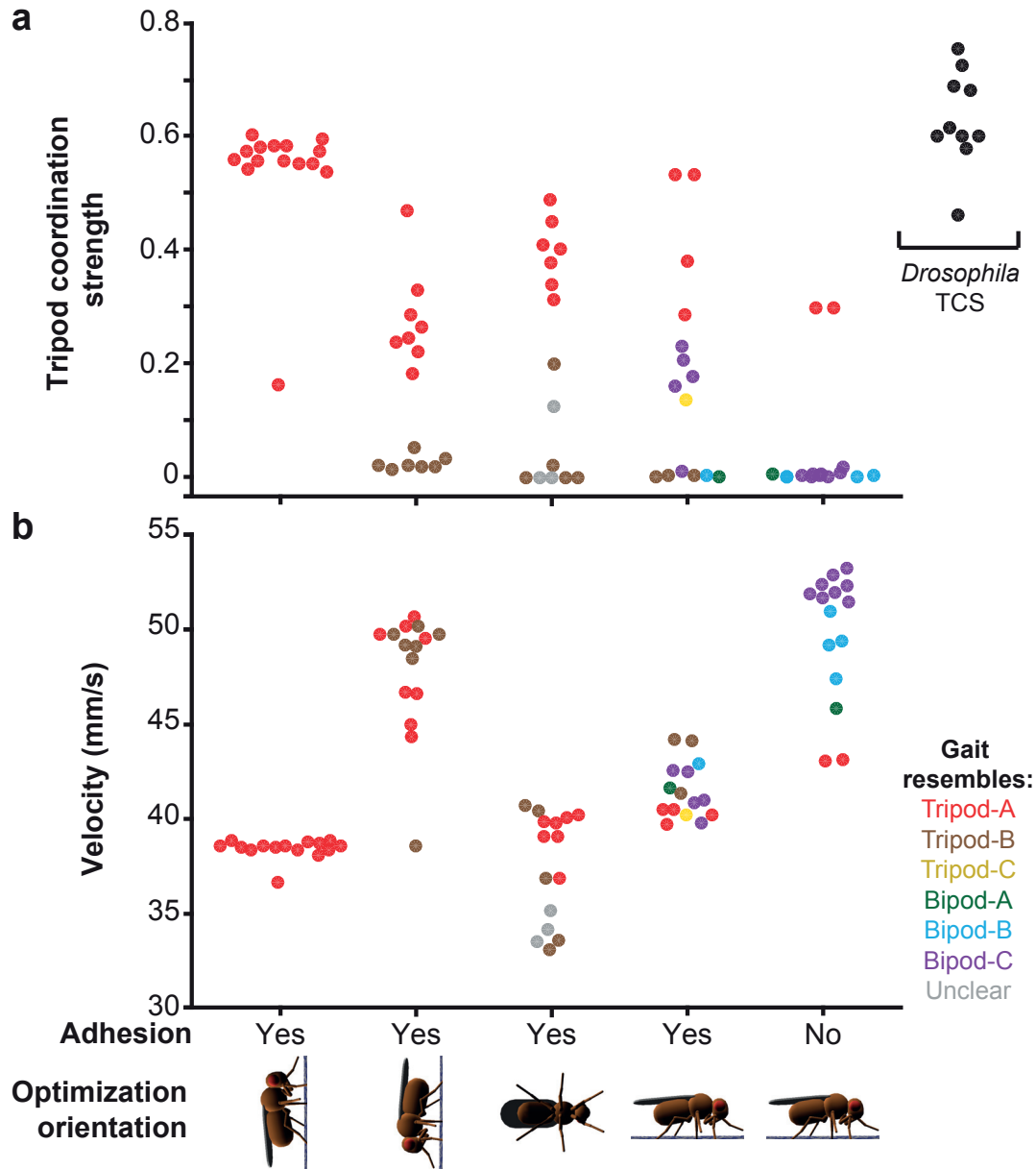
Figure 1.4 – **Tripod gaits are optimal for fast climbing using leg adhesion**. Gaits were optimized for forward velocity while climbing upward (left), downward (center-left), or sideways (center) on a vertical surface using leg adhesion, walking on the ground with leg adhesion (center-right), or walking on the ground without leg adhesion (right). **(a)** Tripod coordination strength (TCS) values indicating the degree of similarity to the classic tripod gait footfall diagram (tripod-A). N = 15 for each condition. For comparison, TCS values for *Drosophila melanogaster* during rapid, touch-evoked ground walking are shown on the far right (black, N = 10). **(b)** The average velocity of each gait. Optimized gaits are color-coded by class. Data points are randomly scattered along the x-axis for clarity. N = 15 for each condition.
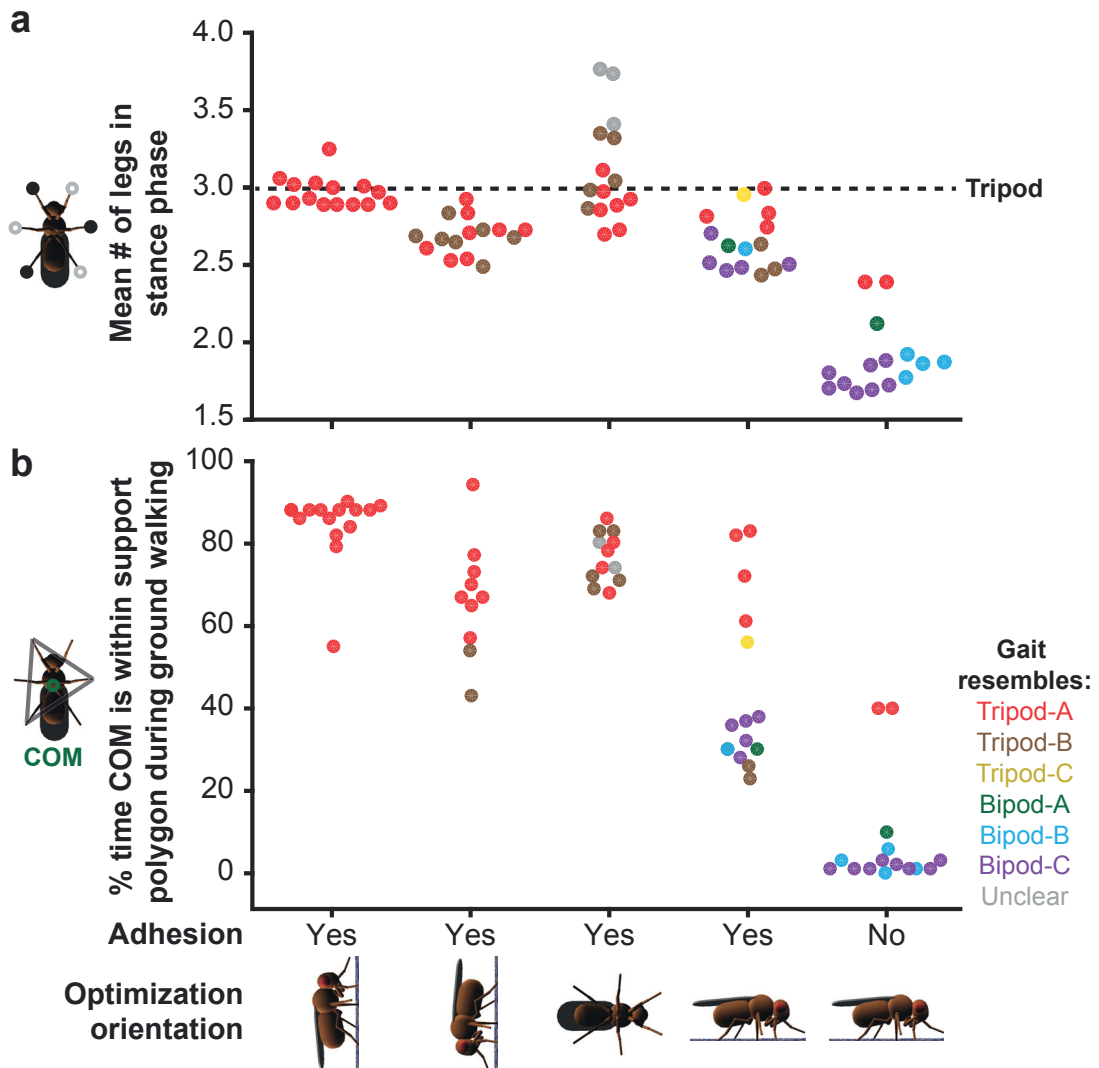
Figure 1.5 – **Dynamically stable bipod gaits are optimal for fast ground locomotion in the absence of leg adhesion**. Gaits were optimized for forward velocity while climbing upward (left), downward (center-left), or sideways (center) on a vertical surface using leg adhesion, walking on the ground with leg adhesion (center-right), or walking on the ground without leg adhesion (right). **(a)** The average number of legs in stance phase over five walking cycles. A dashed black line indicates three legs in stance phase as expected for the classic tripod gait. N = 15 for each condition. **(b)** The percentage of time that the model's Center-of-Mass (COM) lies within a polygon of support delineated by each leg in stance phase when the gait is tested during ground walking. The level of adhesion is kept as during optimization. Optimized gaits are color-coded by class. Data points are randomly scattered along the x-axis for clarity. N = 15 for each condition except for vertical downward (N = 11) and vertical sideways (N = 12) locomotion since in these conditions several gaits were unable to support ground walking.

1.5.2 Bipod gaits are optimal for fast ground locomotion without adhesion

Large vertebrates typically do not depend on leg adhesion to locomote (but note the exceptional climbing abilities of smaller vertebrates such as geckos and squirrels). Instead, they rely on frictional forces to traverse the ground. By contrast, many insects use adhesive structures during ground locomotion. We hypothesized that this difference may have influenced the starkly different fast locomotor strategies used by vertebrates (dynamically stable running gaits) and insects (tripod gait). An interesting prediction of this hypothesis is that if insect gaits are optimized to locomote rapidly on the ground without leg adhesion, they might employ dynamically stable fast gaits instead of the tripod gait. To test this possibility, we optimized our insect model to generate gaits for rapid ground locomotion in the absence of leg adhesion. Indeed, we found that a large majority of optimized gaits bore little to no resemblance to the classic tripod gait (Fig. 1.4a, right, $TCS \sim = 0$). Moreover, two gaits that could be classified as tripod-A (experiments 4 and 15) were also the slowest (Fig. 1.4b, right, red circles).

Instead, the fastest gaits had on average nearly two legs on the ground at any given moment (Fig. 1.5a, right) and low duty factors (< 0.5, Supplementary Fig. A.4e). Therefore, we named these bipod gaits. In many cases, during bipod locomotion a model's projected center of mass almost never lies within a polygon of support circumscribed by the legs (Fig. 1.5b, right) causing them to be statically unstable – like many fast vertebrate running gaits. In the American cockroach, during extremely fast tripod locomotion ($> 1 \frac{m}{s}$), aerodynamic forces lift the front and middle legs off the ground resulting, effectively, in two-legged running (Full and Tu, 1991). By contrast, in our insect model, two-legged bipod locomotion arises solely from leg coordination without a contribution from aerodynamics. During bipod-A and bipod-B locomotion, each front leg moves in near synchrony with the opposite rear leg, and the middle legs move together (Fig. 1.6a). This generates three power strokes per locomotor cycle (Fig. 1.6a-b). Therefore, all else being equal (e.g., same leg speeds), bipod gaits can generate more continuous, and consequently faster, forward locomotion than the tripod gait (Fig. 1.6c). Notably, although we did not optimize for it, bipod coordination is also energy efficient: It has a lower cost of transport than the tripod gait during ground locomotion without adhesion (Supplementary Fig. A.5, right).

a   Bipod-B gait

Power stroke 1   Power stroke 2   Power stroke 3

b
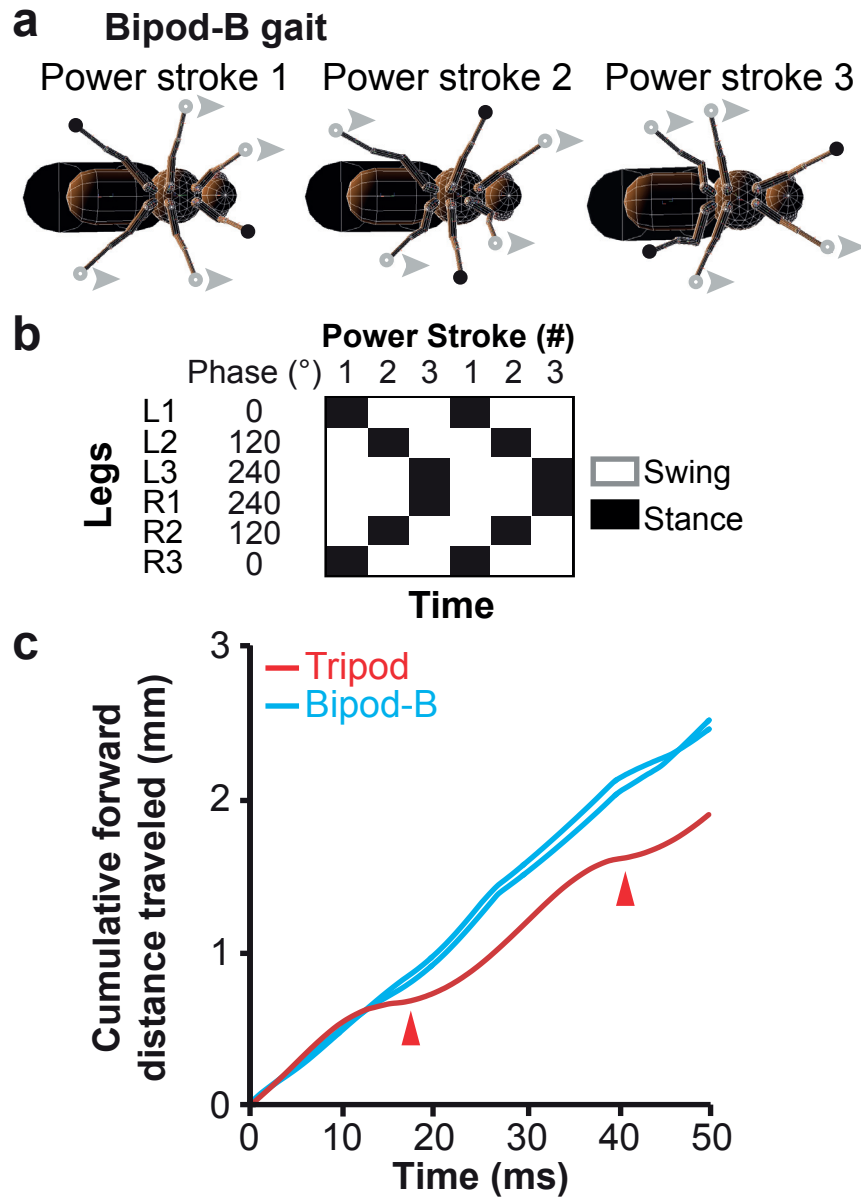
Figure 1.6 – **Bipod gaits generate three power strokes per walking cycle resulting in more continuous forward locomotion**. **(a)** The bipod-B gait has three power strokes per walking cycle. For each power stroke two legs are on the surface in stance phase (black circles) while the other four legs are in swing phase (grey circles). Arrowheads show the direction of motion. **(b)** An idealized bipod-B footfall diagram showing stance (black) and swing (white) phases for each leg. The phase of motion for each leg is indicated. Each power stroke is numbered. **(c)** The cumulative forward distance travelled while upright without leg adhesion during a single walking cycle for the classic tripod (red), or for two optimized bipod-B (cyan) gaits. Red arrowheads indicate pauses between power strokes during tripod locomotion.

1.5.3 The bipod gait is faster than the tripod gait in a hexapod robot

In silico findings can be sensitive to simulation conditions and may fail to capture the complexities of the physical world (Floreano and Mattiussi, 2008). Since it is not yet possible to genetically reprogram insect leg-coordination, we used a hexapod robot to validate our finding that bipod locomotion is faster than tripod locomotion. This also allowed us to explore whether our newly discovered bipod gaits could be used to effectively control hexapod ground robots. First, we transferred the classic tripod (tripod-A) gait and the bipod-B gait to a robot (Fig. 1.7a) using an inverse kinematic approach. In this way we could map the trajectories of the tips of the model's legs onto the tips of the robot's legs (Supplementary Fig. A.6; see Methods). We found that, as for the model, the robot produced two power strokes per walking cycle using the tripod gait (Fig. 1.7b, red) and three power strokes using a bipod gait (Fig. 1.7b, cyan). Remarkably, although it is profoundly morphologically different from the insect model (e.g., size discrepancies and different degrees of freedom for each leg), the robot is also nearly 25% faster when using the bipod gait rather than the tripod gait (Fig. 1.7c-d, P < 0.001, two-sample t-test). These data confirm that a bipod gait is indeed faster than the classic tripod gait during ground walking in the absence of leg adhesion and that these gaits can be used to control fast locomotion in hexapod ground robots.
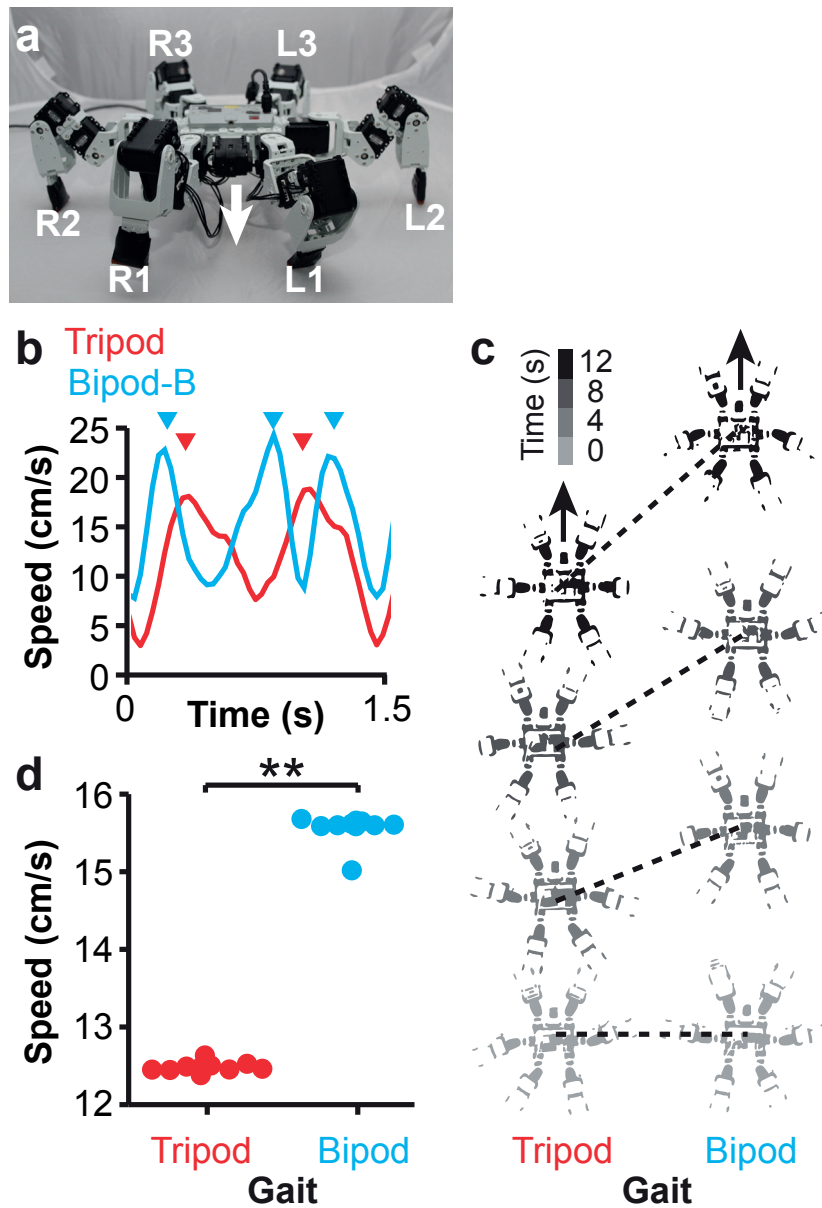
Figure 1.7 – **The bipod gait is faster than the tripod gait during ground locomotion in a hexapod robot**. **(a)** A frontal view of the hexapod robot used. Each leg is labeled in white. A white arrowhead indicates the direction of heading. **(b)** The instantaneous speed of the robot during one walking cycle using the classic tripod (red), or bipod-B (cyan) gait. Red and cyan arrowheads mark peak speeds for the tripod and bipod-B gaits, respectively. **(c)** The robot's position at four four-second intervals during tripod (left) or bipod-B (right) locomotion. Black dashed lines connect the robot's locations at corresponding time-points. Black arrows indicate the direction of heading. Scale bar is 16 cm. **(d)** Average speed over ten seconds for each gait (N = 10 each). A double asterisk (**) indicates that $P < 0.001$ for a two-sample t-test.

1.5.4 Blocking adhesion in *Drosophila* uncovers atypical bipod-like leg coordination

Despite being faster than the tripod gait, our dynamically stable bipod gaits are, to the best of our knowledge, not used by insects. This might be due to inherent neural or biomechanical constraints on limb control i.e., during fast locomotion, insects might be incapable of synchronizing their middle (mesothoracic) legs, and synchronizing their contralateral front (prothoracic) and rear (metathoracic) legs. We define these kinds of novel leg synchronization as 'atypical bipod-like leg coordination' to distinguish them from bipod gaits. Importantly, by this definition, atypical bipod-like leg coordination can occur even when more than two legs on the ground at one time. Since, in our model, removing leg adhesion led to a reduction in tripod gaits and enrichment in bipod gaits (Fig. 1.4, comparing ground locomotion with and without adhesion), we wondered how removing leg adhesion might influence fast locomotor gaits in real Drosophila. To impair leg adhesion, we covered the claws and pulvilli of each leg with a UV curable, hard polymer (Fig. 1.8a). We then elicited a rapid walking response through gentle mechanical stimulation of the wings or abdomen (Ramdya et al., 2015). Animals did not switch to dynamically stable bipod gaits with two legs on the ground in response to this perturbation. In fact, they often had four legs on the ground (Fig. 1.8b). However, these gaits did exhibit atypical bipod-like leg coordination: footfall patterns showed synchronized movement of the middle legs with one another and synchronized movement of contralateral front and hind legs with one another (Fig. 1.8b and Fig. 1.8c, top panel, right). Concomitantly, there was a nearly complete loss of Tripod Coordination Strength (Fig. 1.8c, bottom panel, right). By contrast, control animals without any perturbation or with a polymer coating on the more proximal tarsal segments (i.e., leaving adhesion by the claws and pulvilli intact) did not exhibit atypical bipod-like leg coordination (Fig. 1.8c, top panel, left and center-left). Instead they used gaits exhibiting normal, high Tripod Coordination Strength values (Fig. 1.8c, bottom panel, left and center-left).

One potentially trivial explanation for these results is that animals whose adhesive leg structures are covered simply slip and are unable to coordinate their limbs in any meaningful way. To examine this possibility and to more generally test the role of slipping on fast locomotor gaits, we studied flies walking rapidly on a surface coated with Fluon. Fluon coating lowers the coefficient of friction (Bowden and Tabor, 1950) and also blocks claw and adhesive pad contact with the underlying substrate (Endlein and Federle, 2008). This causes slipping, making it very difficult for insects to adhere to surfaces, and preventing climbing (Merton, 1956; Dankert et al., 2009). We measured similar coefficients of static friction, μs, for unperturbed animals on a Fluon-coated surface ($\mu s = 0.84 \pm 0.13$) as for animals with polymer coating on their distal tarsal segments on an uncoated surface ($\mu s = 0.83 \pm 0.04$). Atypical bipod-like leg coordination was completely absent in animals walking rapidly on Fluon-coated surfaces (Fig. 1.8c, top panel, center-right, $P < 0.001$ for a Wilcoxon rank sum test when compared with Pretarsus polymer experiments). Moreover, while reduced, the gaits of flies walking on Fluon could still have high Tripod Coordination Strength values (Fig. 1.8c, bottom panel, center-right, $P < 0.001$ for a Wilcoxon rank sum test compared with Pretarsus polymer coating). These results reveal
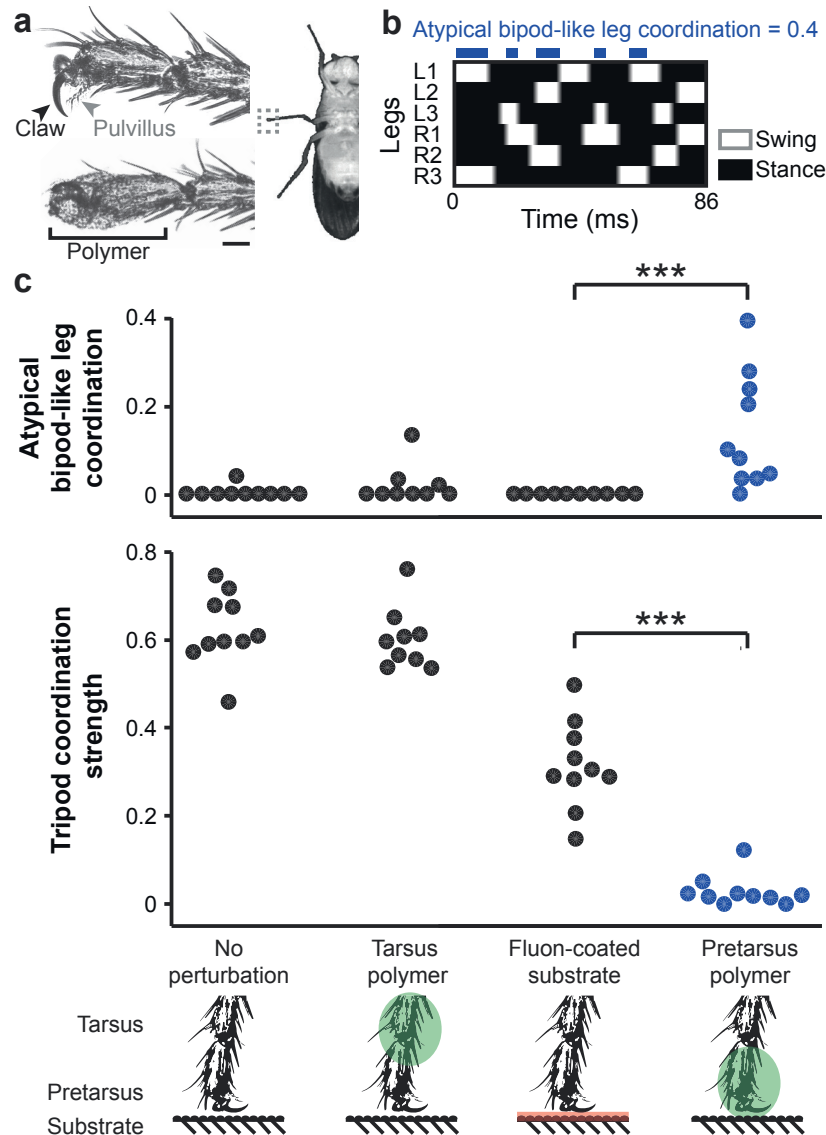
Figure 1.8 – **Blocking leg adhesion in *Drosophila* abolishes the tripod gait and uncovers the potential for atypical bipod-like leg coordination**. **(a)** The pretarsus, the distal-most segment of the *Drosophila* leg (grey dashed box, right), houses a claw (black arrowhead) and pulvillus attachment pad (grey arrowhead), which are used to adhere to surfaces (left, top). We used a UV-curing polymer to cover pretarsal adhesive structures (left, bottom). Scale bar is 40 μm. **(b)** Footfall diagram for a fly walking with polymer coating on each pretarsus. Contact with the ground during stance phase (black) and no ground contact during swing phase (white) are indicated for each leg over time. Blue blocks indicate periods of atypical bipod-like leg coordination. This animal exhibits atypical bipod-like leg coordination 40 % of the time. **(c)** Atypical bipod-like leg coordination (top) and Tripod Coordination Strength (bottom) for unperturbed flies (left), flies with polymer on each tarsus (green, middle-left), flies walking on a Fluon-coated substrate (pink, middle-right), or flies with polymer on each pretarsus (green, right). N = 10, 9, 10, and 10 flies, respectively. A triple asterisk (***) indicates that $P < 0.001$ for a Wilcoxon rank sum test.

that atypical bipod-like leg coordination does not emerge simply because flies are slipping on the ground. Instead, leg adhesion structures and/or their associated sensory feedback likely play an important role in determining which gaits are used during fast ground locomotion. When leg adhesion structures are blocked, flies replace tripod gaits with alternative gaits including those with atypical bipod-like leg coordination.

1.6   Discussion

In this study we asked which conditions might have led to the near universality of the tripod gait as a fast locomotor strategy among insects (Smolka et al., 2013; Graham, 1972; Wosnitza et al., 2013; Wilson, 1966; Zollikofer, 1994; Goldman et al., 2006). We used an optimization algorithm to discover fast locomotor gaits for a simulated insect model. Our modeling efforts were focused on optimizing the relative phases of motion for each leg: defining features of an animal's gait that are under direct control of the nervous system (Andersson et al., 2012; Talpalar et al., 2013). We did not model limb compliance and dynamical effects – like spring-mass dynamics with in phase transitions of energy between gravitational and kinetic energy – that are well established as important for fast insect gaits (Full and Tu, 1991; Ting et al., 1994) but independent of leg coordination. We found that the tripod gait systematically emerges as optimally fast for climbing up vertical surfaces. Tripod locomotion was also well represented among gaits that are optimal for fast downward and sideways climbing. By contrast, diverse gaits were optimal for flat ground locomotion with leg adhesion. Among these, the tripod gait was not the fastest. These data support the possibility that the tripod gait may be favored by insects since it permits rapid navigation of three-dimensional terrain. At first glance, this result seems rather intuitive: three-legged gaits form a closed polygon of attachment and allow an animal to pause in mid-stride without falling or swinging from vertically oriented surfaces. However, the tripod-B gait – an alternative three-legged gait that would not as strongly satisfy the requirements for static stability on the ground – also emerged as optimal for fast downward and sideways climbing. Therefore, upward climbing likely has more stringent requirements for achieving a good balance between speed and stability that may uniquely be met using the classic tripod gait. Contrasting with optimal gaits for rapid climbing, we found that dynamically stable, two-legged gaits are optimal for fast ground locomotion in the absence of leg adhesion. These novel bipod insect gaits resemble the quadruped running trot (Hildebrand, 1965), a gait used by large vertebrates. Bipod ground locomotion is also faster than the tripod gait in a hexapod ground robot. Therefore, while the tripod gait may still be a favorable approach for controlling climbing robots (Goldman et al., 2006; Chou et al., 2012), bipod gaits confer significant speed advantages on the ground (Baisch et al., 2011; Hoover et al., 2008). We hypothesize that bipod gaits are faster than tripod gaits since they generate one additional power stroke per leg motion cycle. However, this additional power stroke causes the model to use a statically unstable locomotor strategy. Although we emphasize the role of vertically oriented climbing in driving the optimality of tripod locomotion, adhesion alone might also serve to constrain available locomotor strategies: If adhesion is strong enough, the push-off force provided by three legs may be required to detach another set of three legs from the substrate. Additionally, isotropic push-off afforded by the tripod gait may be required to avoid toppling. Models contribute to our understanding of biology by allowing us to test otherwise experimentally intractable questions. In this work, we aimed to disentangle the potential impacts of environmental (climbing) and biomechanical (leg adhesion) constraints on the optimality of extant insect locomotor strategies. Although simple models are powerful tools for testing mechanistic hypotheses in a systematic manner, their scope can be limited.

There are many ways to augment our insect model in future studies to strengthen its ability to increase our understanding of insect locomotion. First, our model's P controller has a high gain that currently allows for only limited limb compliance. In future work, the model's limbs might be made more compliant by decreasing P gain and/or increasing joint elasticity (Schneider et al., 2006; Schmitt and Holmes, 2003). Second, insects come in a variety of sizes and morphologies (Snodgrass, 1935). We obtained similar results using models that are several orders of magnitude larger than our original model (Supplementary Fig. A.7). By testing models with a variety of body shapes we might also gain insight into the relationship between morphology and optimal locomotor strategies (Zollikofer, 1994). Finally, the details of leg adhesion can vary across species (Haas and Gorb, 2004; Arzt et al., 2003), suggesting another parameter that may influence gait optimality. In line with a potentially critical role for adhesion, in our model, lack of adhesion led to an enrichment of bipod gaits in place of tripod gaits. When we covered leg adhesion structures in *Drosophila*, flies also abandoned the tripod gait in favor of gaits that exhibit synchronization of the middle legs and of the contralateral front and rear legs. This is notable since middle leg synchronization is normally never observed in the fly. While front and rear leg synchronization can be seen during slow *Drosophila* walking (Mendes et al., 2013; Wosnitza et al., 2013), it is absent when animals generate rapid locomotion. These instances of what we refer to as 'atypical bipod-like leg coordination' can have more than two legs on the ground and are therefore quite different from the dynamically stable bipod gaits discovered in our model. However, these kinds of changes in leg coordination might represent early adaptations to new environments that may ultimately become fixed. For example, dung beetles and water striders traverse sand and water surfaces, respectively. To do this, they use unique bounding and sculling gaits for which the middle legs are synchronized (Smolka et al., 2013; Hu et al., 2003). This impressive capacity for flexible leg coordination suggests that neural and biomechanical constraints may not shape the locomotor strategies of insects as strongly as the need to solve specific challenges posed by the environment.

1.7 Conclusion

In summary, we investigated insect walking based on an *in silico* insect model and used Particle Swarm optimization as a means to find that the tripod gait is the result of a need for fast gaits for climbing. If we loosen the requirement to climb, but rather focus on gaits on the flat ground, adhesion is not necessary. When we optimized for speed in these modified conditions, a new bipod gait that is faster than the tripod gait was found. This particular gait can be potentially very interesting for roboticists to use on insect-like hexapod robots for fast locomotion on flat ground. Finally when blocking the means of adhesion in *Drosophila*, the tripod gait disappeared and bipod-like features were present. This does supports our findings from simulation.

Our study highlights the importance of environmental constraints for the occurrence of specific locomotion patterns that are found in nature. Different types of reaction forces such as gravitational forces acting from different angles on the body (depending on the orientation in space, e.g on the wall or on the ground), adhesion forces increasing the attachment to the substrate, or friction properties, have shown to be crucial for the emergence of specific gait patterns such as the tripod gait for insects.

1.8 Acknowledgments and Contributions

2 Undulatory Swimming

The previous chapter presented a study of locomotion in terrestrial environments. Our key question was related to the prevalence of a distinct gait pattern observed in insects and our goal was to find the crucial constraining conditions for them to emerge. In that case it was sufficient to develop a model that was able to produce different gaits in a relatively simple manner (target phase shifts between legs achieved through position control). The focus was pointed on the exploration of different gait patterns and how they would excel under different environmental conditions. Thus, we intentionally investigated gaits and their performance rather than asking how they could be generated and modulated. Both questions are arguably very interesting. Nonetheless, to keep it simple, it can be useful to look at these aspects once at a time.

In this second chapter, we now focus on the generation of gaits and asked how internal body movement can be created such that it exploits the environment best for efficient locomotion. We explored this for undulatory swimming in water and were curious to test to what extent local sensory information can be beneficial in this process. Therefore, we developed a model capable of generating periodic rhythms and adapting them based on sensory signals. As a result, abstract phase oscillators along with local pressure feedback and viscoelastic body properties revealed new insights into the control of efficient undulatory swimming.

2.1   Introduction

Undulatory propulsion is a widely spread means of locomotion for many species and has been adopted in a variety of environments (Maladen et al., 2009; Sfakiotakis et al., 1999; Guo and Mahadevan, 2008). Different types of undulations can be distinguished and include among others retrograde waves from head to tail (Cohen and Boyle, 2010). In this particular undulatory pattern, waves of body bending travel in the opposite direction of motion along the body, and it appears that in fluid environments these undulations provide a potent locomotor strategy for a diverse group of organisms across different sizes (e.g. leeches, lampreys, eels and water snakes). Remarkably low energy expenditure of migrating eels (Ginneken et al., 2005;

Béguer-Pon et al., 2015) show another advantageous property of undulatory swimming.

A crucial ingredient for efficient swimming is the adaptation to the local aquatic environment (Gemmell et al., 2015). Imposing arbitrary traveling waves of undulations will not lead to efficient swimming, as properties like body geometry and stiffness (Tytell et al., 2010), but also external influences such as viscosity and vortices, determine the resulting reaction forces with a fluid. Adaptation and synchronization of the locomotor body to and with the environment is required. Therefore, the control of the body has to be organized appropriately.

The generation of oscillation patterns of muscle activation along the body is an essential part of the control organization. Corresponding distributed neural oscillators have been identified in the spinal cord of vertebrate fish. Also known as central pattern generators (CPGs), these neural networks are able to produce rhythmic activity without receiving rhythmic input. CPGs have been found in several vertebrates (Grillner and Wallén, 1985) as well as in invertebrate (Kennedy and Davis, 1977; Clarac and Pearlstein, 2007) undulatory animals, e.g. leeches. Moreover, recordings of fictive locomotion (Grillner et al., 1981) show oscillations, in the absence of sensory information. Fictive locomotion patterns have further shown that the intersegmental coordination between neural oscillators is not solely determined by local coupling, but can also be modified and modulated by sensory cues of proprioception (Yu et al., 1999; Cang and Friesen, 2000; Wen et al., 2012; Hsu et al., 2013) aiming at synchronization between the internal neural commands and the body in response to the environment.

Computational models of leech (Iwasaki et al., 2014) and lamprey (Ekeberg, 1993) swimming have explored the interaction between body, CPGs, local proprioceptive receptors and a hydrodynamic environment. These models could explain and reproduce animal behaviors under changing viscosity and have therefore highlighted the importance of proprioceptive feedback loops regarding the adaptation to environmental changes. In *C.elegans* even pattern generation solely induced by proprioceptive stretch receptors (Niebur and Erdös, 1991) without CPGs has been suggested.

Intriguingly, the role of exteroceptive sensors such as flow, touch and pressure from the local environment has been subject to much less consideration (Phelan et al., 2010; Venturelli et al., 2012), which is surprising as these sensor modalities provide a genuine link from a swimming body to its environment. Studies on larval zebra-fish have shown that mechanosensory receptors in the lateral line can elicit swimming bouts (Haehnel-Taguchi et al., 2014). Furthermore, the lateral line organ across many fish species has been regarded as a *hydrodynamic antenna* that is able to detect pressure changes (Schwarz et al., 2011; Ristroph et al., 2015) and to provide fish with information about the hydrodynamic environment. This leads to an untested hypothesis: In order to optimize gaits and to adapt to the local environment, undulatory locomotion could be modulated by local measurements of pressure (Ristroph et al., 2015).

We tested this hypothesis using a neuromechanical model that relies on local sensory pressure measurements in a simulated hydrodynamic environment ensuring correct interaction dynamics between the undulatory swimmer and the water. In our study we propose and test

three conceptually intriguing paradigms, *combined*, *decoupled*, and *sensory-driven*, for the generation and control of undulatory wave patterns. We find that local pressure feedback loops can independently generate retrograde traveling waves of body undulations in a decoupled distributed network of neural oscillators. In a control system with coupled oscillators and fixed non-optimal phase lags - originating from central control instances - the same feedback loops further adapt these patterns towards energy and speed efficient swimming. The local feedback loops are further able to generate coordinated undulatory locomotion in a control scheme without neural oscillators and minimal coupling between segments.

Our results suggest that control for undulatory swimming can be achieved at different levels of complexity, in the absence of genuine oscillators but also in a decentralized manner, which gives new insights to the interplay between central and peripheral mechanisms necessary for swimming locomotion. Our investigations open new venues to understand locomotor control in undulatory swimming animals and to control undulatory swimming engineering systems, arising from the fundamental importance of local pressure feedback loops.

2.2 Concept

2.2.1 Neuromechanical model for undulatory swimming

Our goal was to investigate a minimal comprehensive neuromechanical model in order to explore necessary control mechanisms for undulatory swimming. Our model includes neural oscillators, local sensory feedback mechanisms, virtual muscles and a segmented elongated swimming body. All of these elements were abstracted as much as possible to identify key interaction mechanisms between them, resulting in efficient and robust swimming behavior.

Animals, like e.g. leech and lamprey, have finely segmented bodies, which help them to achieve the necessary local body bending for their particular undulatory swimming style. Based on computational and technological limitations we abstracted our mechanical model of an elongated body to $N = 10$ joints (some investigations are also presented for 20 joints to show a certain generalization of the model), which allows to project at least one wave along the body to sufficiently achieve undulatory swimming. Figure 2.1 shows the segmented robot body that we use in our study.
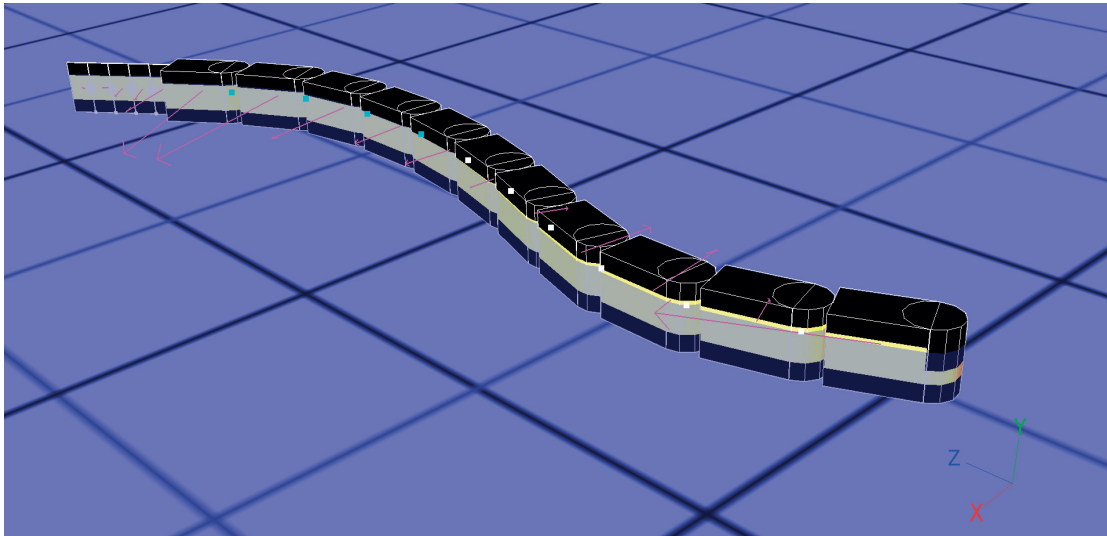
Figure 2.1 – **Simulation model**. The body consists of 11 segments connected by 10 hinge joints. Each joint can be actuated by applying torque. The tail fin is passive and consists of 5 short thin segments. Pink arrows indicate hydrodynamic forces for the given time instance where the snapshot was taken.

To induce body movements in our robot model we use a simplified muscle model inspired by Ekeberg (1993):

$$\tau_i = \alpha\, u_i - \gamma\, \theta_i - \delta\, \dot{\theta}_i \quad .\tag{2.1}$$

It generates a torque τ_i in the i-th joint of the segmented body. It is derived from a antagonist

muscle pair, modeled as linear spring-dampers and contains motoneuron activation (u_i), an activation gain (α), stiffness (γ) and damping (δ). The stiffness and damping terms contribute to a (passive) viscoelastic behavior of the robot depending on the kinematic state of the body (joint angle θ_i and angular speed $\dot{\theta}_i$), whereas the activation allows to influence the internal torque. The muscle model in Ekeberg's original contribution contained an additional actively controlled stiffness term (co-contraction of muscles), that we omit here.

Active control originates from Central Pattern Generators (CPGs). Many types of models exist for those CPGs, from highly elaborate Hodgkin-Huxley-like models (Rybak et al., 2002; Ivashko et al., 2003) to more elementary neuron models (Knüsel et al., 2013; Bicanski et al., 2013). We use simple phase oscillators in this study, as we are interested in questions about the role and importance of inherent neural oscillations for undulatory locomotor control. Equations (2.2) and (2.3) define the model dynamics.

$$u_i = cos(\phi_i) \quad , \tag{2.2}$$

$$\dot{\phi}_i = \omega + \underbrace{\sigma_1 \sum_{j=1}^{N} w_{ij} sin(\phi_i - \phi_j - \psi_{ij})}_{A} + \underbrace{\sigma_2 w_{fb} F_i cos(\phi_i)}_{B} \quad . \tag{2.3}$$

To reduce the complexity, we consider a single chain of oscillators (as opposed to a double chain, Grillner et al. 1995) along the body with one oscillator for each joint of the robot model (Figure 2.3). Consequently, u_i represents the activation signal of the contralateral muscles of either the left ($u_i < 0$) or the right ($u_i > 0$) side at the joint i. The phase of the activation signal is given by ϕ_i, and ω denotes the intrinsic oscillator frequency, which can be modulated by descending drives from the brainstem (Cabelguen et al., 2003).

Besides local neural oscillators themselves, we are also interested in the modulation and interaction between oscillators. Thus, central coupling between CPGs, which is present in lampreys (Cohen et al., 1992; Matsushima and Grillner, 1992) and leeches (Cang and Friesen, 2002) was implemented (equation 2.3, A) by coupling the phases of activation based on defined phase shifts ψ_{ij} (Ijspeert et al., 2007). To enclose the coupling locally, we exclusively consider nearest neighbor coupling (w_{ij}) between oscillators.

In addition to local couplings we consider sensory inputs which modulate the CPGs for locomotion control. In this study we take into account the pressure changes along the body, and consequently equipped the mechanical model with pressure sensors on the left and right sides of each segment. We examine how the measurement of pressure difference between contralateral sides can contribute to adaptive undulatory swimming. Based on the sensed contralateral pressure difference in one segment, one can estimate that a corresponding resulting external force is exerted. On a very local level, the force indicates from which side the surrounding water is pushing (or pulling) the body. The principal goal of the feedback loop is to locally modulate the activation in the corresponding muscles depending on the pressure measurements they receive and the current state of the muscles. This is schematically

illustrated in Figure 2.2. At this point there is no biological evidence for such pressure feedback loops, however we hypothesize that similar mechanisms might exist related to the lateral line organ (Ristroph et al., 2015) or that corresponding mechanisms could also indirectly relate to local stretch receptors.

Ideally, muscle activations should follow a pattern which drives the local body segments in a sequence $A \rightarrow B \rightarrow C \rightarrow D$. This could be achieved with a simple open loop oscillator that constantly increases the phase. However, it is crucial that the appropriate external forces which are beneficial for forward locomotion are generated while going through the different states of contraction. Therefore, we propose the following feedback loop that depends on the local state of contraction: Progression to the next state (increase of phase speed) is encouraged when the measured external force is appropriate for forward locomotion. Waiting or going back (decrease of phase speed) to a previous state is favored when the forces are not desirable. In our model, this sensory feedback mechanism is incorporated in equation (2.3, B), where F_i denotes the estimated resulting force proportional to the pressure difference and w_{fb} represents the feedback gain. Using σ_1 and σ_2 we can modulate the influence of coupling between oscillators vs feedback, with respect to the phase.

2.2.2 Details of the feedback rule

Desired force distribution

As explained in section 2.2.1, our proposed feedback rule relies on a desired force distribution along the body during undulatory swimming. To explain the force profile along the body it is useful to introduce two definitions first:

1. *Body inflection point:* During undulatory locomotion, waves of undulation pass through the body. Freezing the movement at a given time instance, one can observe locations which are maximally bent and locations which are almost straightly aligned. We define the latter areas as *body inflection points*, as at those characteristic points the body bending along the body switches the side (e.g. from left to right). At the same time these points are the node of the undulatory traveling wave.

2. *Force inflection point:* Assuming the body is performing a periodic undulatory movement, forces along the body are also going through a periodic time course. Zero force will occur in this process, as the forces switch signs (pushing/pulling from the left or the right of a segment). We define the location along the body where zero external force occurs as *force inflection point*.

The force profile along the body is given in Figure 2.2 and based on observations from open loop swimming with 100% phase lag (one complete wave along the body). Thus, the body and force inflection points coincide. At the same time, the absolute force maxima occur in the maximally bent body areas.
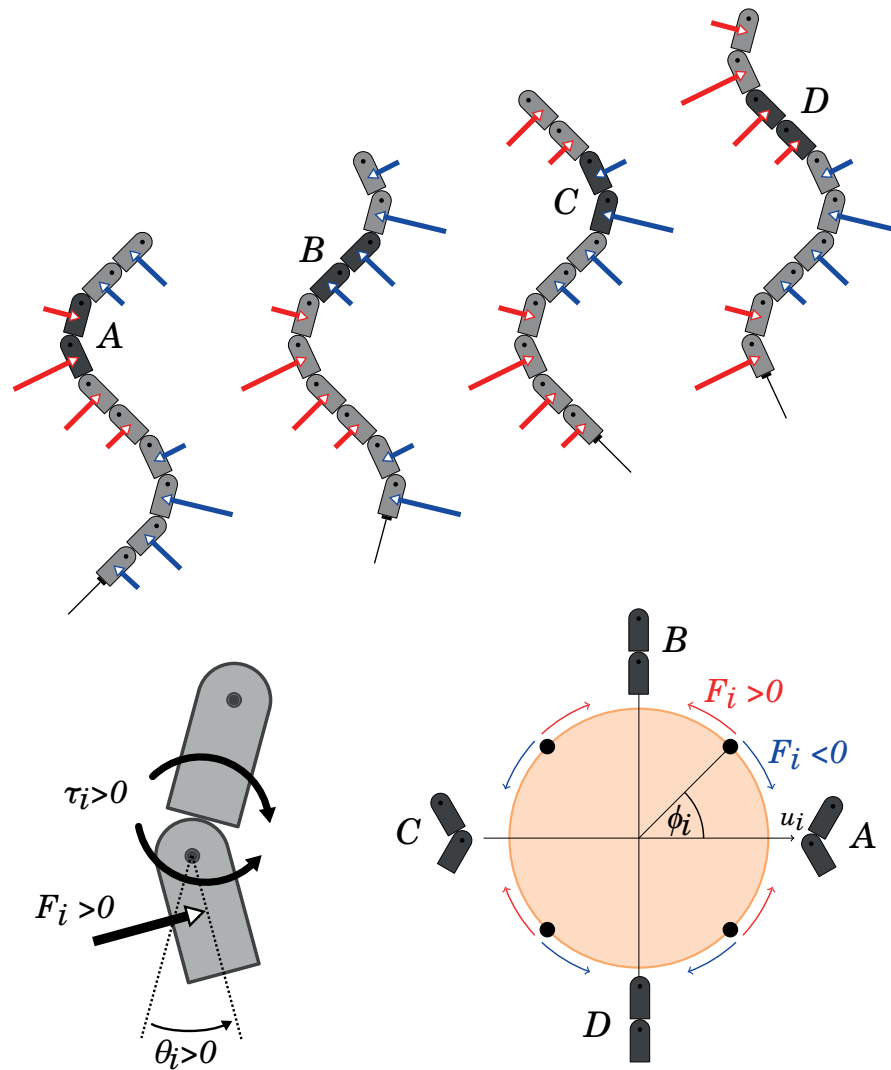
Figure 2.2 – **Working principle of the sensory feedback loop**. **(top)** Red ($F_i < 0$) and blue ($F_i > 0$) arrows indicate desirable external forces from the water for forward undulatory locomotion. The forces are estimated based on measurements of pressure on contralateral sides of a segment. **(bottom right)** Illustration of the phase ϕ_i on the unit circle. Activation $u_i = cos(\phi_i)$ is determined as projection onto the x-axis, where positive values indicate contraction to the right (A) and negative values show contraction to the left (C). The feedback accelerates the phase when the corresponding forces are desirable and slows down the rythm when forces are non-desirable. **(bottom left)** Conventions for segments around joint i with Force F_i, torque τ_i and joint angle θ_i.

Open loop behavior

To understand the feedback rule, it is useful to study the open loop behavior on the unit circle first. Let us consider the following reduced system (without central coupling and feedback):

$$\dot{\phi}_i = \omega \quad , \tag{2.4}$$
$$u_i = cos(\phi_i) \quad . \tag{2.5}$$

As shown in Figure 2.2, the behavior of the system described above can be represented on the unit circle. The constant increase of the phase ϕ_i drives the phase from 0 to 2π, which will lead the activation as defined in equation (2.5) from $u_i = 1$ (maximal bending to the right) to $u_i = 0$ (body inflection point B), to $u_i = -1$ (maximal bending the left) to $u_i = 0$ (body inflection point D) and back to $u_i = 1$.

Feedback rule

The proposed feedback rule has the goal of synchronizing the oscillatory muscle activation with the desired force profile along the body. At a given joint, for a given force measurement, the corresponding phase is manipulated in such a way that it is encouraged to progress if the measured force matches the desired one at that phase instance and slowed down otherwise. In detail this can be explained as follows by looking at the different quadrants in the unit circle:

- 1. Quadrant ($A \rightarrow B$): Ideally, the two segments progress from maximal bending to the right to the body inflection point B, while experiencing external forces from the left ($F_i > 0$).

- 2. Quadrant ($B \rightarrow C$): Following the desired force distribution, B is both a body as well as a force inflection point. Therefore, in this quadrant the phase is encouraged to progress, when the measured force is pushing from the right ($F_i < 0$).

- 3. Quadrant ($C \rightarrow D$): The desired forces in this quadrant are again negative and should decrease towards the force inflection point in D.

- 4. Quadrant ($D \rightarrow A$): Phase is increased by the feedback when the forces are increasingly positive towards maximum force from the left at a maximal bending to the right.

The corresponding rule to achieve the desired feedback behavior is described by manipulating the phase with $\dot{\phi}_i = ... + F_i \cdot cos(\phi_i)$.

2.3 Methods

2.3.1 Simulated model

We modeled the elongated swimming body in Webots 6.4.4 ((Michel, 2004), Cyberbotics Ltd., Lausanne, Switzerland). Webots is a simulator based on the ODE (Open Dynamics Engine). It provides a simulation environment for rigid bodies, which can be linked and constrained to one another, as well as actuated by servo motors or user-defined external forces. Besides predefined contact models between objects (e.g. friction), Webots also offers custom definition and implementation of physics via ODE, which we used to simulate hydrodynamic forces.

Our segmented elongated swimming body consists of 10 identical body segments with an additional segmented tail. The body segments are linked with 2-dimensional hinge joints which restricts the movements of the swimmer within a plane. The tail segments are also connected via the same type of hinge joints. The tail joints have spring-damper properties and are passive (not actively controlled). Corresponding dimensions and weights as well as tail stiffness and damping are given in Table 2.1. As defined in section 2.2.1 and equation (2.1), the segmented body is actuated by torques in the joints between body segments. We refer the reader to simulations that were performed with a 20-segment-model without tail. Additional corresponding results can be found in chapter B. The segment geometries and weights follow the ones of our robot model.

Characteristics	Body segment	Tail segment
Count	11 (21*)	5 (0*)
Shape	cube + half cylinder	cube
Dimensions [cm]	$4.5 \times 5.9 \times 7.25$, $r = 2.25$	$0.1 \times 5.9 \times 2.49$
Mass [kg]	0.22 (0.094**)	0.0013
Stiffness [Nm/rad]	variable	2
Damping [Nms/rad]	variable	0

Table 2.1 – Dimensions and properties of the simulated elongated body for undulatory swimming. * indicates the number of segments for the 20 joint model and ** denotes the mass for the head segment.

2.3.2 Hydrodynamics

We consider buoyancy as part of the hydrodynamics model. This is related to the immersion in water. As a consequence the swimming body will occupy a specific volume in water. According to Archimedes' principle, this leads to a buoyant force counteracting the gravitational force equal to the weight of the displaced water. Hence, aquatic organisms, can in a way compensate their weight by their volume, which also explains the impressive sizes of uniquely big animals such as the blue whale. Since we model surface swimming (based on restriction of our robot model), we have a small positive buoyancy in our simulations.

Whereas, buoyant forces act mainly normal to the water surface, propulsion of an elongated swimmer originates from a variety of different mechanisms such as vorticity, inertial and viscous forces. An accurate model of fluid flow and the corresponding exerted forces on a swimmer would require to solve the N-S-equations. However, as they remain analytically unsolvable to date and numerical solutions prove to be computationally costly, we use a recently published hydrodynamics model proposed by Porez et al. (2014). This model is based on Lighthill's large amplitude elongated body theory (Lighthill, 1971) and considers reactive forces stemming from the acceleration of the fluid moved by the swimming body, as well as resistive (drag) forces from viscous stresses in the boundary layer of the body. The model has been tested and validated with swimming kinematics of Amphibot, an anguilliform swimming robot. Furthermore, the authors of that work apply a Newton-Euler modeling approach which allows for numerical integration in real-time. These advantages justified the use of this particular hydrodynamics model in our study. For further details, the reader is referred to the corresponding publication by Porez et al. (2014).

For completeness (not used in our simulations), we mention here also another simpler model that has been used to study lamprey locomotion, namely in Ekeberg (1993). It considers solely resistive drag forces $F \sim v^2$, where v denotes the speed of a respective body moving in a fluid. Important considerations are further the drag coefficients which depend on shape and surface properties. In models for elongated swimmers, one can assume that the drag coefficients in axial segment direction are significantly smaller than in lateral direction.

2.3.3 Metrics for characterization

In order to characterize and evaluate the performance of the segmented swimming body for different undulatory control strategies, we introduce several metrics that describe the movements of the body with respect to the environment, but also the relative internal movements of the body.

Frequency

Except for the open loop control scheme in which the control frequency of locomotion is directly given by the intrinsic oscillator, frequency is an emergent property. It is defined by the interaction between oscillators and the local feedback loops that influence the phase of the activation signals. Assuming straight swimming (due to symmetric control scheme, as explained later), the zero-crossings of the joint angles provide sufficient information about the period of their rythmic pattern. We then arbitrarily consider periods between zero-crossings from positive to negative joint angle values, within a given estimation time frame. The frequency is

determined by the average period over different joints angles:

$$f = \frac{1}{\sum_{i=1}^{N} \sum_{k=1}^{K} T_{i,k}^{\Delta t_{est}}} \quad , \tag{2.6}$$

where f denotes frequency and $T_{i,k}^{\Delta t_{est}}$ describes the $k-th$ period in the measurements of joint i during an estimation time interval of Δt_{est} seconds.

Speed

The speed of locomotion is computed based on the absolute traveled distance within one gait cycle (and therefore requires a frequency estimation beforehand). The direction (forward/backward) is determined by the projection of the progression vector in one cycle and the current tail-to-head vector:

$$v = sign(\vec{d} \cdot \vec{r}) * |d| * f \quad , \tag{2.7}$$
$$\vec{d} = \vec{p_h}(t) - \vec{p_h}(t - T) \quad , \tag{2.8}$$
$$\vec{r} = \vec{p_h}(t) - \vec{p_t}(t) \quad , \tag{2.9}$$

where v denotes the current speed, $\vec{d}$ the progression vector, $\vec{r}$ the current tail-to-head vector, f the frequency (T the corresponding period), and $p_h(t)$ and $p_t(t)$ the head and tail positions at time t, respectively. The current mean speed is estimated as the average over the last two cycles.

Cost of Transport (COT)

This metric relates expended energy of a system to the locomotor progression it goes through and is defined as follows:

$$CoT = \frac{E \cdot f}{m \cdot g \cdot v} \quad , \tag{2.10}$$
$$E = \sum_{i=1}^{N} \int_{t}^{t+T} W(t) dt \quad , \tag{2.11}$$

where E denotes the used energy, $f = \frac{1}{T}$ the gait frequency, m the mass, g the gravitational acceleration and v the speed. The energy is defined in terms of mechanical work, with the

torque $\tau_i(t)$ and the corresponding joint angle velocity $\dot{\theta}_i(t)$ of the joint i at time t. We compute the COT for one cycle in steady state. For convenience, we define also the following quantities:

$$E_{pos} = \sum_{i=1}^{N} \int_{t}^{t+T} W_{pos}(t)dt \quad , \tag{2.12}$$

$$W_{pos}(t) = \begin{cases} \tau_i(t) \cdot \dot{\theta}_i(t) & , \text{for } \tau_i(t) \cdot \dot{\theta}_i(t) > 0 \\ 0 & , \text{for } \tau_i(t) \cdot \dot{\theta}_i(t) \leq 0 \end{cases} \quad , \tag{2.13}$$

$$E_{neg} = \sum_{i=1}^{N} \int_{t}^{t+T} W_{neg}(t)dt \quad , \tag{2.14}$$

$$W_{neg}(t) = \begin{cases} 0 & , \text{for } \tau_i(t) \cdot \dot{\theta}_i(t) \geq 0 \\ \tau_i(t) \cdot \dot{\theta}_i(t) & , \text{for } \tau_i(t) \cdot \dot{\theta}_i(t) < 0 \end{cases} \quad , \tag{2.15}$$

where E_{pos} and W_{pos} define positive energy and work, and E_{neg} and W_{neg} the corresponding negative counterparts. Finally we define the total spent energy if negative work can be fully restored as follows:

$$E_{tot} = E_{pos} + E_{neg} \quad . \tag{2.16}$$

Phase lag

Assuming periodic oscillations in the different joints along the body, one way to characterize their coordination pattern is to look at the differences in relative phases between them. One can consider the individual intersegmental phase lags or the overall phase lag from head to tail. Both are related to the number of waves traveling along the body. We defined the overall phase lag $\Delta\Phi$ along a body in our simulations as follows:

$$\Delta\Phi = \frac{1}{2\pi} \sum_{i=1}^{N-1} \Delta\phi_i \quad , \tag{2.17}$$

where $\Delta\phi_i$ denotes the intersegmental phase lag from joint i to $i+1$ in radians. We compute the intersegmental phase lags based on the phase lags between zero-crossings of consecutive joints. Moreover, we distinguish the phase lag $\Delta\Phi_{act}$ in the activation signals (inputs to the muscle model) and $\Delta\Phi_{kin}$ in the joint angles (kinematics).

2.3.4 Exploration of model parameters

Our results are based on extensive parameter variations of our neuromechanical model in order to characterize the proposed control schemes (explained in section 2.4) and quantify them with respect to different performance metrics (see section 2.3.3). The model parameters of interest are related to central coupling, feedback, muscle model and environmental conditions. A list of parameters and corresponding ranges is presented in Table 2.2 for a series of simulations that have been performed for the different models, respectively.

Setting	f [Hz]	α [Nm]	γ [Nm/rad]	$\Delta\Phi_{nom}$ [%]	w_{fb} [-]
Open loop	0.5:0.25:2	0.5:0.5:2	1.0:0.5:2	-50:10:250	-
Combined model (I)	0.5:0.25:2	0.5:0.5:2	1.0:0.5:2	-50:10:250	1
Decoupled model (II)	0.5:0.25:2	0.5:0.5:2	1.0:0.5:2	-	1
Sensory-driven model (III)	-	0.5:0.5:2	1.0:0.5:2	-	1:0.5:3

Table 2.2 – Parameter exploration (minimum value : step size : maximum value) for the different undulatory swimming control schemes

2.4 Results

Given our proposed neuromechanical model, we investigated three distinct control model topologies as shown in Figure 2.3:

- (I) *Combined model* - represents a model based on CPGs with central coupling and local sensory feedback

- (II) *Decoupled model* - denotes a scheme with decoupled CPGs and local sensory feedback

- (III) *Sensory-driven model* - serves as a model without neural oscillators but central coupling between segments and local sensory feedback.

In all the topologies, the local sensory inputs are present and result from local contralateral pressure differences along the swimming body.
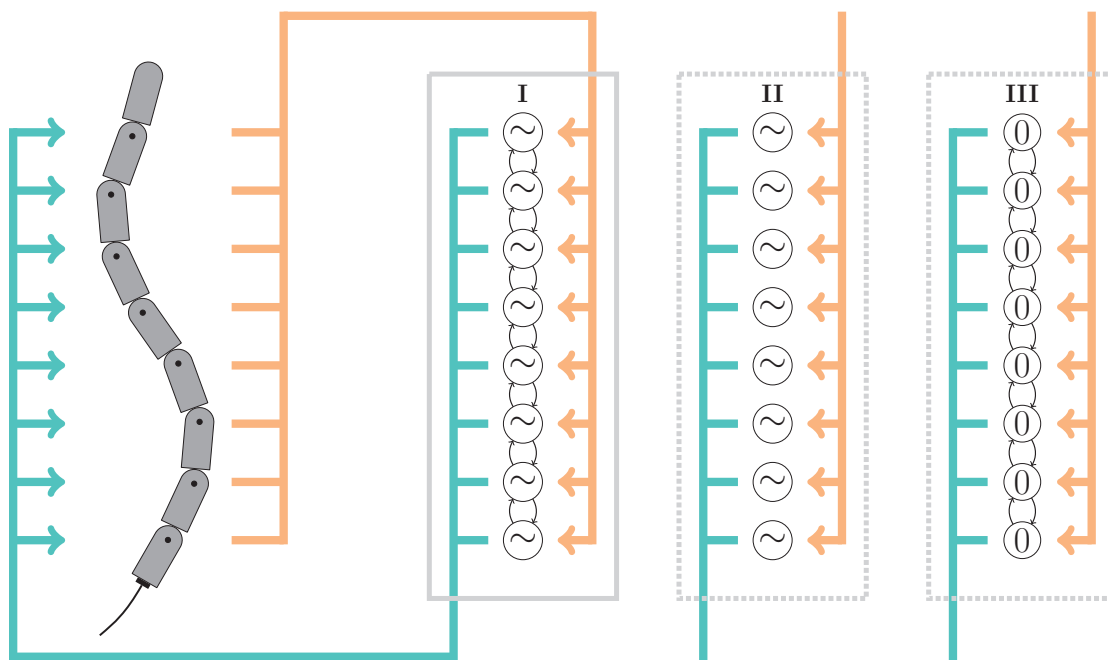
Figure 2.3 – **Control paradigms for undulatory swimming**. **(I)** *Combined model* with neural oscillators (CPGs), central coupling and local sensory feedback. **(II)** *Decoupled model* based on decoupled neural oscillators and local sensory feedback. **(III)** *Sensory-driven model* only based on local sensory feedback and central coupling between joints. All models include sensory feedback loops exploiting pressure differences on contraleral sides of the body. Light green arrows indicate motor outputs, Light orange arrows define sensory inputs.

2.4.1 Local pressure feedback can reshape and correct phase-lag patterns

We first examined locomotion control for undulatory swimming based on centrally coupled CPGs influenced by local sensory inputs (Fig. 2.3, *Combined Model* I). As it is known from salamanders (Delvolvé et al., 1999; Knuesel, 2013), the variability of intersegmental phase lags in isolated spinal cord preparations is large. Forward and backward traveling waves as well as standing waves have been observed. In intact animals however, the observed phase lags are in a much narrower range. It can be hypothesized that these particular characteristics are a product of the closed loop system in the animal, which incorporates sensory feedback mechanisms. With our neuromechanical model, we therefore asked to what extent the sensory inputs influence a variety of open loop patterns, which in our model are represented by fixed phase lags in the central coupling between oscillators. To evaluate the effects of the sensory feedback, we compared open loop swimming gaits with corresponding closed loop gaits. We measured locomotion speed, and emerged phase lags and frequencies (Definition of metrics, see section 2.3). Results are shown in Figures 2.4, 2.5 and 2.6 for the 10-joint and for the 20-joint model. The key differences between these two models are the distinct number and the absence of a tail fin for the 20-joint model. The analysis for the model with the higher number of joints was motivated, as we wanted to reduce the effects of the passive tail fin and explore the effects of a more finely segmented body, that brings more challenges in terms of intersegmental synchronization.

In open loop, we notice different characteristic speed performances for the short and the long model with different optimal number of waves along the body. Whereas for the short model a clear peak towards one wave (100% phase lag) is observed, the long model has two peaks in general and one peak for higher frequencies. The two peaks are located near 100% and 200% phase lag. In both models, the speed drops drastically for higher numbers of waves, i.e. higher phase lags, along the body. Closed loop swimming with local sensory pressure feedback can correct many of the suboptimal phase lag patterns by imposing wave numbers around 100% for the short and around 200% for the long model. Overall, the performance of the local feedback brings more improvement in the case of the long model, as in closed loop, high speeds over the entire spectrum of phase lags are achieved ($[0.59, 0.75]$ m/s). These come close to the maximum speed peaks of the open loop model (0.8 m/s). Similar characteristics are observed for the short model, however a saturation of speeds is visible. At high frequencies (1.75 and 2 Hz) the speed peaks of the open loop are clearly outperforming the feedback solution.

We observed that adding feedback increased frequencies and thus, increased oscillatory rhythms compared to open loop patterns, which is consistent with observations in lampreys and leech (Friesen and Cang, 2001). Nonetheless, it is important to note that the speed-optimal swimming behavior for local feedback-induced coordination patterns, originates not only from faster rhythms but also from adapted phase lag patterns. Especially for high nominal phase lags the frequency increase does not explain the significant increase of speed. Adapted phase lag patterns (and also respective amplitude patterns) contribute as well. In Figure 2.7

we show an example of how a nominally "*wrong*" large phase lag gets corrected by the local feedback mechanism. This can be seen in the activation patterns as well as in the snapshot sequence where initially two body waves are present and eventually are corrected to one body wave.

We conclude that the local pressure feedback can correct various nominal phase lags to more beneficial regimes such as one or two body waves along the body. In addition, the feedback loops lead to increased oscillator rhythms and overall high speeds are achieved. The results also indicate that such a closed loop system is beneficial for different body morphologies as we have found qualitatively similar characteristics for a short and a more finely segmented body.

(a) 10-joint model

(b) 20-joint model

Figure 2.4 – ***Combined model I in comparison with open loop patterns***. Evaluation of open and closed loop performance for same fixed phase lag values and same parameters for the 10 and 20 joint models. Muscle parameters correspond to $\alpha = 1$ Nm, $\gamma = 2$ Nm/rad, $\delta = 0.1$ Nms/rad and $w_{fb} = 1$. Connected lines show open loop data, filled markers indicate *Combined model* I (closed loop) measurements. Same colors indicate corresponding same neural oscillator frequencies. (**left**) Mean speed (**middle**) Emerged frequency (**right**) Emerged average phase lag.
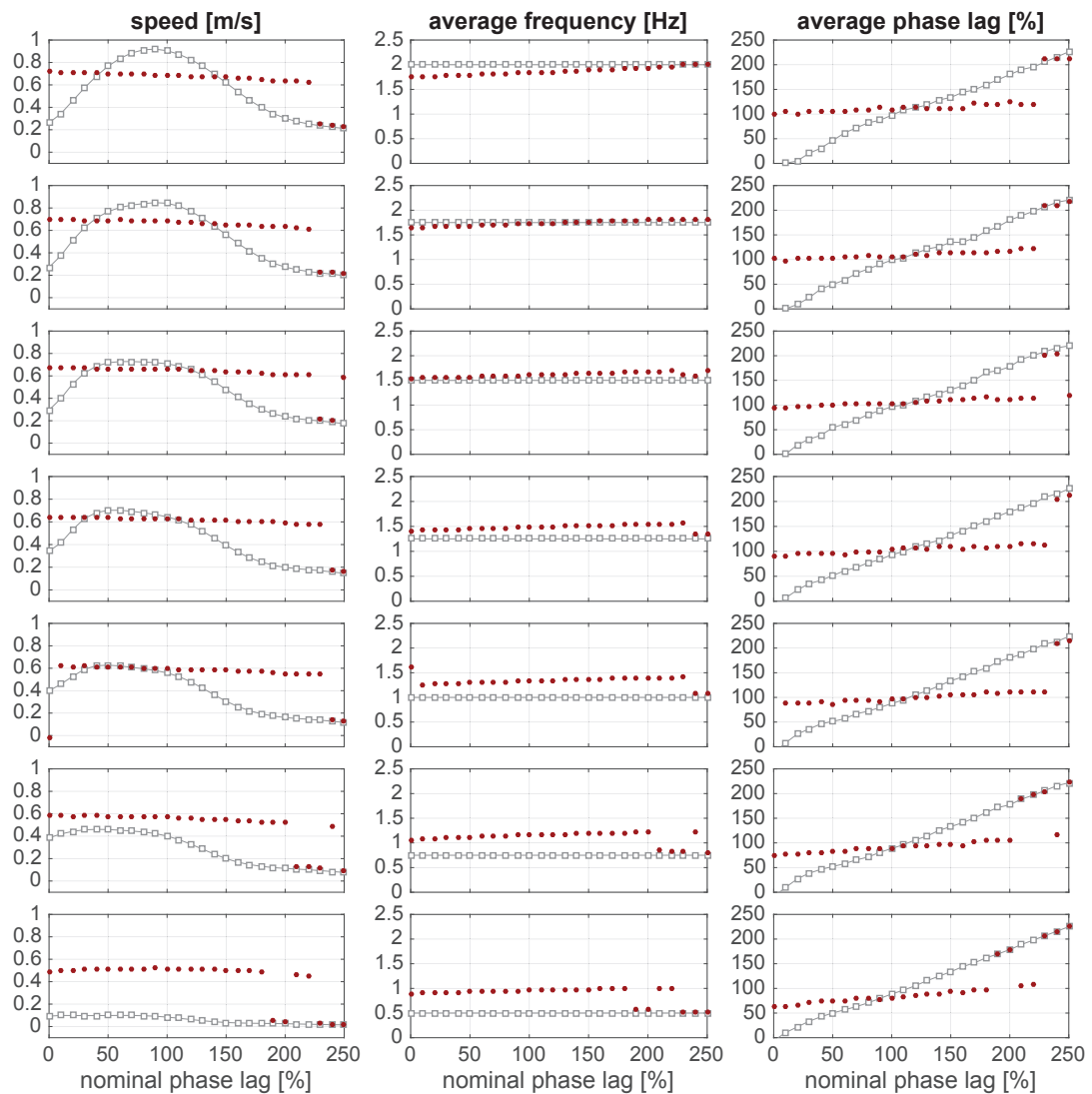
Figure 2.5 – *Combined model* **I in comparison with open loop patterns - 10-joint model**. Evaluation of open and closed loop performance for same fixed phase lag values and same parameters. Muscle parameters correspond to $\alpha = 1$ Nm, $\gamma = 2$ Nm/rad, $\delta = 0.1$ Nms/rad and $w_{fb} = 1$. Connected lines show open loop data, filled markers indicate Model I closed loop measurements. (**left**) Mean speed (**middle**) Emerged frequency (**right**) Emerged average phase lag.
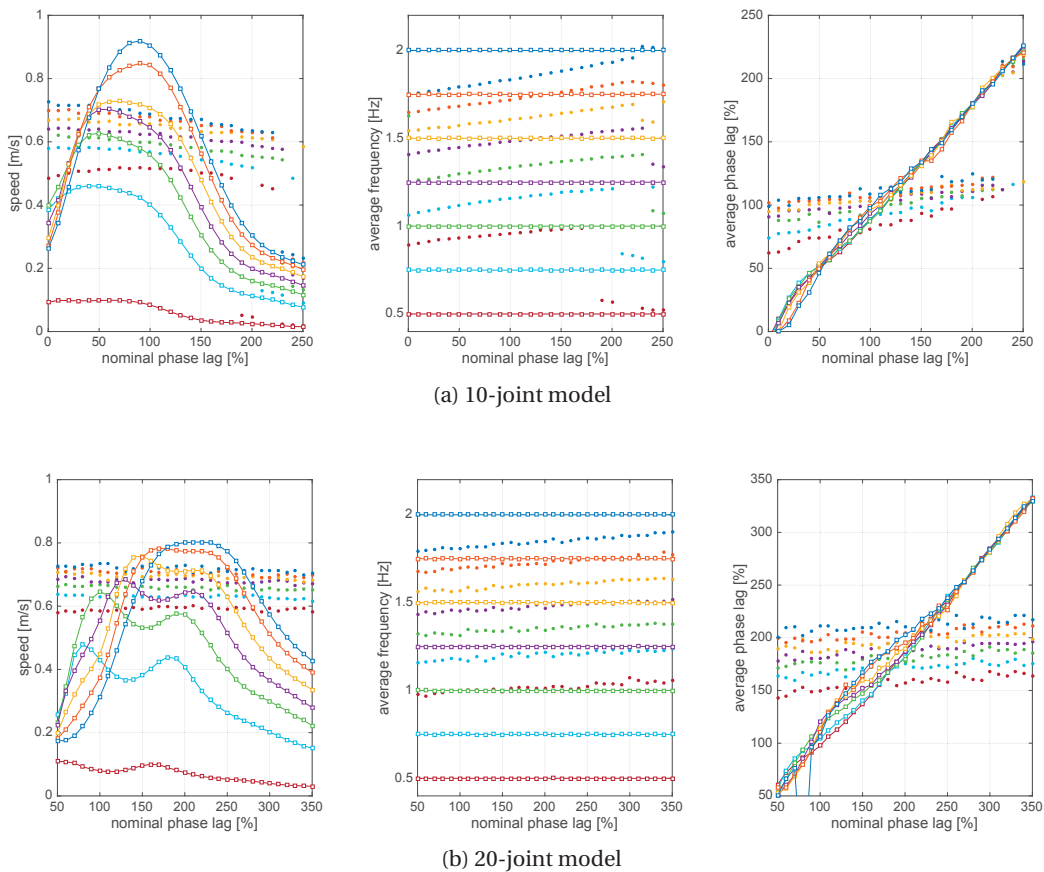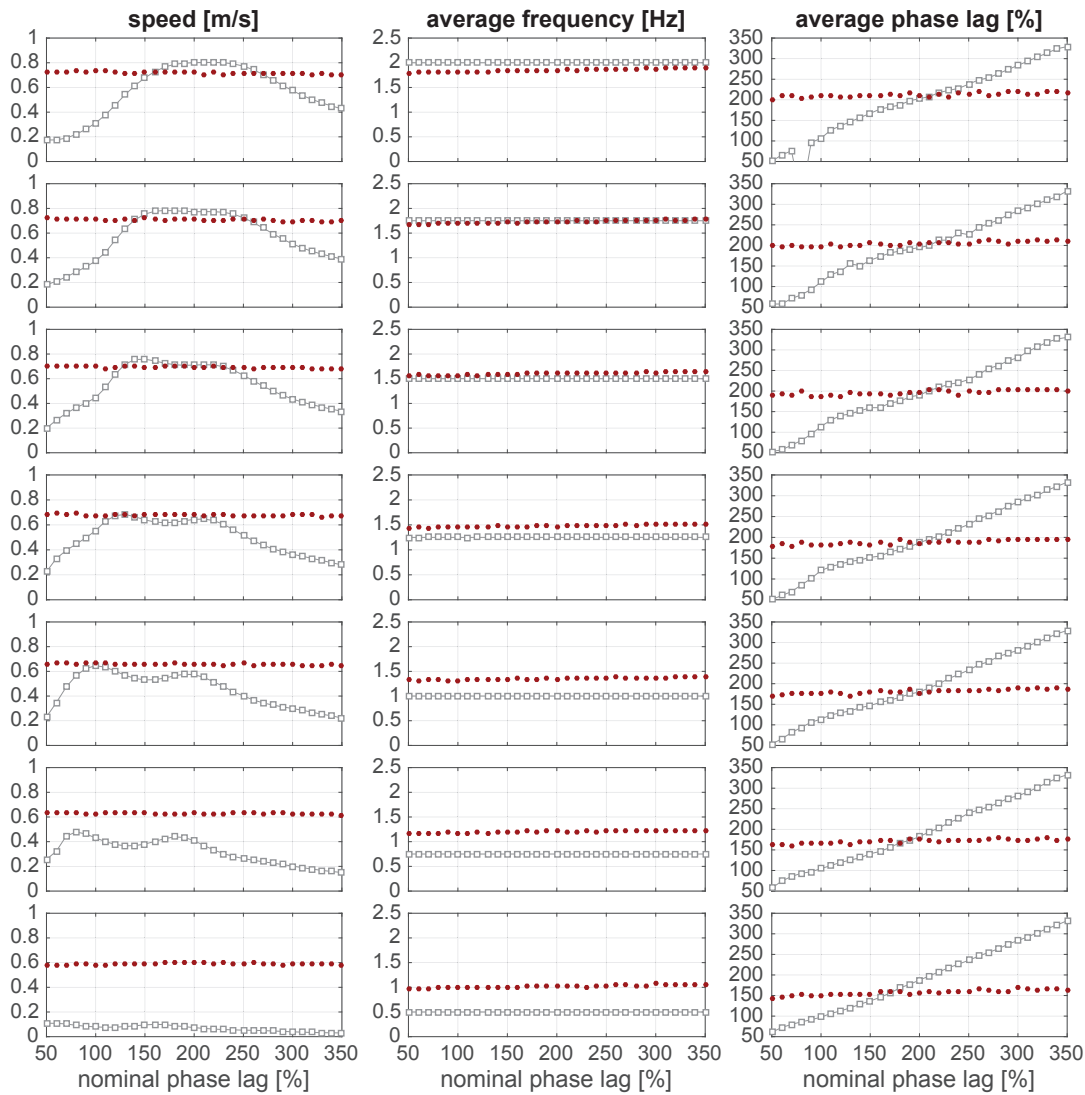
Figure 2.6 – *Combined model* **I in comparison with open loop patterns - 20-joint model**. Evaluation of open and closed loop performance for same fixed phase lag values and same parameters. Muscle parameters correspond to $\alpha = 1$ Nm, $\gamma = 2$ Nm/rad, $\delta = 0.1$ Nms/rad and $w_{fb} = 1$. Connected lines show open loop data, filled markers indicate Model I closed loop measurements. (**left**) Mean speed (**middle**) Emerged frequency (**right**) Emerged average phase lag.

Figure 2.7 – **Emergence of undulatory swimming for the *Combined model* I**. (**A**) Shows a plot of the activation dynamics over the course of 4 seconds in corresponding colors over time along with the kinematics in terms of joint angles in black lines. (**B**) 20 Snapshots over the course of the same 4 seconds show the evolution of an undulatory swimming pattern with parameters $\alpha = 1$ Nm, $\gamma = 2$ Nm/rad, $\delta = 0.1$ Nms/rad, $f = 1.5$ Hz, $\Delta\Phi = 200\%$ and $w_{fb} = 1$. Red ($F > 0$) and blue ($F < 0$) arrows denote external forces from the water, light orange and light brown bars along the body indicate that muscles on the respective sides are contracted.

2.4.2 Decoupled oscillators together with local pressure feedback lead to well-coordinated swimming behavior

Decentralized control has been investigated in various previous works and has proven to explain locomotor modes of different kinds (Owaki et al., 2013; Cruse et al., 2007). With our neuromechanical model we wanted to investigate to what extent such a decentralized control scheme, relying on pressure measurements, could generate undulatory swimming. For this purpose we removed the central coupling in our model and analyzed a model purely based on local oscillators and sensory feedback (Fig. 2.3, *Decoupled model* II). Our motivation was, as observed in Owaki et al. (2013), that the neural oscillators subject to sensory inputs, would synchronize with the forces exerted by the water and thus exploit the natural dynamics of the environment.

We found that coordinated swimming emerges spontaneously. Figure 2.8 shows an example of this emergent behavior. Starting from a straightly aligned body position and decoupled local oscillators, the local pressure feedback succeeds in modulating the phases of the CPGs such that the desired force distribution along the body is attained. Thus, bending to the left induces opposing reaction forces from the left and analogously for right side bending. As a result traveling waves of (neural) activation from head to tail are generated (Figure 2.8). The corresponding kinematic wave (local body bending) has a slight phase lag with respect to the neural wave, which is expected due to stiffness and damping effects and the fact that the joints are controlled via torques applied in the joints (with relatively low gains). In previous studies also different propagation speeds of the neural and kinematic have been observed (McMillen et al., 2008), in our results this is less evident, and is most likely related to the choice of muscle parameters.

The emergent behavior in this control scheme has several advantageous characteristics. Figure 2.9 presents a comparison of the different models in terms of speed, Cost of Transport (COT, definition in section 2.3.3) and average phase lag. We show the latter two characteristics selectively for fast swimming gaits across different models (above the dashed-threshold line in Figure 2.9, left). The first observation is that the phase lags for the decoupled oscillator model converge to a similar range as the proposed *Combined model* I (Figure 2.9, right), which is beneficial for fast swimming. Figure 2.9 (left) confirms this, as the emerged speeds can compete with the *Combined model* I and with the fastest swimming speeds that were observed for open loop swimming. Measures of COT show that the emergent coordinated behavior is at the lower bound among the selected gaits, indicating that high speeds along with low COT are obtained for this model.

We also carried out the same analysis for the longer model with 20 joints and obtained similar results (Appendix B, Figure B.1). In summary, the local decoupled oscillator model modulated by local pressure feedback leads to coordinated swimming with approximately one body wave traveling from head to tail. In addition, measurements indicate that the swimming behavior is fast and energy efficient.
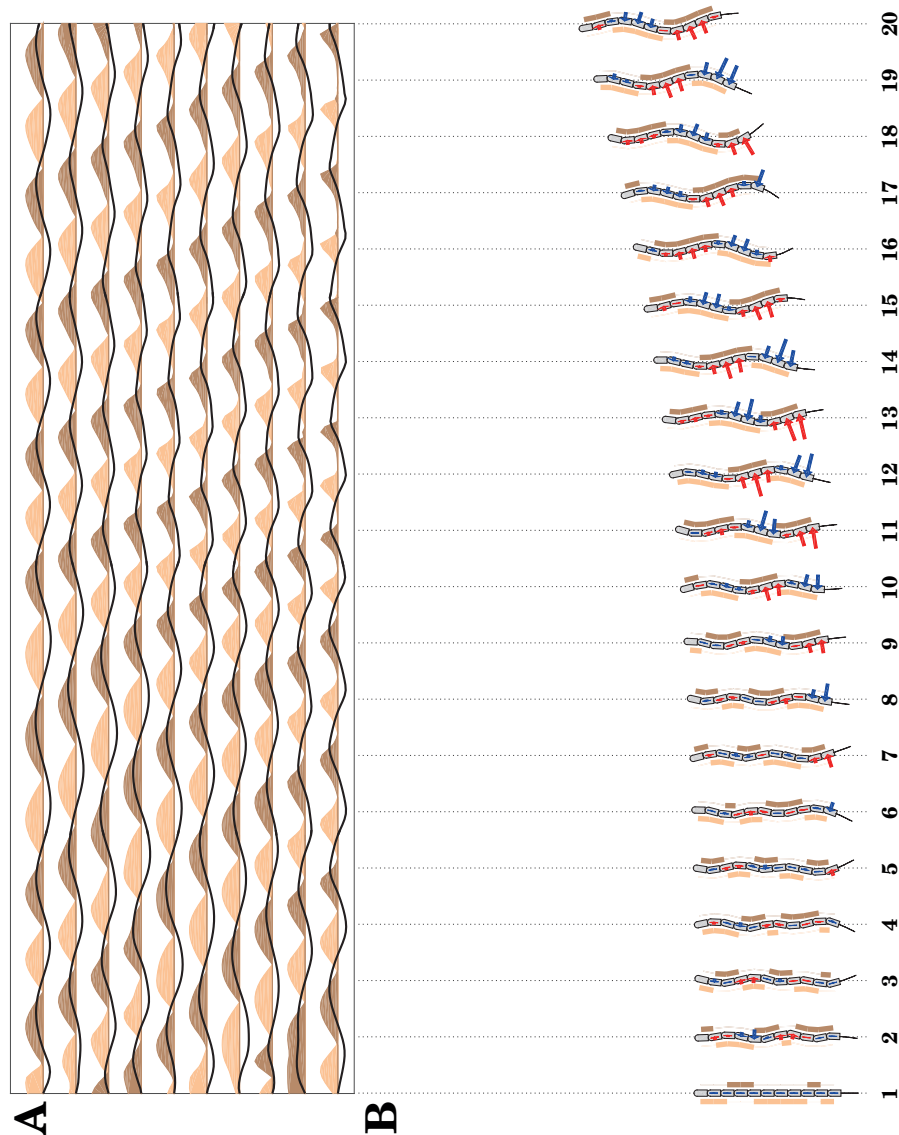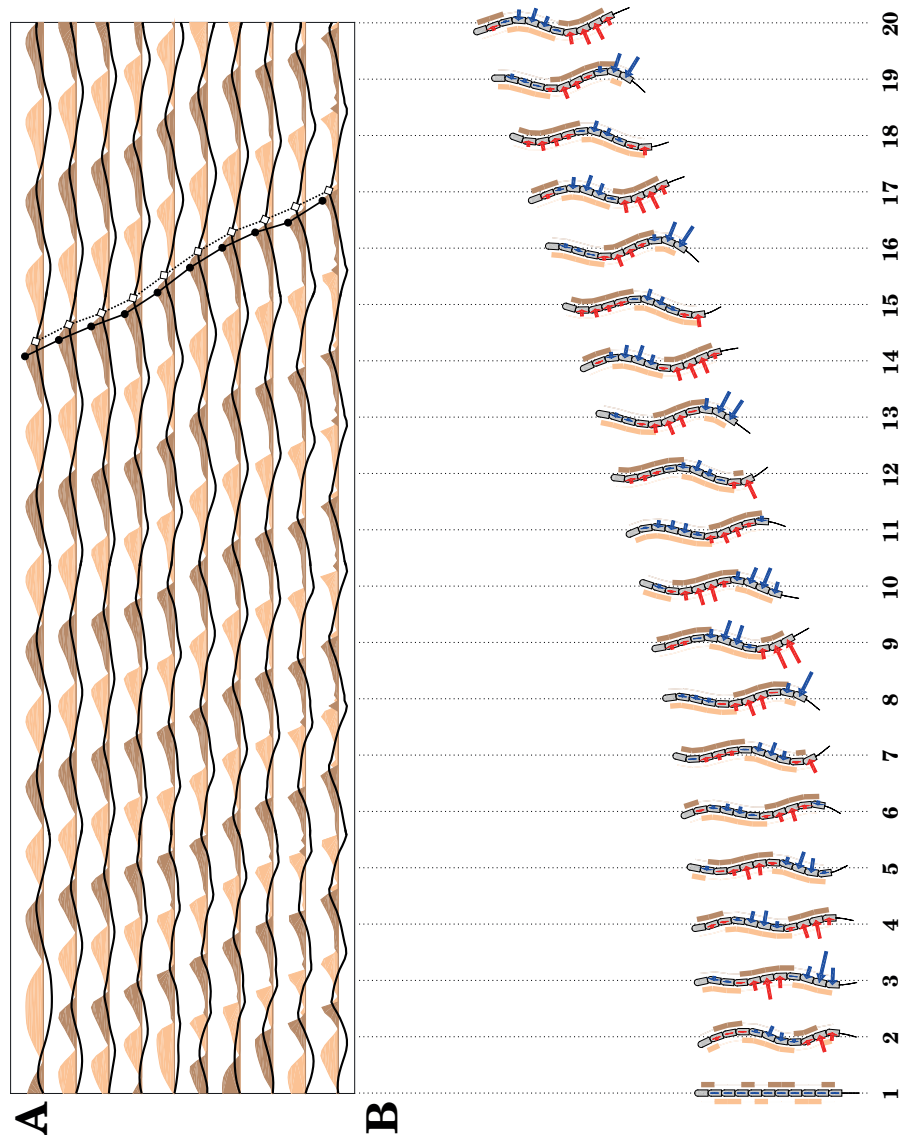
Figure 2.8 – **Emergence of undulatory swimming for the *Decoupled model* II**. (**A**) Shows a plot of the activation dynamics over the course of 4 seconds in corresponding colors over time along with the kinematics in terms of joint angles in black lines. The filled circles indicate maxima of the signals for activation (connected by solid line) and kinematics (white diamonds, dashed line) and visualize the phase lag between segments as well as the time delay between neural and kinematic wave. (**B**) 20 Snapshots over the course of the same 4 seconds show the evolution of an undulatory swimming pattern with parameters $\alpha = 1$ Nm, $\gamma = 2$ Nm/rad, $\delta = 0.1$ Nms/rad, $f = 1.5$ Hz. Red ($F > 0$) and blue ($F < 0$) arrows denote external forces from the water, light orange and light brown bars along the body indicate that muscles on the respective sides are contracted.
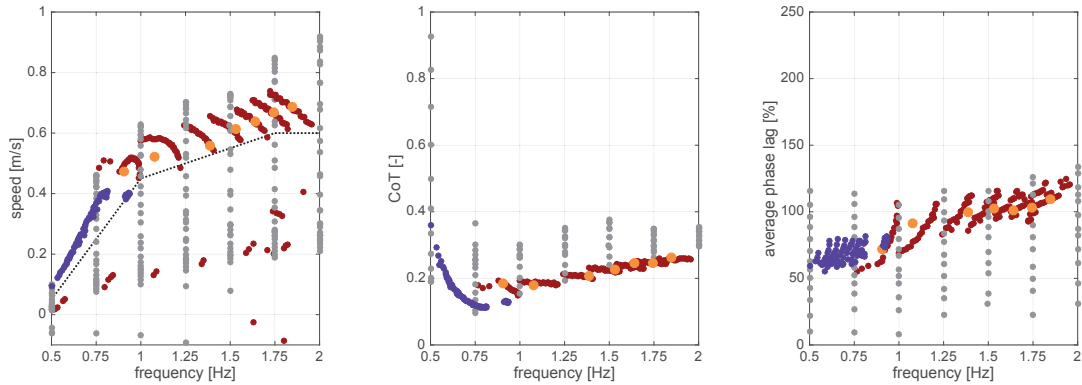
Figure 2.9 – **Comparison of Models I, II, III and open loop - 10 joint model**. Open loop patterns (gray), *Combined model* I (red), *Decoupled model* II (orange) and *Sensory-driven model* III (purple). Muscle parameters for Open loop, model I, II and III correspond to $\alpha = 1$ Nm and $\gamma = 2$ Nm/rad, $\delta = 0.1$ Nms/rad and $w_{fb} = 1$. For the *Sensory-driven model* III nominal phase lags as well as feedback gains were varied. Based on a threshold minimum speed for different frequencies (dashed line), only COT and average phase lags above this threshold are presented. (**left**) Mean speed (**middle**) Cost of transport (**right**) Emerged average phase lag.

2.4.3   Local pressure feedback is sufficient to generate oscillations

Purely reflex-based control as opposed to centralized control has been target of different locomotion studies, in humans (Geyer and Herr, 2010), stick insects (Fischer et al., 2001) and *C. elegans* (Niebur and Erdös, 1991). In those control schemes, it has been shown that periodic movements do not necessarily need to result from neural oscillators, but can be generated as a product of reflex-based feedback loops. Therefore, we asked if we could further simplify our control model for undulatory swimming, by removing the neural oscillators and see whether pressure induced oscillations could be generated. This was done by setting the intrinsic frequency of the CPG to zero ($\omega = 0$) and exploring a model exclusively with central intersegmental coupling and sensory feedback (Figure 2.3, *Sensory-driven model* III).

Using the same local sensory feedback rules that were introduced before, we identified oscillatory patterns that emerged along the body. Moreover, we found that it was possible to generate traveling waves of body undulations in this control scheme, however exclusively when central coupling was present. Figures 2.10 and 2.11 show examples of emerged gaits for two different feedback gains. We found that this gain for the sensory driven model serves as a tuning parameter for the gait frequency and possibly the speed of swimming. Additionally different body shapes were observed depending on the feedback gain, e.g. lateral displacements were much larger for lower gains (slower speeds). Moreover, we identified characteristic patterns in activation along the body. For both gains, longer activation periods were observed rostrally, with an almost gradual increase of duration towards the tail. For lower feedback gains, also lower phase lag patterns were identified. In comparison to the previous *Combined model* and *Decoupled model*, the *Sensory-driven* model showed longer convergence times. Indications are shown in the aforementioned figures, which are plotted on a double time-scale compared to the previous emergence snapshot figures.

Figure 2.9 shows the corresponding emerged characteristics (purple) in comparison to the other models. We note that simulations were carried out including higher feedback gains than in the previous two models. The increased weight for the feedback can be seen as a compensation for the loss of the intrinsic oscillation. In contrast to the previous control schemes, primarily swimming patterns at lower frequencies were found. The frequencies could potentially be increased for other stiffness, damping and feedback gains. The number of emerged body waves in the swimming patterns correlates well with the results that were found for the previous models.

Finally, we note that the *Sensory-driven model* requires a starting stimulus in order to initiate movements, as in the straight initial position of the body no reaction forces with the environment are generated. Consequently, equal pressure on both sides of the body does not lead to any feedback that could start oscillations. In our testing setup, it was sufficient to start from randomly initialized phases, which in turn would initiate movements through the central coupling. Alternatively, one could also introduce initial force stimulation.
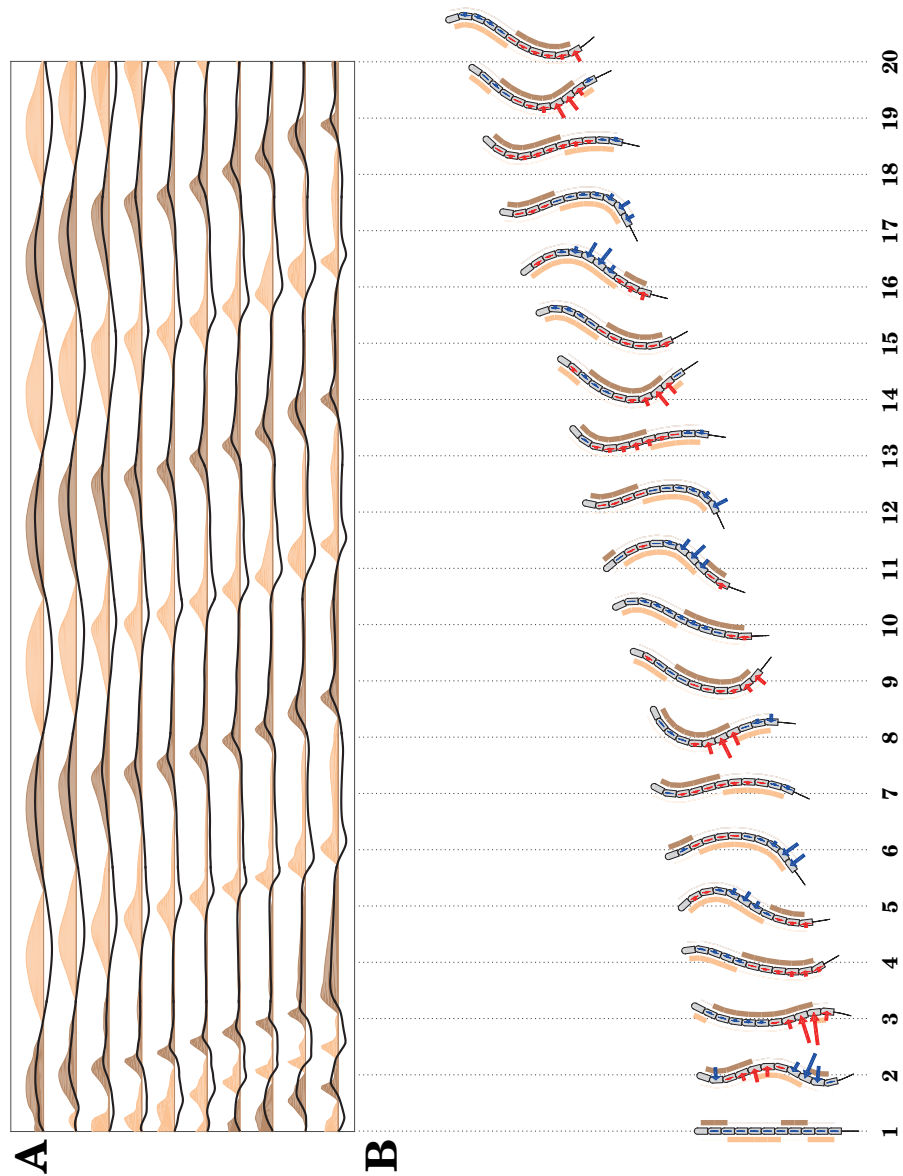
Figure 2.10 – **Emergence for the *Sensory-driven model* III with low feedback gain**. (**A**) Shows a plot of the activation dynamics over the course of 8 seconds in corresponding colors over time along with the kinematics in terms of joint angles in black lines. (**B**) 20 Snapshots over the course of the same 8 seconds show the evolution of an undulatory swimming pattern with parameters $\alpha = 1$ Nm, $\gamma = 2$ Nm/rad, $\delta = 0.1$ Nms/rad, $\Delta\Phi = 120\%$, $w_{fb} = 1$. Red ($F > 0$) and blue ($F < 0$) arrows denote external forces from the water, light orange and light brown bars along the body indicate that muscles on the respective sides are contracted.
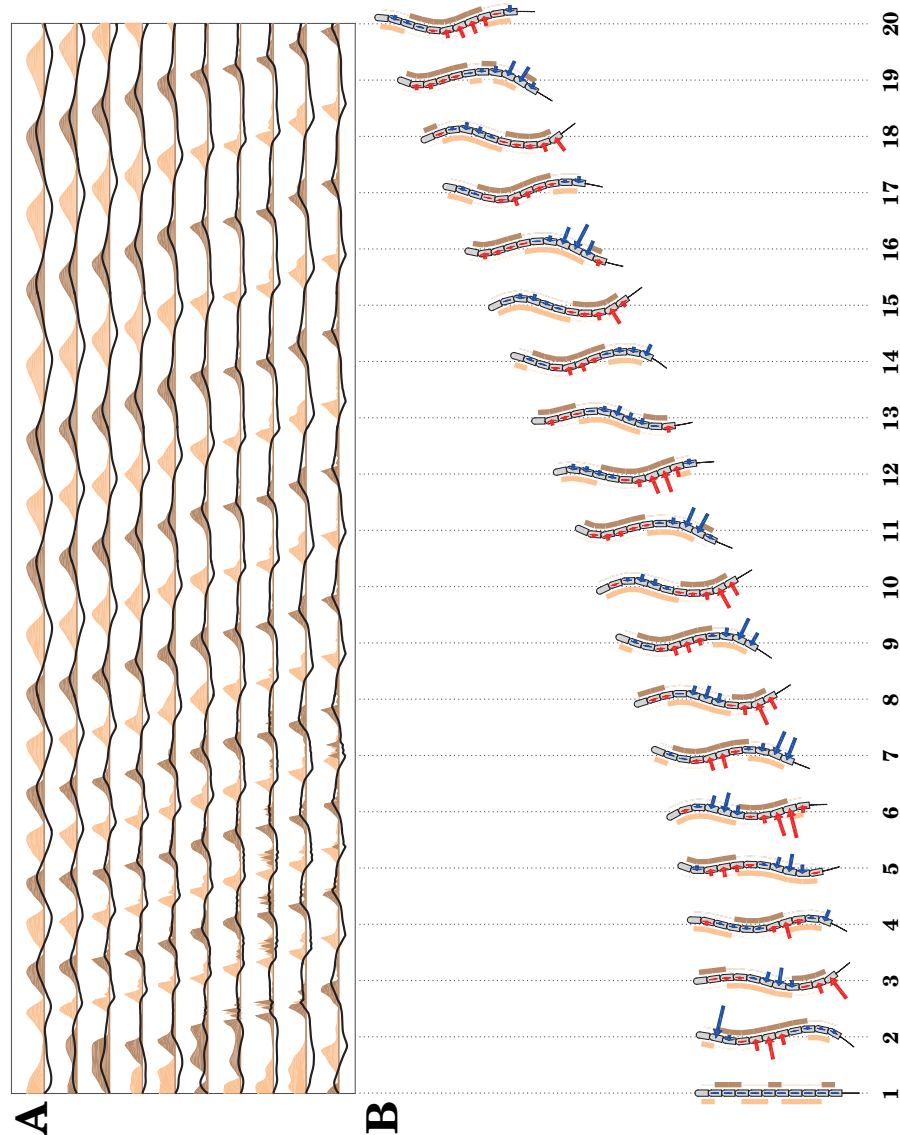
Figure 2.11 – **Emergence for the *Sensory-driven model* with high feedback gain**. (**A**) Shows a plot of the activation dynamics over the course of 8 seconds in corresponding colors over time along with the kinematics in terms of joint angles in black lines. (**B**) 20 Snapshots over the course of the same 8 seconds show the evolution of an undulatory swimming pattern with parameters $\alpha = 1$ Nm, $\gamma = 2$ Nm/rad, $\delta = 0.1$ Nms/rad, $\Delta\Phi = 100\%$, $w_{fb} = 3$. Red ($F > 0$) and blue ($F < 0$) arrows denote external forces from the water, light orange and light brown bars along the body indicate that muscles on the respective sides are contracted.

2.4.4   Energy recovery through negative work

So far, we reported our results regarding the performance of the proposed control schemes. Along with this investigations we also measured energy consumption on our simulated model and found the following:

Until now we had considered positive mechanical work of the motors as a means to compute energy expenditure and the cost of transport. However, as suggested in previous work (Wiens, 2013), a substantial amount of energy during anguilliform swimming has been identified as negative work that could be potentially recovered in a specifically engineered system (using motors as generators when braking motion is present). We therefore asked to what extent our control schemes could profit from such a system and how the overall energy expenditure changes when parts of it are recovered. The results in terms of power consumption are presented in Figure 2.12 for the 10-joint model.
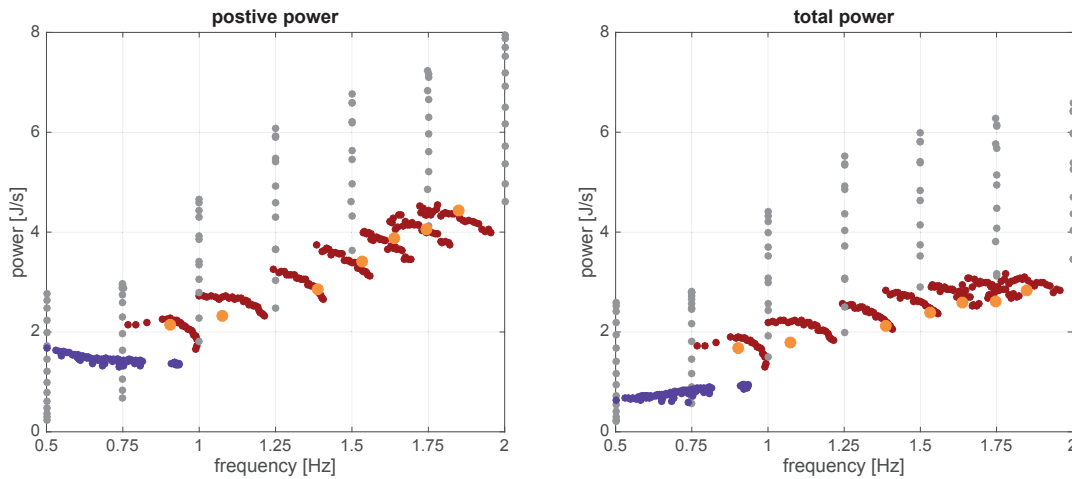
Figure 2.12 – **Energy recovery through negative work - 10 joint model**. Graphs show power depending on frequencies for high speeds (as indicated in Figure 2.9). Gray dots indicate open loop model, red dots *Combined model* (I), orange dots correspond to the *Decoupled model* (II) and purple dots show the *Sensory-driven model* (III) **(left)** Positive power computed based on positive mechanical work. **(right)** Effective power, if negative work can be fully recovered.

We found that negative work is present across all control schemes. If we consider a full recovery of the negative work (Figure 2.12, right) we found that the overall power can be decreased significantly as shown in Table 2.3. The corresponding numbers are computed as the ratio of energy from positive and negative work (details are presented in the methods, section 2.3). Higher numbers indicate therefore, more negative work that could be restored. For the *Combined model*, potential can be seen at speeds above 0.2 m/s and less at lower speeds. Also in the *Decoupled* and *Sensory-driven models*, negative work plays a big role and shows therefore that great energy recovery potential exists.

speed [m/s]	open loop	*Combined*	*Decoupled*	*Sensory-driven*
[0.0, 0.2]	0.07 ± 0.08	0.02 ± 0.02	–	0.23 ± 0.02
[0.2, 0.4]	0.26 ± 0.20	0.31 ± 0.22	–	0.24 ± 0.04
[0.4, 0.6]	0.16 ± 0.10	0.20 ± 0.04	0.23 ± 0.02	0.24 ± 0.01
[0.6, 0.8]	0.16 ± 0.07	0.27 ± 0.04	0.34 ± 0.03	–
[0.8, ∞]	0.17 ± 0.03	–	–	–

Table 2.3 – Energy recovery potential for the different swimming models - 10 joint body. Numbers represent $\frac{|E_{neg}|}{E_{pos}}$, where E_{pos} denotes the energy based on positive work, and E_{neg} indicates energy based on negative work. The quantities are presented for different speed ranges and corresponding models. Mean±std are computed among all the simulations performed for that specific speed range and model.

2.4.5 Sensitivity to muscle model gains

The muscle model is an important intersection between the neural control and the movements of the body. In this section we explored the sensitivity of the corresponding muscle parameters with respect to a few important performance metrics. Additionally, we evaluated swimming performances of the different muscle parameters α, γ, δ for different intrinsic oscillator frequencies f to see how parameters like stiffness and damping relate to different locomotion rhythms. Our goal was to get insights into the influence of the viscoelastic properties and possibly make suggestions towards advantageous parameter regimes. The results of the parameter exploration are presented in following, where we analyzed the *Decoupled*, *Combined*, and *Sensory-driven model*.

Parameters in the *Decoupled model*

Figures 2.13, 2.14 and 2.15 show variations of the four parameters α, γ, δ and f and their influence on speed, emerged phase lag, cost of transport, emerged amplitudes and emerged frequencies. The following main observations can be made:

- Low damping and intermediate or high activation gains: No stable swimming is obtained. Especially for high gains it is necessary that a certain smoothness in the movements is preserved. This can only be achieved with sufficiently high damping. Otherwise jerky movements will induce non-desirable reaction forces, and thus no stable swimming can emerge.

- Correlation between intrinsic frequency and emerging phase lag: Increasing intrinsic oscillator frequency for this model is related to increasing emerging phase lags. Except for very low swimming speeds, the phase lags are between 1 and 1.3 waves along the body.

- Correlation between amplitude and activation gain and stiffness: higher amplitudes emerge for low stiffness and higher activation gain across all frequencies and damping properties.

- Cost of transport is mainly linked to activation gain and intrinsic frequency. Higher activation gains lead to higher costs of transport, which is mainly linked to higher amplitudes. Interestingly, the cost of transport appears almost stiffness independent across different damping coefficients (except for very low intrinsic frequencies) for given activation gains. Overall we find higher cost of transport for higher intrinsic oscillator frequencies.

Parameters in the *Combined model*

For this model we looked at a case where the nominal phase lag in the central coupling between oscillators was 200 %, which the local feedback would ideally correct to a regime

for faster swimming. Results are presented in figures 2.16 and 2.17, where speed, phase lag measurements and emerged frequencies for the different parameter combinations are shown. These were the observations:

- It is necessary that the activation gain is sufficiently high in order to correct wrong phase lag patterns.

- High damping coefficients make it more difficult for the local sensory feedback to correct nominal central patterns.

- The emerged phase lags are around 1-1.3 body waves. As for the *Decoupled model,* higher intrinsic oscillator frequencies encourage slightly larger phase lags.

Parameters in the *Sensory-driven model*

Parameters in this model were explored for a central coupling with a nominal phase lag of 1 body wave for a feedback gain of $w_{fb} = 1$ and for different random initial conditions. This analysis was especially valuable to identify a parameter range of viscoelastic properties where the *Sensory-driven model* could work. Emerged speeds, phase lags as well as frequencies are presented in figures 2.18 and 2.19. We found the following main characteristics for the corresponding parameters:

- This model is much more sensitive to the choice of viscoelastic parameters than the other models, as it can be seen by the sparseness of the plot. High damping inhibits the emergence of a swimming pattern.

- Stiffness and activation gain need to be both high in order to achieve swimming.

- The overall speeds (highly correlated to the emerged frequencies) are lower and the phase lags smaller (below 1 body wave) than in the other models. As shown in figures 2.10 and 2.11 this is can be changed for higher feedback gains.

- Very similar performances are achieved for different initial conditions, which indicates a good robustness of this model, although it is missing an intrinsic oscillation mechanism.
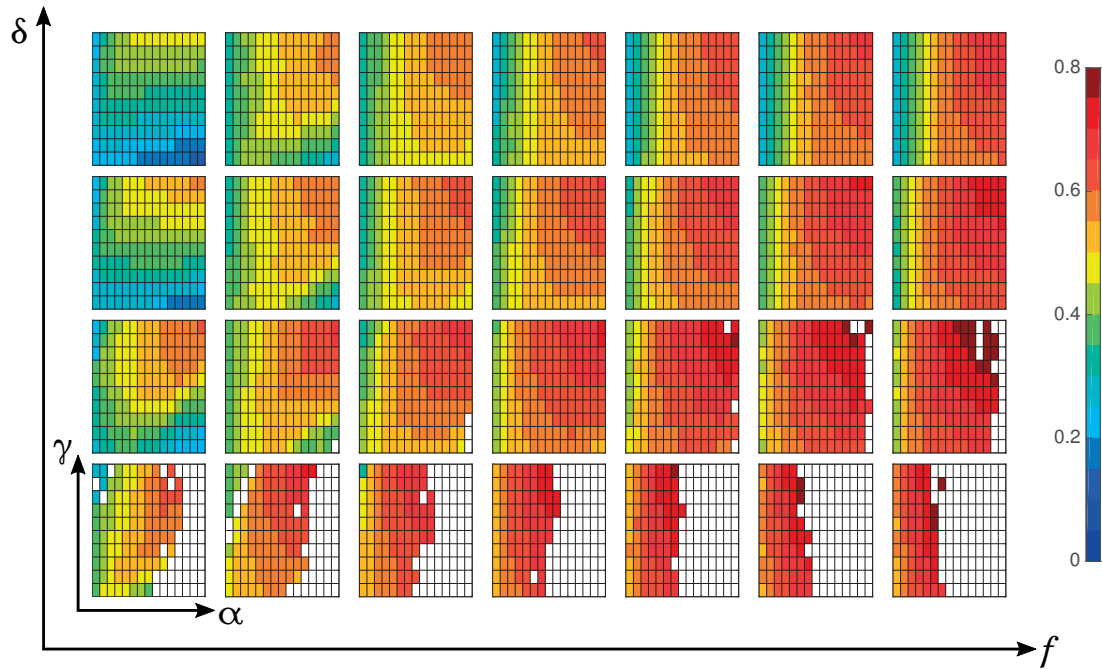
(a) Speed
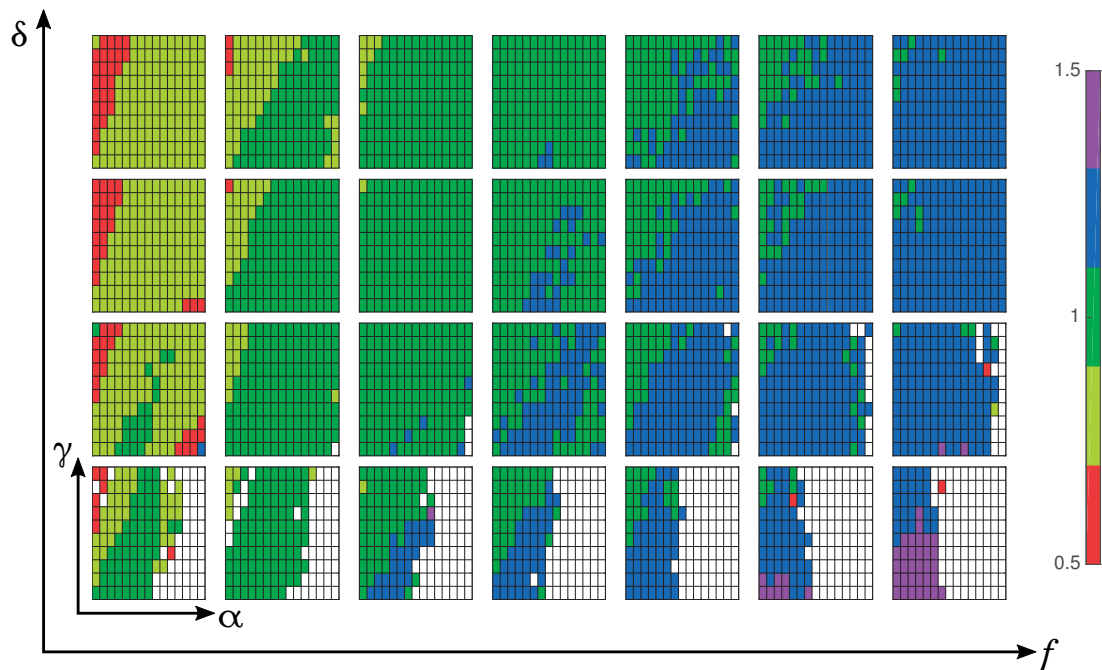
(b) Phase lag

Figure 2.13 – **Parameter exploration for the *Decoupled model*.** Uniform variation of intrinsic oscillator frequency ($f = [0.5, 2.0]$ Hz), activation gain ($\alpha = [0.5, 2.0]$ Nm), stiffness ($\gamma = [1.0, 2.0]$ Nm/rad) and damping ($\delta = [0.05, 0.2]$ Nms/rad). Feedback gain is $w_{fb} = 1$, phase lags are given in terms of number of body waves. White areas indicate non-periodic solutions.

(a) Cost of Transport

(b) Amplitude

Figure 2.14 – **Parameter exploration for the *Decoupled model*.** Uniform variation of intrinsic oscillator frequency ($f = [0.5, 2.0]$ Hz), activation gain ($\alpha = [0.5, 2.0]$ Nm), stiffness ($\gamma = [1.0, 2.0]$ Nm/rad) and damping ($\delta = [0.05, 0.2]$ Nms/rad). Feedback gain is $w_{fb} = 1$, white areas indicate non-periodic solutions. Amplitude is represented by average amplitude of the 4-th joint.

71
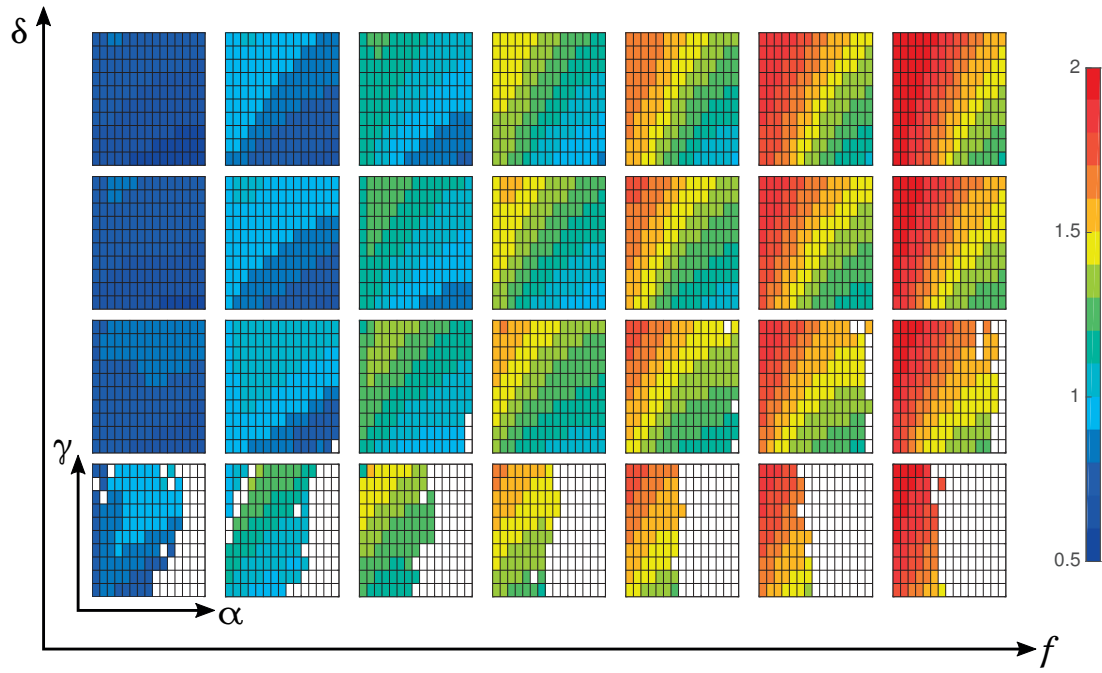
(a) Emerged frequency

Figure 2.15 – **Parameter exploration for the *Decoupled model*.** Uniform variation of intrinsic oscillator frequency ($f = [0.5, 2.0]$ Hz), activation gain ($\alpha = [0.5, 2.0]$ Nm), stiffness ($\gamma = [1.0, 2.0]$ Nm/rad) and damping ($\delta = [0.05, 0.2]$ Nms/rad). Feedback gain is $w_{fb} = 1$, white areas indicate non-periodic solutions.
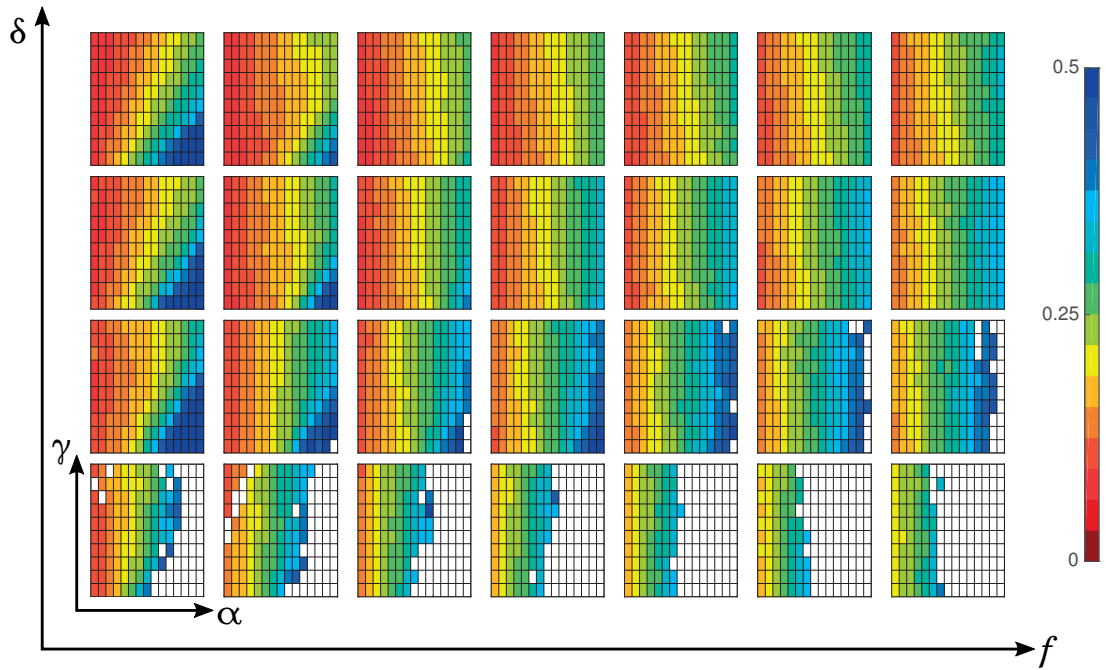
(a) Speed
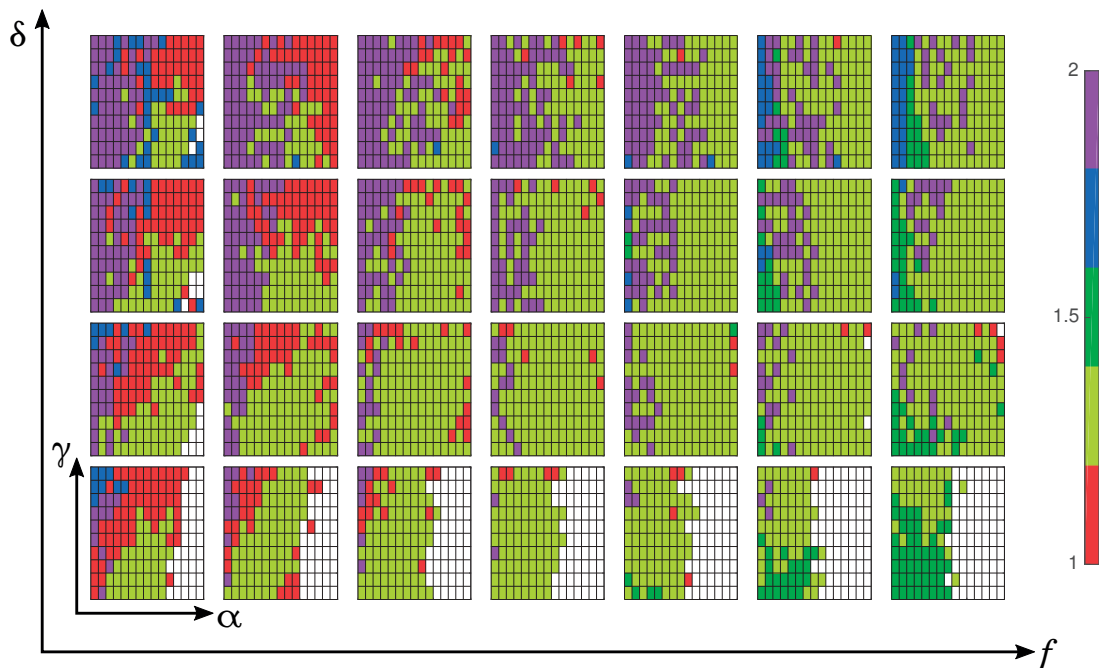
(b) Phase lag

Figure 2.16 – **Parameter exploration for the *Combined model*.** Uniform variation of intrinsic oscillator frequency ($f = [0.5, 2.0]$ Hz), activation gain ($\alpha = [0.5, 2.0]$ Nm), stiffness ($\gamma = [1.0, 2.0]$ Nm/rad) and damping ($\delta = [0.05, 0.2]$ Nms/rad). Feedback gain is $w_{fb} = 1$, phase lags are given in terms of number of body waves. Nominal phase lag is set to 200% (2 body waves). White areas indicate non-periodic solutions.
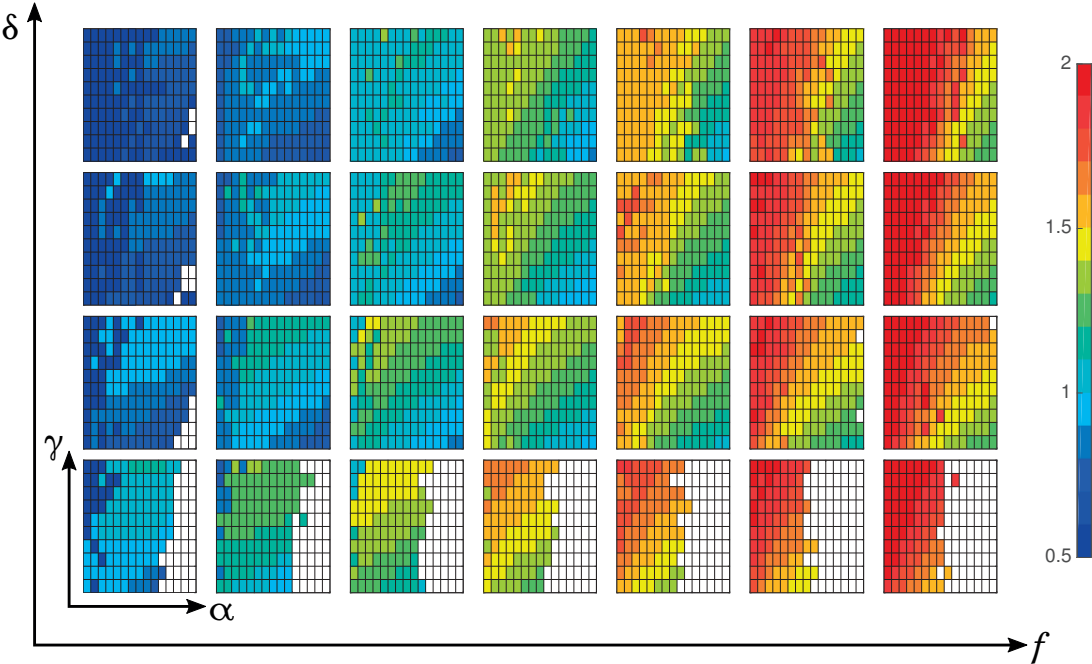
(a) Emerged frequency
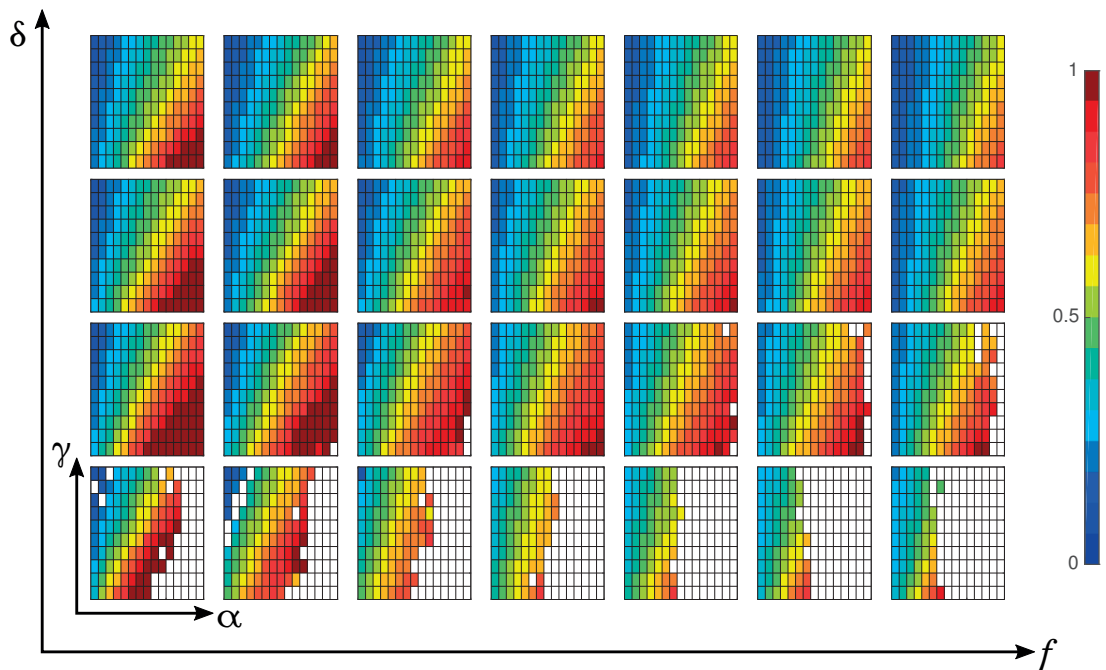
Figure 2.17 – **Parameter exploration for the *Combined model*.** Uniform variation of intrinsic oscillator frequency ($f = [0.5, 2.0]$ Hz), activation gain ($\alpha = [0.5, 2.0]$ Nm), stiffness ($\gamma = [1.0, 2.0]$ Nm/rad) and damping ($\delta = [0.05, 0.2]$ Nms/rad). Feedback gain is $w_{fb} = 1$. Nominal phase lag is set to 200% (2 body waves). White areas indicate non-periodic solutions.
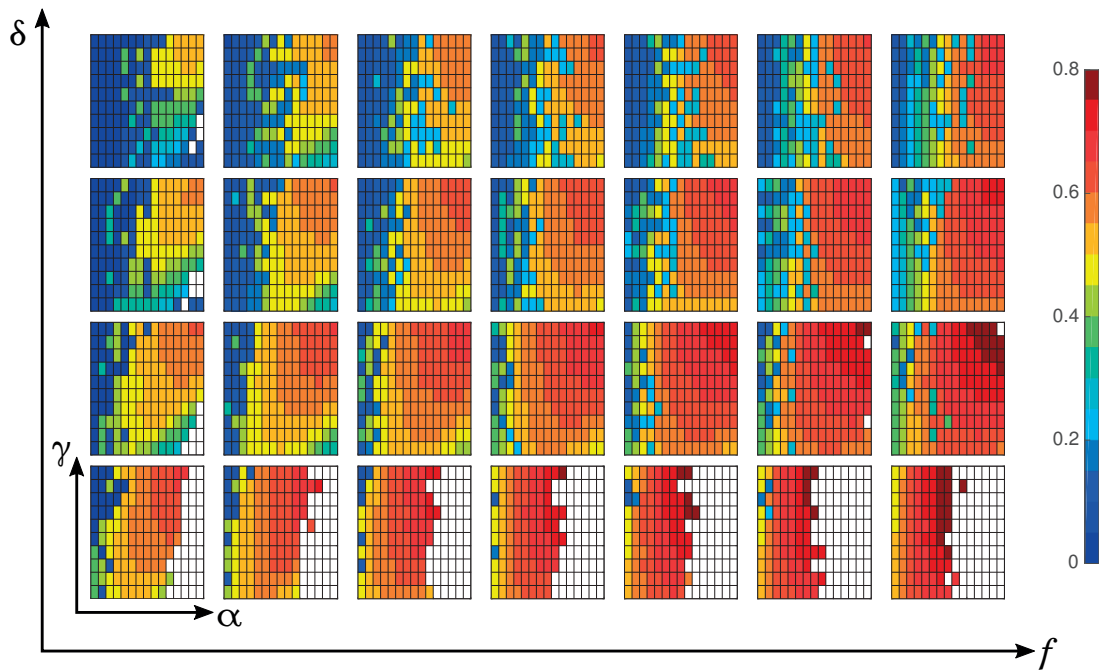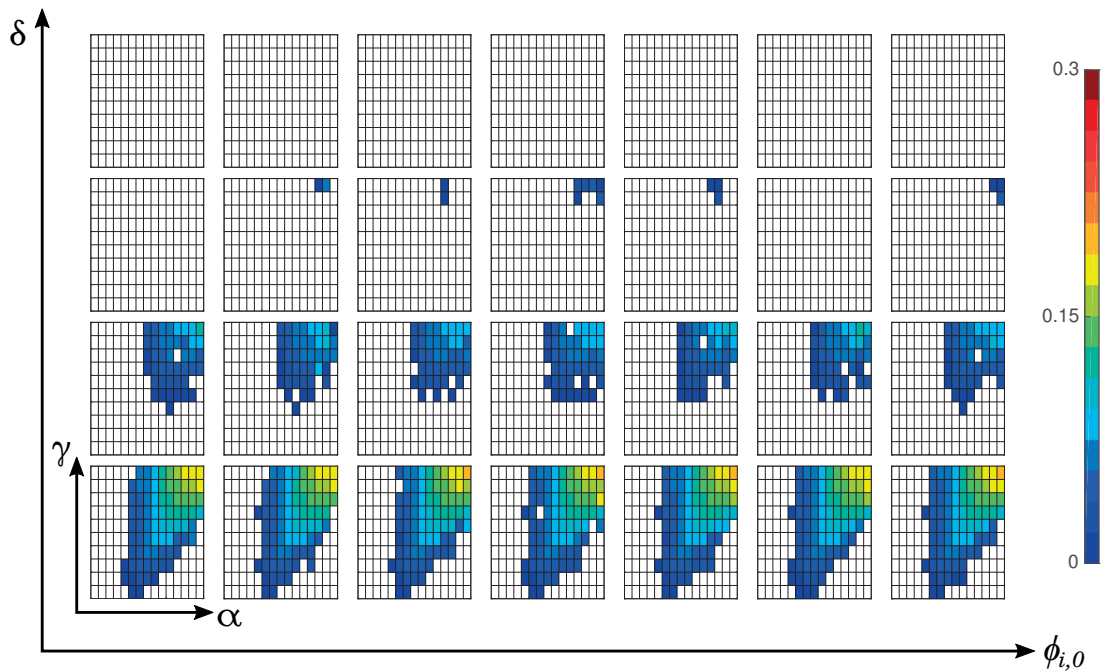
(a) Speed
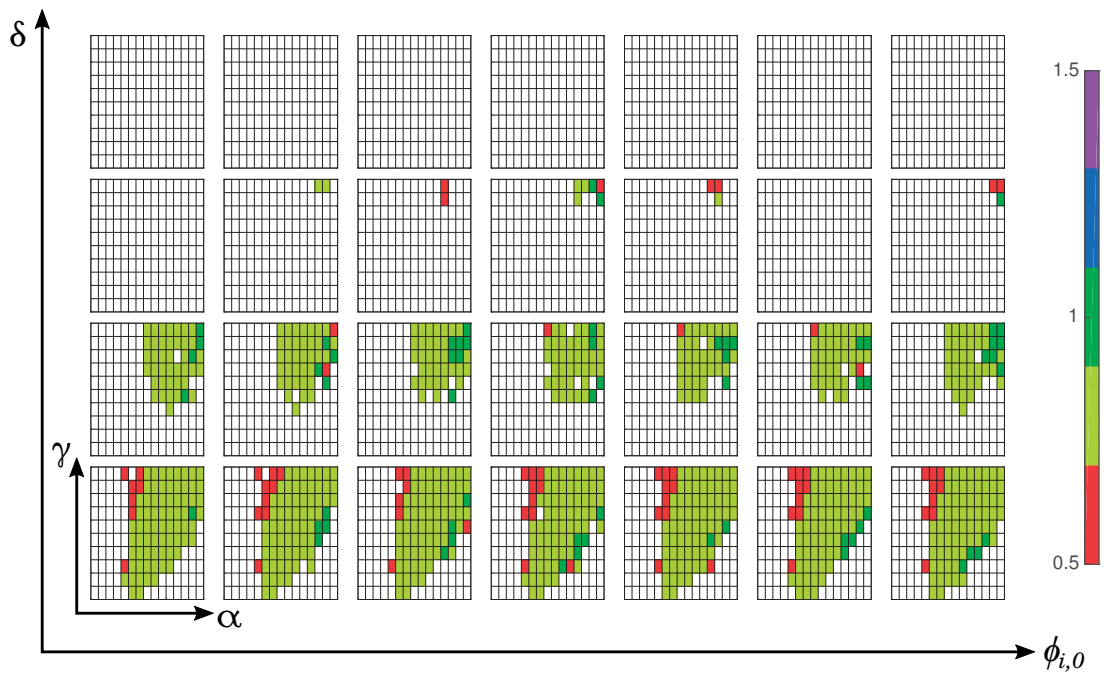
(b) Phase lag

Figure 2.18 – **Parameter exploration for the *Sensory-driven model*.** Uniform variation of activation gain ($\alpha = [0.5, 2.0]$ Nm), stiffness ($\gamma = [1.0, 2.0]$ Nm/rad) and damping ($\delta = [0.05, 0.2]$ Nms/rad) for different random phase initial conditions $\phi_{i,0}$. Phase lags are given in terms of number of body waves. Nominal phase lag in the central coupling is set to 100% (1 body wave) and the feedback gain $w_{fb} = 1$. White areas indicate non-periodic solutions.
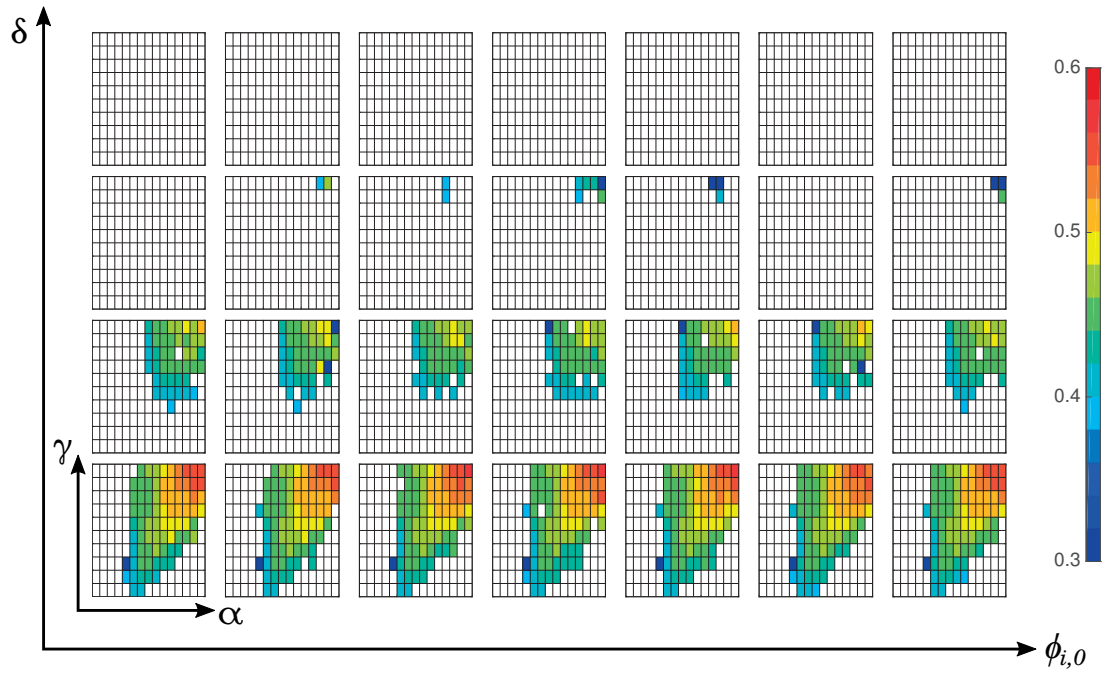
(a) Emerged frequency

Figure 2.19 – **Parameter exploration for the *Sensory-driven model*.** Uniform variation of activation gain ($\alpha = [0.5, 2.0]$ Nm), stiffness ($\gamma = [1.0, 2.0]$ Nm/rad) and damping ($\delta = [0.05, 0.2]$ Nms/rad) for different random phase initial conditions $\phi_{i,0}$. Nominal phase lag in the central coupling is set to 100% (1 body wave) and the feedback gain $w_{fb} = 1$. White areas indicate non-periodic solutions.

2.4.6 Steady-state swimming vs acceleration maneuvers

An important consideration in our proposed neuromechanical model is that the local sensory feedback mechanism aims to achieve a synchronization between muscle activation and desired reaction forces. We presented the characteristics of the force distribution in section 2.2.2. Maxima in external force magnitude are thus defined in the maximally bent regions of the body and force inflection points coincide with body inflection points. Figure 2.20 (left) shows a schematic representation. Assuming that lateral reaction forces from drag for a body segment are much higher than in axial direction, the force vectors act, as shown, orthogonally to the body (axial drag is omitted in the drawing). The resulting force for this scheme would ideally be zero since both forces in moving as well as lateral direction would cancel out, due to the symmetry in the body shape. The zero resulting force is reasonable for this theoretical system, as it would correspond to the force distribution along the body in steady-state, when the moving speed is constant.
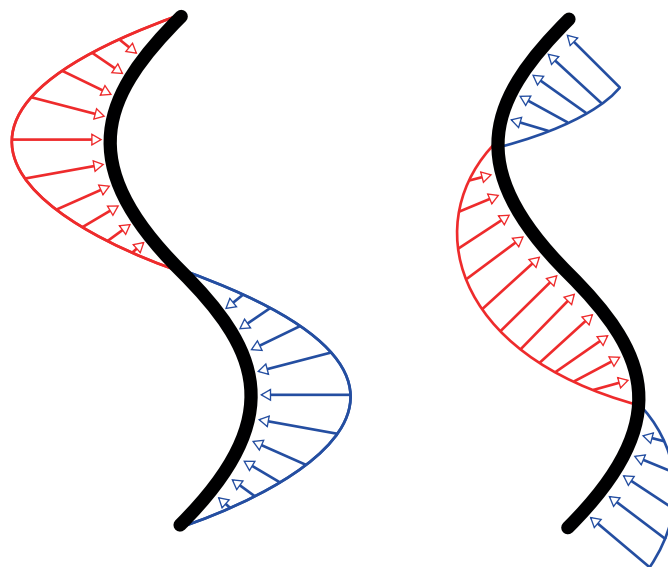
Figure 2.20 – **Conceptual steady-state vs high acceleration swimming**.

One could agree that the aforementioned force distribution is desirable in steady-state, however if acceleration (or deceleration) is required it seems not optimal. Figure 2.20 (right) shows an alternative force distribution that is governed by the same assumptions (larger drag lateral to a segment, zero axial drag). The resulting force in this scheme is non-zero and points in forward direction, lateral forces ideally cancel out again. Hence, this force distribution is more suitable for an acceleration of the body. Our feedback scheme is not limited to a particular force distribution and can also be defined for the acceleration-beneficial scheme. This would result in the following feedback:

$$\dot{\phi}_i = \quad \dots \quad - \quad \sigma_2 F_i \cdot sin(\phi_i) \quad , \tag{2.18}$$

$$= \quad \dots \quad + \quad \sigma_2 F_i \cdot cos(\phi_i + \frac{\pi}{2}) \quad . \tag{2.19}$$

Equation (2.19) indicates that this feedback rule is realized by a phase shift of $\frac{\pi}{2}$ compared to the initial rule that is desirable for steady-state. In the unit circle scheme, this shifts the attractors from $\{\frac{\pi}{2}, -\frac{\pi}{2}\}$ to $\{0, \pi\}$. Based on equation (2.19) we can now formulate the acceleration and steady-state based control methods with nearly the same feedback rule. Consequently, we can now formulate a continuous change in the force distribution between acceleration towards steady-state by changing the attractor fixed points in the feedback system.

$$\dot{\phi}_i = \quad \dots \quad + \quad \sigma_2 F_i \cdot cos(\phi_i + \kappa(v)) \quad , \tag{2.20}$$

where $\kappa(v)$ varies from $[-\frac{\pi}{2}, \frac{\pi}{2}]$ and can be linked to the speed v of the body. For small speeds, acceleration is desired, thus $\kappa \to \frac{\pi}{2}$ and for larger (steady-state) speeds, $\kappa \to 0$. κ can also be used for deceleration, where $\kappa \to -\frac{\pi}{2}$.

All our considerations in this section have assumed zero drag forces in axial direction of the segments. In reality, there is a little contribution of those forces. Fortunately, this can be easily incorporated in our analysis. Assuming small forces in axial direction, they will cancel out in the overall lateral moving direction but will form a small resulting resistance force against the moving direction. In steady-state, this resistance force has to be compensated for. Assuming that the axial drag is small, the resulting force in moving direction is also small and just enough to compensate this drag. In practice this means that the maximal reaction force peaks should lie just slightly behind the maximum bending positions. This could be achieved by an asymmetric force distribution with bigger force magnitudes behind the maximum bending positions.

2.5 Discussion

Our aim in this study was to find the essential control mechanisms that lead to efficient undulatory swimming. Efficient locomotion results from well coordinated reaction forces which in water are determined by drag, depending on the velocity of the different body segments. To exploit the aquatic environment to its fullest and generate forward propulsion, it is necessary to synchronize body movements with beneficial reaction forces. As previously hypothesized (Schwarz et al., 2011; Ristroph et al., 2015), efficient swimming could be modulated by means of pressure sensing. Based on this, we formulated a generic control scheme containing three components: oscillators for rhythm generation, central coupling and local sensory feedback. We tested the resulting neuromechanical model including viscoelastic properties and asked if and how well swimming patterns could emerge. We characterized the resulting locomotion patterns and analyzed speed and energy-related quantities to determine efficiency of the obtained patterns.

In our first model we were able to show that initially "wrong" phase patterns stemming from central coupling are corrected by local sensory feedback loops. This is consistent with previous studies (Cang and Friesen, 2000) in which fictive motor patterns in isolated spinal cord preparations showed smaller intersegmental phase lags than in intact animals. It also shows that the spinal cord can generate a variety of patterns (Delvolvé et al., 1999; Ryczko et al., 2015) and still achieve selective behaviors such as forward swimming by closing the loop with the environment.

The decoupled oscillator model is less intuitive from a biological perspective because central coupling is known to be present in the spinal cord and nerve cord of vertebrates (lamprey, Cohen et al. 1992; Matsushima and Grillner 1992) and invertebrates (leech, Cang and Friesen 2002). We found that coordinated behavior based on sensory feedback can also be achieved in a dissociated network, where all the segments are separated. In preparations where parts of the network (not all segments) were disconnected in severed nerved cords (Yu et al., 1999), it has been shown that sensory feedback could still enable a fully coordinated behavior. Moreover, our model indicates that the emergence of a traveling wave is not necessarily linked to a predefined oscillation pattern with fixed phase lags. Exploiting the natural dynamics of drag forces between the body and the water is sufficient to achieve fast and energy-efficient swimming. The findings are very interesting from a biological point of view. It seems that there are two redundant mechanisms for generating coordinated wave patterns: 1) central coupling and 2) sensory feedback. This implies a good robustness of the locomotor system, for instance, to handle lesions along the spinal cord (or nerve cord).

Also interesting for robotics, this characteristic behavior can be beneficial for modular robot design, where benefits of distributed control can be exploited. Identically programmed units can be connected together, and do not require any internal communication between them to coordinate the overall swimming behavior. This would significantly reduce computational demands as well as control complexity. Additionally, one could easily achieve fast and energy-

efficient swimming gaits in such robotic swimmers through the self-tuning property from the sensed pressure signals, independent of often unknown robot properties such as joint friction and/or damping.

The last swimming control scheme that we explored, led us to a rather unexpected finding. We showed that coordinated undulatory swimming could emerge also in the absence of intrinsic oscillators. Intersegmental coupling together with local sensory feedback loops were sufficient to induce this behavior. Therefore, as opposed to the *Decoupled model*, the feedback is useful for rhythm generation in addition to coordination. To the best of our knowledge we know only of a similar case in *C.elegans* (Niebur and Erdös, 1991; Wen et al., 2012), where a model in the absence of CPGs was proposed. Oscillations were generated due to proprioceptive sensory feedback loops. However, head or tail elements were required to oscillate in that case. In our model we noticed that besides the sensory feedback loops, the intersegmental coupling was crucial to establish a traveling wave pattern. Therefore, we hypothesize that sensory feedback in combination with body stiffness can establish oscillations, whereas additional intersegmental coupling can impose the coordination of the segmental feedback oscillators. An alternative hypothesis could be that the local feedback loops contribute also partly to the intersegmental coordination, as our feedback control scheme targets a desired reaction force distribution along the body. The resulting traveling wave could be a product of that force distribution. Nevertheless, this last model showed less robust characteristics (lower speeds and frequencies) than the other models. We also noticed that higher feedback gains were required to achieve stable locomotion patterns, suggesting also that additional "energy" or "drive" has to be put into the control system to generate oscillations.

In our study we explicitly investigated the role of pressure (or in general force) feedback to modulate CPGs or generate rhythms. It can be argued that the sense of pressure is related to proprioceptive stretch receptors as they were identified both in lampreys (Grillner et al., 1984) and leech (Cang and Friesen, 2000; Iwasaki et al., 2014). As proprioception is by definition related to the sense of the own body, also pressure or tension information could be captured by these types of sensors (possible function as tension sensors hypothesized in Cang and Friesen 2000). More precisely, one can imagine that different resulting reaction forces from the surrounding fluid will lead to different body movements, given the same level of activation in the muscles. Therefore, proprioceptive sensing such as incorporated by stretch receptors can implicitly give indirect information about the local environment.

The findings presented in this study are however subject to some limitations. Firstly, there are constraints regarding fluid dynamics. It has to be noted that our models for undulatory swimming is operating in a range with high Reynolds number ($Re = \frac{\rho v L}{\mu} = 2 \cdot 10^7$, $\rho = 1000 \frac{kg}{m^3}$, $v = 0.2 \frac{m}{s}$, $L = 1\ m$, $\mu_{water} = 10^{-5} Pa\ s$), where inertial forces are more dominant. This is very different to small animals such as the *C.elegans* swimming in more viscous fluids (e.g. methylcellulose), which swim in a regime where the Reynolds ($Re \approx 0.4$, Sznitman et al. 2010; Korta et al. 2007) numbers are very low, i.e. viscous forces are more important. It can be argued whether control strategies are the same or deviate in the different Reynolds regimes. This

should be part of future studies.

So far we tested our neuromechanical model in a simulated hydrodynamics environment (see methods section 2.3.1 for more details). It was based on the model proposed by Porez et al. 2014, which uses main ideas from the large amplitude elongated body theory developed by Lighthill. Our considerations of sensory feedback rely on the produced resulting reaction forces applied from this hydrodynamics model. Therefore, experiments and validation of the proposed models on a robot [1] in a real world hydrodynamic environment will be of great importance. Especially the role and influence of vorticity (Triantafyllou and Triantafyllou, 1995; Liao et al., 2003; Liao, 2004; Gemmell et al., 2015) will be important to analyze.

Following the validation, the next steps can involve more detailed analyses and extensions of the components. Firstly, the robustness of the different paradigms should be quantified with respect to adaptation to perturbations such as viscosity changes, variable water flow, etc. Secondly, more elaborate neuron models can be tested and possibly reveal interesting effects and implications for the neural control based on environmental sensing. Possible extensions can start with integrate-and-fire (Knuesel, 2013; Holmes et al., 2006) or leaky-integrator neuron models (Ijspeert, 2001; Billard and Ijspeert, 2000) but can also be expanded upon conductance-based Hodgkin-Huxley-like neuron networks (Ivashko et al., 2003; Bicanski et al., 2013) that incorporate detailed ionic mechanisms.

Finally, our study shows that the essential components for undulatory swimming include local oscillations and intersegmental coordination (coupling), both in agreement and exploiting the environment. This can be achieved in different ways: a) neural (*open loop*) oscillations and intersegmental coordination via sensory feedback or direct coupling b) feedback induced oscillations and central intersegmental coupling.

---

[1]initial experiments with Envirobot equipped with pressure sensors showed promising swimming behaviors for the decoupled model.

2.6 Conclusion and Future work

Our aim in this chapter was to identify the central principles of undulatory swimming gaits. Thus, rather than observing and assessing different locomotion patterns, we were interested to explain *how* movements for locomotion can be generated and which key mechanisms are necessary for undulatory swimming. Using a simple local sensory feedback mechanism we asked how internal body movements can be generated and synchronize in a way that they exploit the environment towards efficient locomotion. The main components of our model contain neural oscillators, a central coupling and a local pressure feedback mechanism. In three different control schemes we found that 1) local feedback was able to correct *wrong* phase lag patterns, 2) decoupled oscillators were able to generate a coordinated swimming behavior along the body induced by local feedback, and finally 3) the same sensory feedback loops together with central coupling were able to generate oscillatory rhythms and coordinated swimming without oscillators. A question that can be asked is how these different concepts relate to biology and how plausible they are. In table 2.4 we summarized the different properties of the models based on our obtained results and conceptual aspects. Most evident are the major drawbacks of the *Sensory-driven model* with respect to maneuvering capabilities. Although possible to generate coordinated traveling waves, control of frequency (related to speed) is hardly achievable (only through modulation of feedback gains), as this is an emergent property. Same holds for heading control. Overall, the *Combined* and *Decoupled* model have similar characteristics, albeit the former offers a more redundant system in case of failure of sensory or central mechanisms. As also highlighted by Kuo (2002), in a system with both feedforward (CPG) as well as feedback components, performance can be improved, as it provides both robustness to imperfect sensor measurements and to unexpected disturbances. From a biological point of view, we know that lampreys and leeches have these two components (oscillators and sensory feedback loops). Nevertheless, other organisms such as *C.elegans* have a very primitive nervous system were local oscillators are less likely to exist.

Property	Combined model	Decoupled model	Sensory-driven model
fast swimming	++	++	+
energy cost	++	++	++
convergence time	+	+	−
control of specific speed	+	+	−
heading control	++	+	−−
robustness to sensor noise	++	+	−
robustness to lesions	+	+	−

Table 2.4 – Conceptual evaluation of the different locomotor paradigms for undulatory swimming. (+) indicates good achievability and (−) missing property or bad performance.

In the work so far the main concepts have been introduced and their feasibility is shown, future work should further assess also the robustness of these swimming control strategies with respect to perturbations, sensor noise, maneuverability and convergence time. The study as presented here was furthermore tested in a model, where both the segmented elongated

swimming body and the hydrodynamics were numerically simulated. In a next step these findings have yet to be validated in a real physical environment. Therefore, we have started to implement our control strategies in Envirobot (Bayat et al., 2016), an anguilliform swimming robot used for pollution detection in lakes and open waters. Preliminary tests, in which the robot segments were equipped with pressure sensors on contralateral sides showed notions of coordinated swimming for the decentralized control scheme (*Decoupled model* II) and encourage further tests for validation of all the models. Furthermore, as we briefly highlighted in section 2.4.4, the idea of energy recovery is very interesting for robots like Envirobot, which would profit from long term missions that require efficient locomotion. Adaptations in the electronics, which enable short term storage of negative work could increase energy efficiency in this robot, and show the benefits of undulatory swimming platforms for real-world applications. Especially from a technological point of view for nautical applications it is crucial to design systems that efficiently convert the given energy to forward propulsion for locomotion. The most widely used classical designs are rotatory propellers in ships and underwater vehicles. However, as argued in Triantafyllou and Triantafyllou (1995) alternative propulsors than conventional propellers are required, in order to overcome the *extreme constraints on energy storage on board* of such vehicles. The presented study here, could bring us a step closer to achieve this.

3 | Bimodal Locomotion in Water and on Land

In the previous chapters we developed models that both aimed to explain movement generation as well as the emergence of optimal gait patterns depending on environmental constraints. Mostly numerical simulations were used to approximate the reaction forces between the locomotor body and the environment. Given the possiblity to explore extensive solution spaces for gaits and relevant parameters, the use of those simulations is greatly justified. Nevertheless, in order to strengthen the effectiveness of such derived findings, real world experiments should be encouraged for validation.

Therefore, we asked in this chapter how we can investigate locomotion with more elaborate physical models (namely robots). In this process we focused on important aspects of how reaction forces are generated between body and environment. Our study was set in a challenging bimodal condition, with both terrestrial as well as aquatic properties, where we investigated salamander locomotion by means of walking and swimming.

*The subsequent sections are based on our published article "K. Karakasiliotis, **R. Thandiackal**, K. Melo, T. Horvat, N. K. Mahabadi, S. Tsitkov, J. M. Cabelguen, A. J. Ijspeert. From cineradiography to biorobots: an approach for designing robots to emulate and study animal locomotion. Journal of The Royal Society Interface (2016)", in which I contributed as a main co-author.*

My original contributions

- Major contribution to the written manuscript
- Analysis of cineradiographic recordings and transfer of movements to the robot
- Programming and control of the robot
- Design and evaluation of robot experiments
- Waterproofing of the robot
- Minor contributions to the robot design with CAD

3.1 Abstract

Robots are increasingly used as scientific tools to investigate animal locomotion. However, designing a robot that properly emulates the kinematic and dynamic properties of an animal is difficult because of the complexity of musculoskeletal systems and the limitations of current robotics technology. Here we propose a design process that combines high-speed cineradiography, optimization, dynamic scaling, 3D printing, high-end servomotors, and a tailored dry-suit to construct Pleurobot: a salamander-like robot that closely mimics its biological counterpart, *Pleurodeles waltl*. Our previous robots helped us test and confirm hypotheses on the interaction between the locomotor neuronal networks of the limbs and the spine to generate basic swimming and walking gaits. With Pleurobot, we demonstrate a design process that will enable studies of richer motor skills in salamanders. In particular, we are interested in how these richer motor skills can be obtained by extending our spinal cord models with the addition of more descending pathways and more detailed limb central pattern generators (CPG) networks. Pleurobot is a dynamically-scaled amphibious salamander robot with a large number of actuated degrees of freedom (27 in total). Because of our design process, the robot can capture most of the animal's degrees of freedom and range of motion, especially at the limbs. We demonstrate the robot's abilities by imposing raw kinematic data, extracted from X-ray videos, to the robot's joints for basic locomotor behaviors in water and on land. The robot closely matches the behavior of the animal in terms of relative forward speeds and lateral displacements. Ground reaction forces during walking also resemble those of the animal. Based on our results we anticipate that future studies on richer motor skills in salamanders will highly benefit from Pleurobot's design.

3.2 Introduction

Agile locomotion in animals results from a complex interplay of various components, involving: the central nervous system, the peripheral nervous system, the musculoskeletal system, and interactions with the environment (Dickinson et al., 2000). This makes decoding the mechanisms of locomotor control a difficult problem. Researchers have been trying to determine the role of each component with different approaches: (i) locomotion studies involving kinematic and dynamic recordings (Daley and Biewener, 2006), (ii) electromyographic studies (Engberg and Lundberg, 1969), (iii) neurophysiological studies in vitro and in vivo (Grillner et al., 1995), (iv) electrical stimulation studies (Cabelguen et al., 2003), and more. In addition to animal experiments, computational and robotic studies can be very useful in investigating interactions between the different components (Holmes et al., 2006; Floreano et al., 2014; Ijspeert, 2014). *"Robots have multiple properties to complement animal studies: Their actions are repeatable, they offer access to variables or quantities that would be difficult to measure on animals, they can perform movements that are unnatural or dangerous for animals, and their morphology can be systematically changed."* (Ijspeert, 2014). Used as physical models of animals, robots are interesting as complements to neuromechanical simulations because they provide real physics. This is particularly important for locomotion that relies on complex interactions with the environment, such as swimming, crawling on mud, etc., since the motions involved are very difficult to simulate properly. Biorobots are therefore increasingly used as tools in locomotion studies to test hypotheses about biomechanics and neural control (see Ijspeert 2014 for a review). There are several examples of studies(Dickinson et al., 1999; Ijspeert et al., 2007; Maladen et al., 2009; Marvi et al., 2014; Libby et al., 2012) in which robots have been instrumental in understanding some properties of animal locomotion.

Two approaches can be distinguished among computational and physical models: template and anchor models (Full and Koditschek, 1999). *"A template is the simplest model (least number of variables and parameters) that exhibits a targeted behavior."* An anchor is *"a more realistic model fixed firmly or grounded in the morphology and physiology of an animal."* Templates are useful for studying general principles of locomotion. The same template model can represent several types of animals, such as the spring-loaded inverted pendulum (SLIP) model for legged running (Blickhan and Full, 1993). Physical models (i.e. robots) have been designed based on template models, for instance the biped ATRIAS robot (Grimes and Hurst, 2012), the hexapod RHex robot (Saranli et al., 2001), and the salamander-like Salamandra robotica (Ijspeert et al., 2007). These robots were designed to use the lowest number of degrees of freedom to obtain and study a particular type of locomotion. Depending on the specific targeted behavior, template models can be made as complex as necessary (but not more). Anchor models can then be used to validate the templates and to analyze multi-leg coordination, joint torques and neuromechanical aspects.

Salamanders have attracted the attention from researchers from various fields. In particular, they have garnered the interest of neuroscientists for investigating the neural mechanisms that produce their various aquatic and terrestrial locomotor modes as well as the cellular

and molecular mechanisms underlying their impressive regenerative abilities (Chevallier et al., 2008; Ryczko et al., 2010; Kragl et al., 2009; Kumar and Simon, 2015). Moreover, since salamanders resemble the early tetrapods in their skeletal morphology and locomotor modes more than any other extant species (Schaeffer, 1941; Carroll, 1988; Worthington and Wake, 1972; Romer and Byrne, 1931; Howell, 1944; Barclay, 1946; Gray, 1968; Edwards, 1989; Gao and Shubin, 2001; Clack, 2002a; Petti et al., 2014) they can be used as experimental models to have some insights into the neural mechanisms underlying aquatic-to-terrestrial transition in primitive tetrapods (Ijspeert et al., 2007). We are currently investigating the interplay between central pattern generation, sensory feedback and descending modulation for producing the large variety of motor behaviors involving whole body movements as exhibited by salamanders. In previous work (Ijspeert et al., 2007), we designed a simple template robot model of the salamander with a CPG model that could generate two motor behaviors of the salamander (swimming and walking trot) and that included two descending pathways (left-right stimulation). But the salamander is capable of producing a larger variety of motor behaviors and is known to have more descending pathways. This motivated the design of an anchor model of the salamander. So far we have mainly explored two descending pathways (left-right stimulation) but more pathways exist in the salamander. In the neural models, additional descending pathways can be added to stimulate subparts of the complete locomotor circuit (e.g. only the tail, only the hind left limb) similar to the action of strings in a marionette. The way in which specific behaviors are generated, when only the marionette is visible but not its strings, can be inferred from a model. The better the model captures the DoF of the marionette the closer one can estimate the number of strings needed for the model to reproduce the observed behaviors. In the same way, if the behavior of the marionette depends on external interactions one has to be able to simulate those interactions with the model. Capturing those interactions accurately, especially when they cannot be properly simulated, is important and, for that reason, a physical model – in our case a salamander-like robot – is necessary. It is important to try to include all the components that influence locomotion: the spinal cord circuits, the sensory feedback, the descending modulation, the internal body dynamics (i.e. muscle dynamics, the musculoskeletal dynamics), and the external body-environment dynamics. Locomotion will likely never be completely understood without investigating the interaction of all these components (i.e. while necessary, it is not sufficient to investigate these components in isolation). At the same time, we realize that any of these components will only be approximations, and future work will involve investigating the effect of these approximations, for instance by comparing the results of experiments carried out with components implemented at different levels of abstraction, e.g. coupled oscillator models versus spiking neural network models for the spinal circuits (Knüsel et al., 2013), and different types of muscle models.

Our previous robots Salamandra robotica I and II were designed to investigate the transition between swimming and walking (Ijspeert et al., 2007; Crespi et al., 2013). Those robots have 10 and 12 actuated degrees of freedom (DOFs), respectively, and use simple 1 DOF rotational limbs like the RHex robot (Saranli et al., 2001) for ground locomotion. They can be seen as

template models with just the minimal number of DOFs to investigate inter-limb and body-limb coordination in steady state swimming and walking gaits. However, the limited number of DOFs not only restricts our ability to study the organization of the limb CPG networks, but prevents the study of richer motor skills (e.g. aquatic stepping gaits, turning, paddling etc.) where multiple DOFs are used (Ashley-Ross, 1994; Karakasiliotis et al., 2012). For example, we showed in previous work (Crespi et al., 2013; Karakasiliotis and Ijspeert, 2009) that a single rotational DoF at each limb is a limiting factor for understanding turning in salamanders and discussed the importance of a knee joint. It is also easy to show that for aquatic stepping and paddling single-DoF limbs cannot capture the necessary interactions with the environment (e.g. regulating the distance between the feet and the girdles so that traction with the ground is maintained, or orienting the limb in such way that the hydrodynamics are similar to the ones that the animal experiences).

Building an anchor robot involves multiple design challenges: (i) designing the proper kinematic structure, i.e., the topology and number of DOFs, capable of emulating the desired animal behaviors, (ii) matching similar dimensions and mass distributions, and (iii) replicating muscle-like properties and more generally viscoelastic properties of the body. But even in anchor models many trade-offs and simplifications need to be made. The constraints relate to technological limitations in actuation (size, weight, torque, power density and velocity limits) and sensing (size and accuracy), price and manufacturability which highly affect the accessibility of the platform to various researchers as well as studies of morphological variability. Variations of the optimized platform – possibly, but not necessarily, drawn from the variability found in salamanders and other sprawling animals – will give hints on the role of body-morphology with respect to the organization of the locomotor network and the pathways that regulate it.

Here we present an approach to designing a biorobot as an anchor model and use it to create Pleurobot, an amphibious salamander-like robot that emulates *Pleurodeles waltl* (*P. waltl*). Key elements of Pleurobot's design are the number and placement of locomotion-relevant joints. Our approach is then composed of the following steps: (i) collecting three-dimensional kinematics of skeletal elements using biplanar high speed cineradiography; (ii) optimization of the robot kinematic structure using a genetic algorithm to be able to replay the set of collected gaits; (iii) dynamic scaling, i.e. performing an analysis of the animal and robot dynamics to ensure that the animal and robot gaits are carried out within the same regimes of interaction forces with the environment; (iv) constructing the robot using 3D printed parts, high-end servomotors, and a tailored dry-suit; and (v) comparing the robot and animal gaits with motion capture and force plate measurements. The main features compared to previous design methods are the combination of cineradiography and optimization to identify important locomotion-relevant degrees of freedom for making the robot structure which can easily change depending on the hypothesis being tested. Cineradiography, in our case bi-planar, is increasingly used to characterize animal locomotion (Fischer and Lehmann, 1998; Brainerd et al., 2010). In biorobotics, it has been used to compare animal and robot locomotion, e.g. during sand swimming (Maladen et al., 2009), or to extract design principles

for template-like robots (Andrada et al., 2013) or robot simulations (El Daou et al., 2010), but to the best of our knowledge it has not yet been used together with optimization algorithms to design a physical anchor-like robot model. An important feature that makes *P. waltl* a excellent animal to model is its low dynamic behaviors, especially during ground locomotion. Many of the skills which can enrich our understanding of the salamander's locomotor network are much less dynamic than other animals, like mammals for instance. Our methodology is based on this fact. Not only current technology reaching its limits in producing reliable dynamic platforms, but also muscle, tendon and bone-properties become much more important during dynamic locomotion.

3.3 Pleurobot's design methodology and development

Our robot is based on *P. waltl*, a salamander that exhibits both terrestrial and aquatic loco-motion. This salamander represents a good candidate for our design approach, having been subject to neurophysiological (Ryczko et al., 2010; Delvolvé et al., 1999), electromyographic (Delvolvé et al., 1997) and biomechanical (Ijspeert et al., 2007; Karakasiliotis et al., 2012) studies in the past. Its morphology is composed of an elongated body (trunk and tail) and four limbs located at the pectoral and pelvic girdles (Fig. 3.1). The average body length and weight of *P. waltl* specimens ($n = 2$, 8.45 ± 0.078 cm snout-vent length) considered for this study were approximately 17.6 cm and 23.8 g. Biplanar high-speed cineradiographic (Neurostar® Siemens AG) recordings at 500 fps and image resolution of 1536x1024 were performed at the University of Jena, Germany. The data presented here has been partially published else-where (Karakasiliotis et al., 2012) and in detail in a doctoral thesis (Karakasiliotis, 2013). More specifically, walking gaits have been described in (Karakasiliotis et al., 2012), whereas data for aquatic stepping and swimming are original. A comparison between animal and robot sizes is provided in Table 3.1.

Characteristic length	*P. waltl*	Pleurobot
Snout-vent length [m]	0.085	0.73
Body length [m]	0.176	1.52
Mass [kg]	0.024	7.40
Scaling factor [-]	1	8.6

Table 3.1 – Comparison of animal and robot dimensions

As discussed in the introduction, several constraints guide the design of an anchor robot. Some are related to technology and some are driven by the designer's goals. For Pleurobot, we consider one of the most important constraints to be the ability to easily produce copies and variations of the robot at a reasonable price and time, while still being able to test hypotheses on rich motor skills. Most of the rich behaviors of the salamander depend on its segmented limbs (turning, paddling and more), so particular focus was given in replicating the DOFs of the limbs. An important technological constraint is actuation. Currently the most accessi-ble, efficient and cost effective actuator is the DC motor. However, DC motors still remain
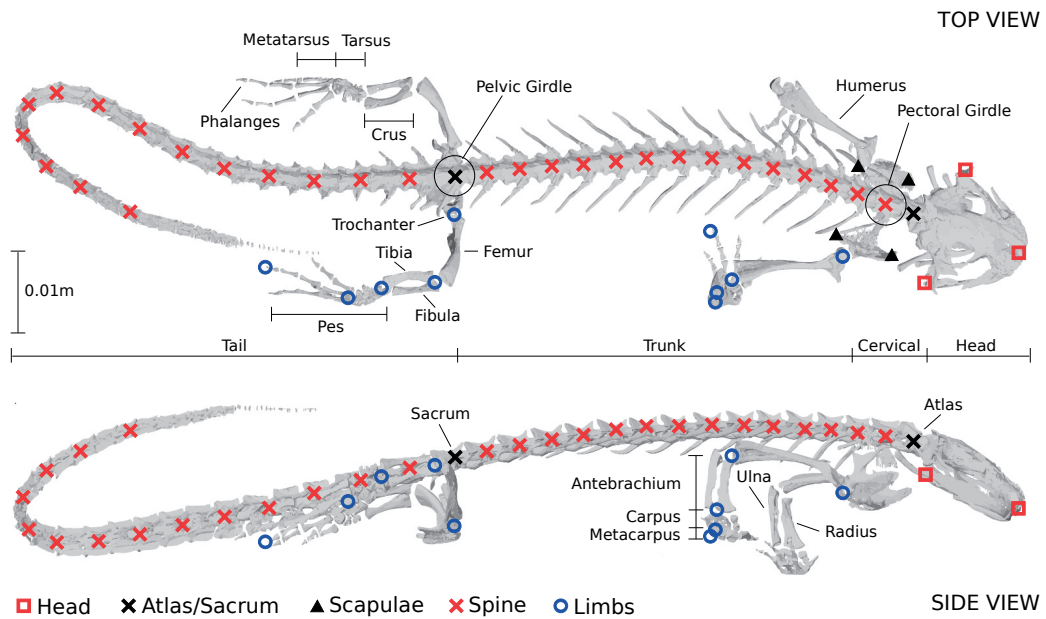
Figure 3.1 – **P. waltl skeletal system**. The basis of the design methodology is built from a careful analysis of cineradiographic recordings, the subsequent tracking of the bone structure and the 3D reconstruction. Top and side view of a CT-scan are shown, where the markers indicate tracked points: 3 points for the head, 4 points for the scapulae, 5 points for each limb, 16 points in the trunk and 20 points in the tail were included in the analysis. The Sacrum was used to separate between trunk and tail.

inefficient in very small scales and we had to choose larger DC motors than we would have liked. Therefore, the motors' size guides the robot's final size, which is larger than the animal (Table 3.1). Given these constraints, the key element of Pleurobot's design is to determine two important engineering considerations: (i) the number of locomotion-relevant joints and (ii) the placement of each joint along the robot's body.

Therefore, we developed a dataset of sequential whole-body postures for walking, swimming and aquatic stepping using the cineradiographic recordings and the 3D reconstruction of kinematics obtained from experiments with *P. waltl*. In order to derive the 3D reconstruction from the cineradiographic recordings, the salamander skeleton was manually tracked in all the videos where the animals showed straight and steady state locomotion. For this purpose a custom software based on OpenCV (open graphics C/C++ library) was developed and used. The top and side views were digitized at a frame rate of 40 Hz for swimming and 80 Hz for walking. The dataset of body postures was then used to guide an optimization problem with two goals: (i) optimal segmentation of the robot, i.e., minimum number of joints and (ii) their optimal placement so that the segmented body can reproduce recorded animal postures in our dataset. The spine, forelimbs, and hind limbs were optimized as three separate kinematic chains.
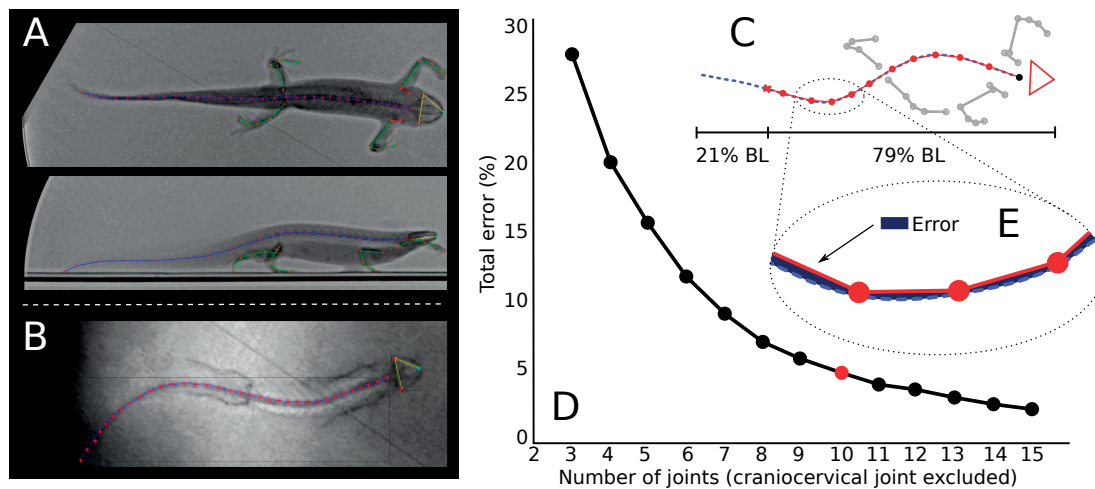
Figure 3.2 – **Spine optimization based on cineradiographic data**. We used the cineradiographic recordings of *P. waltl* and the resulting 3D kinematics of the skeletal structure to design the robot's spine: (A) Top and side view snapshots for walking and (B) top view for swimming. The markers indicate which points were tracked. Assuming mostly constant bending in the sagittal plane, the spinal movements in the transverse plane were approximated by a segmented spine (C) (BL: Body length). The segmentation was derived via an optimization procedure (D), in which separate optimizations for various numbers of joints were carried out. For each joint configuration the segment lengths were derived via an optimization using a GA (Genetic algorithm). The error area (E) between observed spinal bending in *P. waltl* and the segmented line was used as a fitness function. A resulting number of 10 joints (red data points) was chosen as a trade-off between accuracy of the approximation and a minimal number of joints.

3.3.1 Spine

The cineradiographic data for the axial movements of the salamander show that during steady state locomotion (both in walking and swimming gaits), salamanders undulate mainly in the transverse (horizontal) plane; bending in the sagittal (vertical) plane was almost constant (Karakasiliotis et al., 2012), (Karakasiliotis, 2013) . This reduced the problem of designing the robot spine to its optimal segmentation in the transverse plane.

Each snapshot of the salamander spine was represented as a continuous curve in the transverse plane (Fig 3.2A, 3.2B). The mean length of all the curves in the dataset was used to define the length of the segmented line that represents the spine of the robot (including head). Note that the length we refer to here represents part of the animal's spine, in particular 79% of the body length. The remaining 21% (end of the tail) presented rather irregular kinematics between cycles, suggesting that mostly passive dynamics shape the end of the tail during walking or swimming (Fig. 3.2C).

We performed several optimization runs with different predefined numbers of joints using a
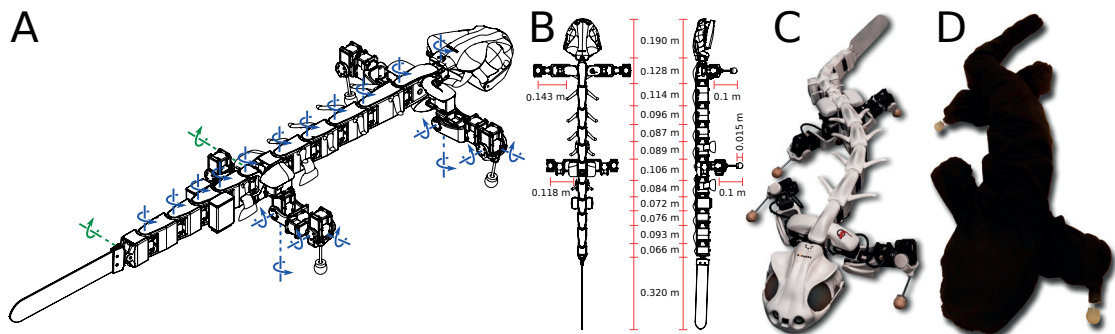
Figure 3.3 – **Pleurobot**. Following our design methodology, Pleurobot with a total of 29 DOFs (degrees of freedom) was derived. In (A) blue axes indicate the 27 motorized DOFs, whereas the green axes indicate 2 passive DOFs (i.e. unactuated free joints). The results from the spine optimization together with segmented limbs (B), allow replicating various gaits, such as walking, swimming and aquatic stepping. The robot design (C) comprises 3D printed parts (white), 27 off-the-shelf servomotors (black), silicon feet and a flexible tail. (D) A waterproof swimming suit out of a Lycra®Nylon fabric laminated with a 1mm layer of polyurethane completes the design that allows locomotion in terrestrial as well as aquatic environments.

genetic algorithm[1] (GA). Having the craniocervical joint (i.e. neck joint) fixed, the position of each of the other joints was open for optimization. Arbitrarily, 3 to 15 joints were used in different optimization runs (Fig. 3.2D). The GA generated new positions for the corresponding number of joints at each iteration. To evaluate how well the given joints and their positions could reproduce the curvature of the salamander's spine, we introduced an error metric as the sum of squared areas between the segmented line and each curve found in the dataset of animal postures (Fig. 3.2E). This was done for 80 trials, which corresponds to a total of 2798 analyzed postures both in water and on ground. For each specific number of joints, the optimal positions were assumed when the fitness function converged to a very small value (10^{-6}). For the GA in our spine optimization of the robot we used the GA implementation from Matlab (Matlab 2014b) with default parameters. As such we used the following parameters: a population size of 200, a crossover fraction of 0.8 and a migration fraction (guarantees survival from one to next generation) of 0.05.

As expected, the higher the number of joints the better the segmented line can capture the shapes of the animal's spine during locomotion (Fig. 3.2D). The approximately exponential convergence of the total error value allowed us to arbitrarily select a number of 10 joints which we considered as a good trade-off based not only on the geometry but also the resulting length of the robot. Including the craniocervical joint, that makes a total of 11 spine joints (Fig. 3.3A). This number and their corresponding optimal positions allow Pleurobot to imitate the bending of the salamander's spine in different gaits to a good extent as illustrated in the accompanying videos and discussed below. Notice in Fig. 3.3B and Table 3.2 how the optimization found that

---

[1]A type of evolutionary optimization algorithm that evolves a population of candidate solutions by altering and mutating them with the goal to maximize a selected fitness criterion.

a higher curvature is needed around the hind but not around the front girdle. This is a result of both the limited bending of the front part of the body for all gaits (Karakasiliotis et al., 2012) and the increasing curvature of the spine towards the tail during swimming. Two passive DOFs (green in Fig. 3.3A) were placed at the first and the last segment of the tail to account for the passive bending of the salamander's tail in the sagittal (vertical) plane. It is important to note here that this partially optimal segmentation, guided by a subset of the behaviors observed in salamanders, might prove less optimal for behaviors for which data is not yet available and were not used in the optimization. However, we strongly believe that except for turning gaits, most other behaviors are based on either walking or swimming patterns or a mix of the two (e.g. underwater stepping ro paddling). Future experiments will show whether Pleurobot's 'optimal' design captures poorly turning gaits, in which case the ease of producing variations in the robot design will prove significant.

Segment	Length [m]
Head	0.190
Joint 1 – Joint 2	0.128
Joint 2 – Joint 3	0.114
Joint 3 – Joint 4	0.096
Joint 4 – joint 5	0.087
Joint 5 – joint 6	0.089
Joint 6 – joint 7	0.106
Joint 7 – joint 8	0.084
Joint 8 – joint 9	0.072
Joint 9 – joint 10	0.076
Joint 10 – joint 11	0.093
Joint 11 - Tail	0.066
Tail fin	0.320
Forelimb upper leg	0.143
Forelimb lower leg	0.100
Hind limb upper leg	0.118
Hind limb lower leg	0.100
Ball foot radius	0.015

Table 3.2 – Pleurobot segment dimensions

3.3.2 Limbs

The hind limb of the salamander consists of two main segments (Fig. 3.1), the thigh and the crus. In Karakasiliotis et al. 2012 we described those two segments as a four DOF manipulator with three DOFs at the hip joint and one at the knee. The analysis of the kinematics suggested that all four DOFs are used during locomotion and they were therefore all included in Pleurobot. Adjoining the two main segments is the foot, which has a highly complex structure with compliant elements as well as bones. While in our future work we plan to use Pleurobot to

demonstrate the principles of sprawling locomotion with biomimetic feet, we consider feet here as simple point-contact elements. We discuss the effects of simplifying the foot structure in the experimental validation of Pleurobot (section 3.5). In all walking trials salamanders clearly showed foot ground contact at the metatarsals, i.e., at the distal region of the foot. For that reason, Pleurobot's ball-foot element was placed at the mean distance of the metatarsus to the animal's knee during locomotion.

Consequently, the robot's limbs consist of a two-link system with the hip approximated by 3 consecutive DOFs and a 1-axis knee joint. Pleurobot's forelimbs and hind limbs follow the same design methodology while their corresponding element sizes were measured and scaled up from the animal's CT-scan. Excluding the feet and some possible structural elasticities in the animal's joints, it is reasonable to say that Pleurobot's limbs are a closely scaled up replica of the animal's limbs.

3.3.3 Hardware implementation

For the actuation, we chose Dynamixel MX-64R servomotors from ROBOTIS, Inc. as they offer a good trade-off featuring a fairly high torque-mass ratio (7.3 Nm of stall torque at 126 g), max no-load speed of 78 rpm, and positional accuracy (0.088° resolution) at a reasonable price. The locomotion controller for replicating the animal gaits is implemented on an Intel Atom 1.6 GHz-based computer provided by ROBOTIS (DW-EK01) placed inside the robot head. The same hardware kit handles the low level communication with the servomotors through an RS-485 bus at 1 Mbps. We were able to send position commands to the servomotors at a rate of 1 kHz. The entire mechanical structure of Pleurobot is 3D printed (Laser sintering) using three variations of polyamide 12 (plastic): the skull (head) is made out of natural polyamide, the spinal segments are made out of glass filled polyamide and the limb segments out of aluminum filled polyamide. The two main meta-materials were used because of their increased strength compared to natural polyamide, and also because of the higher density than water, which is important in order for the robot to be able to be sufficiently submerged in water. The ball-shaped feet are made out of silicone rubber molded around a 3D printed spherical structure attached to steel rods which act as the lower leg of each limb. The robot dimensions and specifications are summarized in Table 3.2 and Table S1.

In the swimming experiments, the robot, including the passive tail fin, was entirely covered by means of two protective suits (Fig. 3.3D). The outer suit was made of a Lycra®Nylon fabric laminated with a 1mm layer of polyurethane (PU) that ensures waterproofness. Seams were sealed by taping the same fabric from the inside (PU-PU connection). A waterproof zipper (TIZIP, MasterSeal 10, 500 mbar pressure proof) was used to open and close the suit. The purpose of the inner suit (made of soft fabric) was to protect the sensitive PU layer from sharp edges on the robot. In order to allow limb interaction with the environment also in water, the feet had to be kept outside the suit. Therefore, the steel rods at the crus/antebrachium were guided through a cylindrical silicone rubber piece that was glued inside the suit at each of the

limbs. The press fit between silicone and the rod ensures waterproofness. To provide power to the robot, we used IP67, Binder 693 series, 4-pole plug/socket connectors, as part of a 5 m tether (There is also the option to have a tether-less setup with a battery pack).

The swimming suit notably increases the volume of the robot, which increases the buoyancy. Therefore, the robot is not fully submerged in water. On the positive side this adds a stabilizing property (no rolling), however we noticed that lateral movement of the body was increased substantially, especially in the rostral part. Consequently, for the experiments we added a weight of 1.5 kg at the head as well as 1 kg at the level of the hind girdle. Furthermore, the air inside the suit was vacuumed to decrease the overall volume as much as possible.

3.3.4   Transformation to joint angles for Pleurobot

Finally, given the introduced design methodology, it is possible to impose kinematics recorded from the animal on Pleurobot. We will show in section 3.5 how this together with a careful scaling analysis (section 3.4) can be used to validate our design. To transfer the cineradiographic movement recordings to Pleurobot we solve two optimization problems related to the spinal and limb joints, respectively. Notice that in this optimization problem as opposed to the one for the robot design, the segment lengths are given and we solve for the joint angles. Motion sequences from the 3D reconstruction of the cineradiographic recordings contained between 12 and 190 time steps.

To compute the corresponding spinal joint angles for Pleurobot, the trunk and tail postures of *P. waltl* were first approximated using piecewise linear segments, where the length of each segment was given from the spinal segmentation on Pleurobot. Subsequently, at each time instance within a particular movement cycle (with 40 fps for swimming and 80 fps for walking), we solved an optimization problem as follows:

$$\{x_{i+1}, y_{i+1}\} = \min_{x_{i+1}, y_{i+1}} \left(\int_{x_i}^{x_i+1} \left| y_t(x) - (y_i + \frac{y_{i+1} - y_i}{x_{i+1} - x_i}(x - x_i)) \right| dx \right) \tag{3.1}$$

In this planar problem $y_t(x)$ describes the target posture in Cartesian coordinates. x_i and y_i denote coordinate points corresponding to the i-th joint on Pleurobot. As shown in the equation above, the optimization problems are solved sequentially, starting from the first (head) until the last joint (tail). The problem was solved using the unconstrained nonlinear optimization function fminsearch from Matlab, with default parameters. The solutions provide us with a piecewise linear approximation of the posture $y_t(x)$. Finally, the joint angles can be extracted by computing the relative angles between segments.

Related to the limb joint angles, the postures on *P. waltl* were identified by means of 5 tracking points located at the hip, the femur-crus joint, the crus-tarsus joint, the metatarsus-phalanges joint and the mid-phalanx tip (and corresponding points in the forelegs). The postures (again

at each time instance) had to be approximated by the segmented robot limbs, where the first segment represents femur/humerus and the second segment the connection from elbow/knee to the metatarsus. In order to compute the corresponding yaw, pitch, roll and elbow/knee angle we set up an inverse kinematics optimization problem for each posture:

$$\underline{\varphi} = \min_{\underline{\varphi}} \left(|p_{d1} - p_1(\underline{\varphi})| + |p_{d2} - p_2(\underline{\varphi})| \right) \tag{3.2}$$

$\underline{\varphi}$ describes the joint angles, p_{d1} and p_{d2} indicate the 3D positions of shoulder/hip and elbow/knee joints on *P. waltl* and the corresponding forward kinematics on Pleurobot are described by $p_1(\underline{\varphi})$ and $p_2(\underline{\varphi})$.

3.4 Dynamical Scaling

Ideally our robot should have a similar size as its biological counterpart. However, due to the unavailability of powerful miniature actuators at this stage in technology and our particular choice of servomotors, we are dealing with a robot that is geometrically scaled up by a factor of 8.6 with respect to *P. waltl.* Similarly to other studies (Dickinson et al., 1999; Taylor et al., 2003; Spence, 2009), it was therefore important to perform a dynamical scaling study so that the robot could faithfully be used to investigate locomotion of the salamander, in aquatic and terrestrial environments. This is necessary to ensure that the physical interactions with the environment are dynamically equivalent, for instance in terms of hydrodynamics regimes.

In this context, an important question was, how the robot should apply movements at speeds and while exerting forces that are comparable to the salamander. Based on the proposed design methodology, relative lengths of different body elements (geometric scaling) as well as the range of joint angles remained the same as for *P. waltl* (except for a 1.67 times increased robot head size, due to the placement of the control board). As a consequence it is also ensured that the robot operates in the same range of movements. To also incorporate the speeds and forces we used the criterion for dynamic similarity as defined by Alexander (2003):

$$\frac{mv^2}{Fl} = const. \tag{3.3}$$

Where m denotes the total body mass, v the forward moving speed and l the characteristic length of the robot. F describes the main forces that act on the system while moving. Dynamic similarity has been used to compare different types of gaits across animals as well as to analyze for instance the relation of mass and locomotion speed in animals of different sizes (Alexander, 1984; Gatesy and Biewener, 1991; Moretto et al., 1996). Let g, ρ, μ, f be the gravitational acceleration, fluid density, dynamic viscosity and the frequency, respectively, then the Froude ($Fr = v/\sqrt{gl}$), Reynolds ($Re = \rho l v/\mu$) and Strouhal ($St = fl/v$) numbers, are non-dimensional quantities that can be obtained from the dynamic similarity criterion (equation 3.3). The Froude number is typically used to compare walking gaits, where gravitational forces are dominant (Holmes et al., 2006).

By definition the Reynolds number determines the type of interaction forces with mainly viscous forces at low Re numbers and inertial forces at high Re numbers. The Re number was measured between $1.45 \cdot 10^4$ to $7.81 \cdot 10^4$ in the experiments with *P. waltl* and between $1.97 \cdot 10^5$ and $4.48 \cdot 10^5$ in our swimming experiments for Pleurobot. These high numbers indicate that both animal and robot are in a regime where inertial forces have a greater influence compared to viscous forces. Furthermore, it is important to notice that in the particular case of *P. waltl* (as well as Pleurobot) we are analyzing swimming at the water surface. Surface swimming is defined as swimming at a depth that is smaller than one body length (Burcher and Rydill, 1998; Moonesun et al., 2013). It is considered a special case as *"drag is increased substantially*

due to the formation of waves " (Johansson and Lauder, 2004) and the wave resistance force is a function of the Fr number (Hoerner, 1965). Therefore we can expect to have dynamically similar behavior at similar Fr numbers which is also supported by common practice in naval architecture (Gillmer, 2012), where the Fr number is used to create dynamically similar models of ships. Finally, related to periodic movements, the Strouhal number can be used to analyze movements at different frequencies. Intuitively, this measure covers observations in which smaller animals generally tend to move at much higher frequencies than bigger animals (Heglund et al., 1974).

Based on the Fr and St numbers, which should be the same for the robot and the animal, we use the subsequent scaling law to determine the corresponding speeds and locomotion frequencies on the robot in order to conserve dynamic similarity with *P. waltl*:

$$v_{robot} = \sqrt{\frac{l_{robot}}{l_{salamander}}} \, v_{salamander} \tag{3.4}$$

$$f_{robot} = \sqrt{\frac{l_{salamander}}{l_{robot}}} \, f_{salamander} \tag{3.5}$$

Accordingly, given that the ratio $\frac{l_{robot}}{l_{salamander}}$ is 8.6, we should be able to obtain dynamically similar behavior by scaling the salamander speeds by 2.94 and frequencies by 0.34 for walking and swimming.

3.5   Experimental validation of Pleurobot

To verify the design of our robot and to quantify the locomotor abilities with respect to *P. waltl* we carried out a series of experiments and compared kinematics as well as dynamics. For this, we replicated walking, swimming, and aquatic stepping gaits by replaying the precise body posture sequences that were obtained from cineradiographic recordings. Of course by design Pleurobot is made to incorporate all the necessary DOFs in order to replay fairly closely the joint kinematics for the three recorded gaits. But rather than focusing on the joint kinematics themselves, we ask the question of how the robot locomotes using those (i.e. how it progresses from one place to another and, more generally, how its orientation changes in 3D space).

The aims of the following experiments are: 1) to demonstrate that we can reproduce the two basic behaviors of the salamander so well that it has the potential to reproduce more complex locomotor behaviors if these are recorded from the animal, and 2) to validate whether replaying kinematics recorded from the animal, provided the scaling factors, can yield behaviors (i.e., Cartesian kinematics and ground reaction forces) comparable to the salamander's. Especially the second point will help validating future experiments in which Pleurobot is driven by a neuronal model instead of prerecorded animal kinematics.

3.5.1   Experimental setup for robot experiments

In order to capture the movements for the walking experiments of the robot we collected motion capture data (MOCAP). A total of 14 MOCAP cameras (Optitrack s250e, Naturalpoint, Inc. 2011) together with 13 infrared reflective markers (11mm) were used for this purpose. The markers were positioned at the each of the spinal joints (10 markers), additionally a rigid body marker (3 markers) was fixed on the head. Movements were recorded at 240 frames per second. Marker trajectories were processed in Arena (Naturalpoint, Inc. 2011) and Matlab (Matlab 2014b, MathWorks, Inc.). We conducted 5 experiments for frequencies of 0.1, 0.2, 0.3,.0.4, 0.5 Hz, where each experiment included 6 trials which were all part of the overall gait analysis.

The Swimming experiments were carried out in a pool with dimensions 6 m x 1.5 m with a water level of 18-22 cm. Movements were recorded with a camera (Canon PowerShot S120), which was mounted at a height of 2 meters over the pool at a frame rate of 30 frames per second and a resolution of 1920 x 1080. In addition we used a video tracking system as described in Crespi and Ijspeert (2008) to track an LED mounted on the robot. During the swimming experiments with the robot, the limbs were folded against the body. The forelimbs were folded underneath the body by positioning the humerus pointing backwards and parallel to the trunk, and fully flexing the elbow joint (as opposed to *P. waltl*, which extends the elbow joint). The hind limbs were also folded underneath the body in a way that is qualitatively similar to *P. waltl*, where the femur was positioned pointing backwards at about an angle of 45 degrees with respect to the trunk. The crus was extended at about 135 degrees (45 degrees from full extension). We chose for two reasons not to use the original limb trajectories during swimming as in *P. waltl*. First, constraints from the suit did not allow us to exactly reproduce the limb

kinematics in swimming, as the tension caused by the stretched material would have restricted the undulatory movements along the trunk. Second, using a fixed limb posture made the experiments more repeatable (same drag coefficient for same body shape) and allowed us to investigate and compare the movements along the spinal joints under same conditions for different swimming gaits. In any case, the limb movements of *P. waltl* during swimming are minimal. For the swimming experiments we considered two different animal gaits, which were tested at 4 different frequencies. To show the repeatability of the experiments, 3 trials each were performed.

3.5.2 Characterization of locomotion

To compare the movements between Pleurobot and *P. waltl* we investigated their lateral displacements and forward velocities. These quantities were measured with reference to the line of locomotion which was computed with the following linear regression:

$$\{m_k, q_k\} = \min_{m_k, q_k} \left(\sum_{i \in P_k} |y_i - m_k x_i - q_k|^2 \right) \tag{3.6}$$

, where k denotes the k-th cycle and m_k, q_k are the resulting slope and offset of the regression. P_k describes the set of all tracked spinal points with coordinates (x_i, y_i) in the k-th cycle. The robot lateral displacement for walking was computed based on the MOCAP recordings and from video data for the swimming gaits. In the case of swimming, characteristic midline points were computed in two steps. First, a curve was fitted (spline interpolation) through 21 manually selected points along the hypothetical midline of the body. Starting point of the midline was defined as the tip of the head and the end point was defined as the end of the tail. The midline was then resampled to 13 equidistant points. For *P. waltl* the corresponding measure was computed based on the cineradiographic tracking data.

Forward velocity of the robot was computed in steady state, which was reached starting from the second locomotion cycle for walking and starting from the third locomotion cycle for swimming. The corresponding forward displacement over time was then averaged over two cycles for walking and three cycles for swimming. The rigid body marker and the LED marker were used as reference markers, respectively.

Besides the above mentioned kinematic measures, we furthermore recorded ground reaction forces (GRFs) on the robot for part of the validation. In this context forces in three dimensions were recorded using force plates (type 9260AA3, Kistler, 2011) at a sampling frequency of 1 kHz. The GRFs were measured for both front and hind limbs the hind limbs. To select appropriate experimental runs for the analysis, video recordings were obtained during the measurements. Only experiments, in which the robot was walking straight and only a single foot was touching a force plate were taken into account. Finally, seven experimental runs for the front limbs and eight experimental runs for the hind limbs were selected for the analysis. The data was processed using Matlab (Matlab 2014b). The stance phases within a cycle were extracted using

the normal force profile for the front limbs (force indicating stance, no force indicating swing). For the hind limbs, as a matter of fact in many experiments the foot was slightly touching the ground when protracting. Therefore, the stance phase for the hind limbs was identified using the anteroposterior as well as the normal force profile. As such, the beginning of stance was identified as soon as propulsive force (retraction) was registered, while the end of stance (lift off) was defined when the normal force dropped to zero. This is consistent with the force measurements in (58), where propulsive stance also was analysed. Furthermore, forces were smoothed using a moving average filter ($N = 100$, over/under smoothing was checked visually). For the analysis the stance duration was normalized from 0 to 100% in order to compare the different experiments. All the forces were expressed with respect to the percentage of body weight, which facilitates the comparison to the salamander.

3.5.3 Walking

During ground locomotion, *P. waltl* typically uses two types of gaits, the walking trot and the lateral sequence walk (Delvolvé et al., 1997; Karakasiliotis et al., 2012). Both gaits involve trunk and tail movements that oscillate with an S-shaped standing wave. When well coordinated with the limbs, this allows the animal to maximize its stride length. As part of the validation we replicated an example lateral sequence walking gait on Pleurobot and discovered interesting similarities (Fig. 3.4).

Based on the scaling laws introduced in section 3.4, it can be shown that the stride length, which is defined as the forward speed normalized by the product of frequency and character-istic length, is a necessary quantity to be matched in order for two motions to be dynamically similar. The resulting stride lengths were measured in the range of 0.55 to 0.74 snout-vent length (SVL) of several repeated experiments at different frequencies on the robot (Fig. 3.5) and from 0.7 to 0.84 SVL for *P. waltl*. In this range we achieve the best matches at 0.2 Hz (7.8% error) and 0.3 Hz (3% error) with respect to the animal gait, which corresponds to a frequency of 0.19 Hz when dynamically scaled. The lower stride lengths can be expected and are in accordance with the abstraction of the ball-shaped feet, as propulsive power from the phalanges is not included. In addition to forward movement we also analyzed lateral displacement patterns (Inset in Fig. 3.5) as a mean to quantify characteristics perpendicular to the movement direction.

We found that the profile with the local minima at the two girdles could be reproduced indicating that the trunk oscillations comply with *P. waltl*. The smaller lateral displacement in the trunk is a result of the slightly different oscillation pattern along the line of locomotion, where the rostral part of the robot tends to oscillate more than that of the salamander (Fig. 3.4, lateral movement of the neck joint). Therefore the lateral oscillation span of the trunk along the line of locomotion is reduced

To quantify further similarities between the Pleurobot and *P. waltl* we compared the footfall patterns. For this purpose the absolute contact force at each individual foot was measured

using force sensors (Optoforce, OMD-D30 3D Force Sensor). A threshold of 7 N (10% Body weight) was used to discriminate between stance and swing. At the same time the limb kinematics were recorded via the joint encoders of the servomotors, which provided joint angle measurements at a sampling time of 12 ms with a resolution of 0.088°. As shown in Fig. 3.6 the forelimb footfalls can be accurately reproduced on the robot, showing very similar stance and swing durations as well as timings. The hind limbs of the robot show shorter stance durations than *P. waltl* (left hind: robot $53.38 \pm 0.99\%$ (*mean* $\pm$ *s.d.*), *P. waltl* $78.64 \pm 5.08\%$, $p = 2.84 \cdot 10^{-7}$, $\mu_{robot} > \mu_{animal}$ [2] ; right hind: robot $64.30 \pm 0.47\%$, *P. waltl* $80.06 \pm 4.29\%$, $p = 9.40 \cdot 10^{-8}$, $\mu_{robot} > \mu_{animal}$), which is expected because of the following reasons: the ball-shaped foot on Pleurobot represents the corresponding metatarsus in the animal and the phalanges are therefore not modeled on the robot. This is especially noticeable in the hind limbs, which have longer phalanges. As a result the hind limbs on the robot show systematically shorter stance durations, despite similar touch-down timings.

---

[2] we carried out standard t-tests with $\alpha = 0.05$ throughout this study, $\mu_i > \mu_k$ indicates the null-hypothesis. $p < 0.05$ indicates that the null-hypothesis should be rejected.
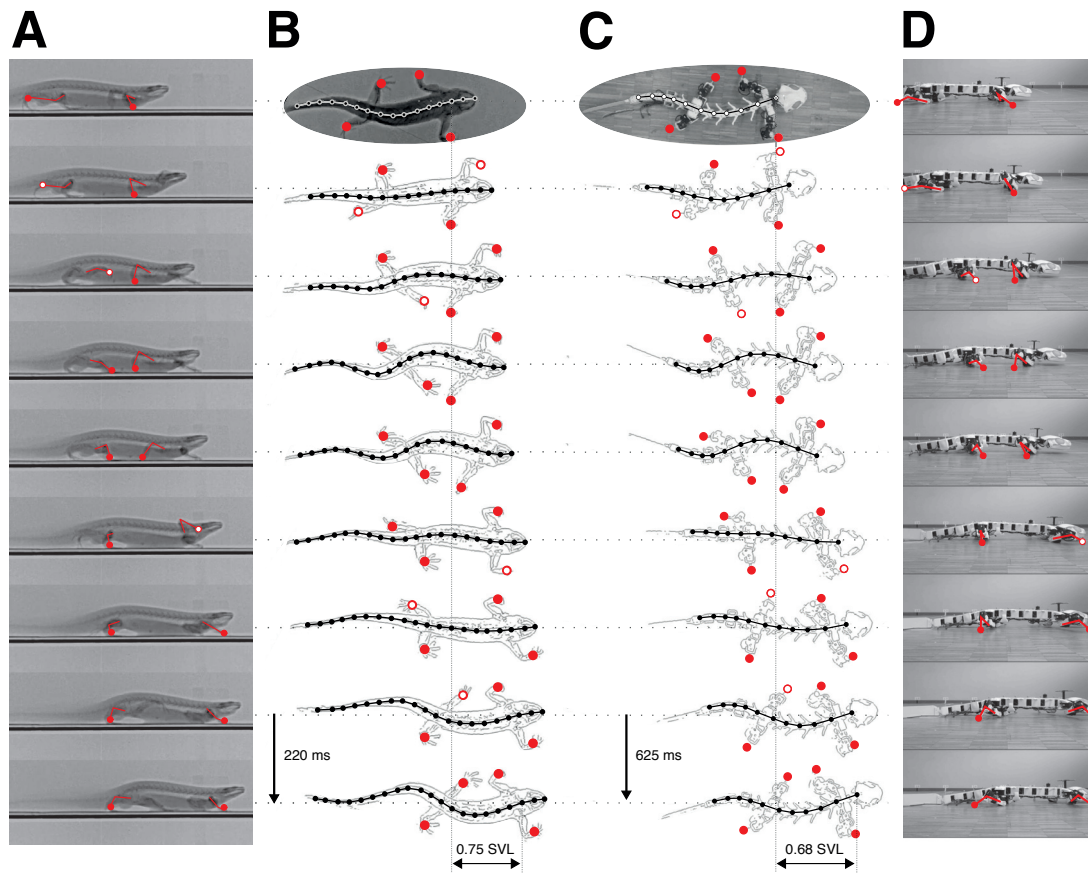
Figure 3.4 – **Comparison of walking gaits from *P. waltl* and Pleurobot**. The left side shows side view (A) and top view (B) of a *P. waltl* walking gait cycle at 0.57 Hz, obtained from cineradiographic recordings. The red filled circles indicate stance phase and the white filled circles indicate swing. The right side shows top view (C) and side view (D) of Pleurobot replaying the corresponding *P. waltl* gait at 0.2 Hz, respecting dynamic scaling. The fine dashed lines in the top views indicate the line of locomotion, computed as linear regression of all the midline points within the gait cycle. Stride lengths are indicated by means of snout-vent length (SVL).
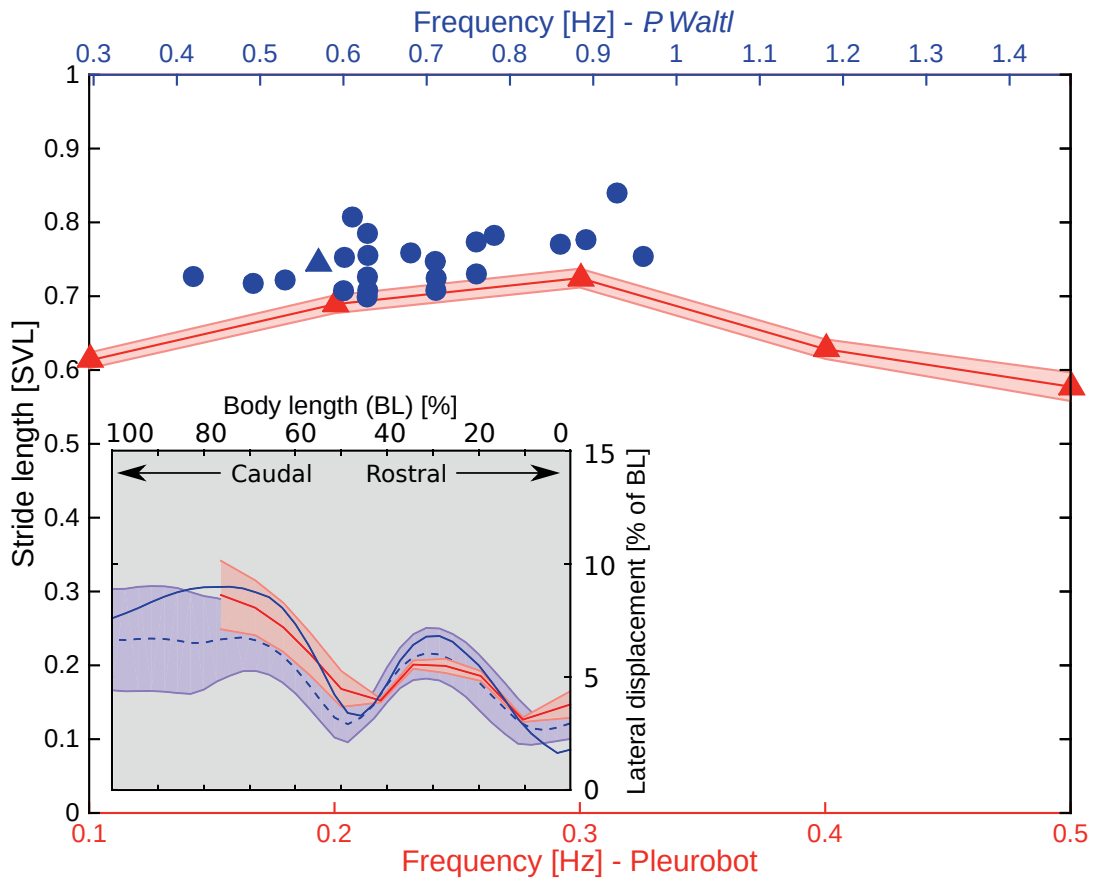
Figure 3.5 – **Similarities in stride length and lateral displacement for walking**. Stride length for walking was defined as forward speed divided by frequency normalized by snout-vent length. Data from *P. waltl* in blue and from Pleurobot are indicated in red. The Pleurobot data is represented as mean and standard deviation of 6 runs at frequencies 0.1, 0.2, 0.3, 0.4, 0.5 Hz. The frequencies of observed gaits from *P. waltl* are scaled based on the scaling laws for dynamic similarity with a factor of 0.34. The blue triangle represents the particular gait that was replayed on Pleurobot, blue disks represent other gaits from *P. waltl*. Inset: Lateral displacement for terrestrial stepping computed by means of maximal displacement from the line of locomotion. The blue shaded area shows mean (dashed line) and standard deviation of 23 cycles obtained from *P. waltl*. The blue solid line represents the particular *P. waltl* gait that was replayed. The red shaded area shows mean and standard deviation from 6 runs of the particular gait replayed on Pleurobot at 0.2 Hz.
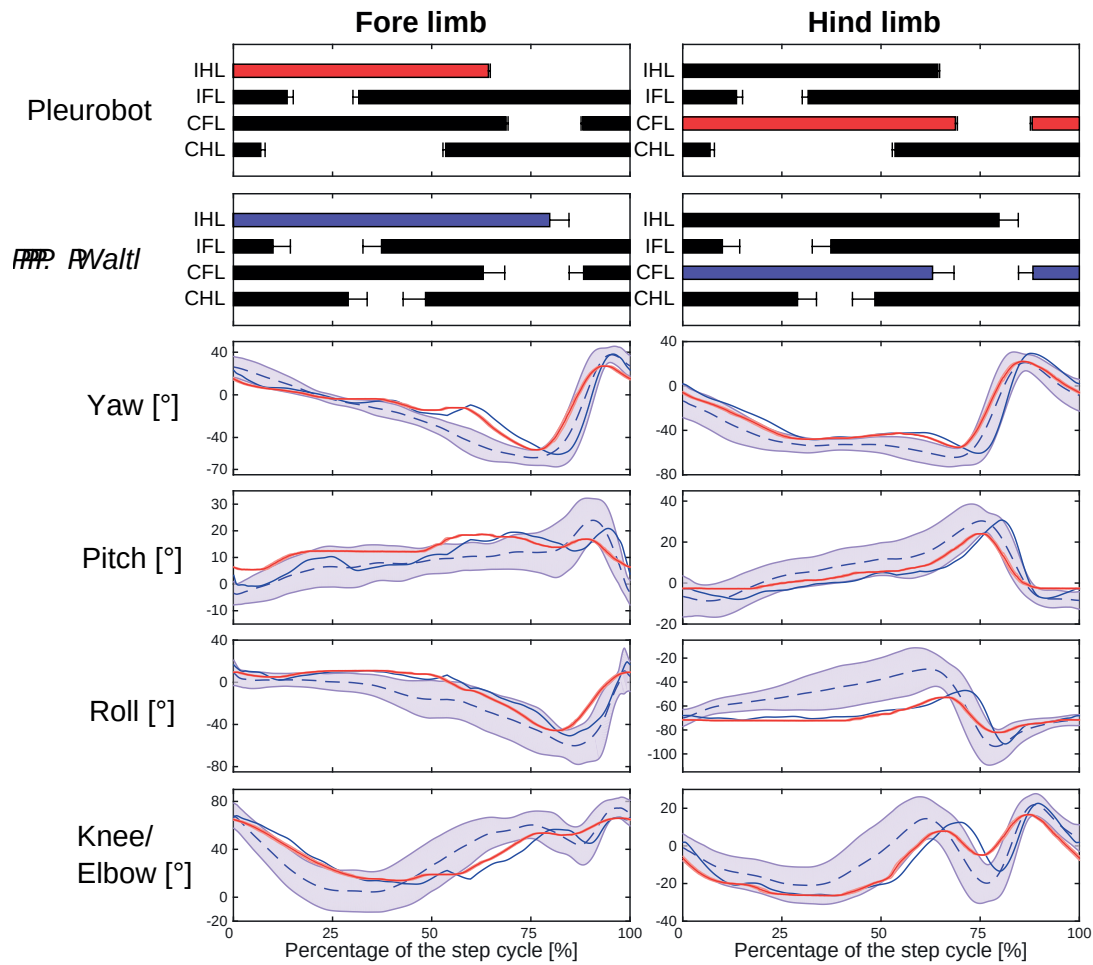
Figure 3.6 – **Similarities in limb kinematics and footfall patterns for walking**. The upper two panel rows represent Hildebrand diagrams showing stance (black) and swing (white) phases within a normalized gait cycle. IHL = ipsilateral hind limb, IFL = ipsilateral forelimb, CFL = contralateral forelimb, CHL = contralateral hind limb. The left side shows results for the hind limbs and the right side for forelimbs. In the other panels blue shaded areas represent mean and standard deviation of joint angle trajectories for *P. waltl* (23 cycles), blue solid lines indicates a particular salamander gait. Red shaded areas indicate mean (solid line) and standard deviation of the particular replayed gait on Pleurobot (5 gait cycles at 0.2 Hz, based on a scaling factor of 0.34 respecting dynamic similarity).

3.5.4 Swimming

Due to its amphibious nature, *P. waltl* can not only exploit gaits in terrestrial but also in aquatic environments. Two major steady state gaits can be observed: swimming and aquatic stepping. The latter is predominantly used when the animal is able to reach the aquatic ground with its limbs. It resembles a trotting pattern in which short power strokes of the diagonal limb pairs in coordination with spinal undulations lead to forward propulsion. Here we focus on swimming and ask whether we can replay gaits in the same way as we do for walking.

P. waltl swims using an anguilliform swimming gait in which a traveling wave of body undulation is propagated from head to tail (Ijspeert et al., 2007), (Fig. 3.7, left). The outcome in terms of forward propulsion for replayed salmander swimming gaits on the robot is more difficult to predict than for walking, as the dominant interaction forces (drag) are hard to estimate for a body with such a complex geometry. Nevertheless, the animal swimming gaits could be reproduced on the Pleurobot as shown in Fig. 3.7, demonstrating similar forward progression and overall attitude between animal and robot along the line of locomotion. *P. waltl* showed a great variety of stride lengths across different recorded gaits ranging from 0.17 BL (BL: Body length) up to 0.5 BL. Similar to the Axolotl (*Ambystoma mexicanum*), also an anguilliform swimmer, these stride lengths are achieved not only by changing the frequency but also by changing the amplitude profile along the body (D'Août and Aerts, 1997). In our experiments we observed for example significantly increased tail amplitudes in gaits with a higher resulting stride length.

When replicating swimming gaits with large amplitudes and high frequencies we observed large tracking errors (Appendix C, Fig. C.1). This is related to the torque and speed limits of the motors, which result in a limited control bandwidth. Therefore, we focused our analysis on gaits with smaller stride lengths. Subsequently, the reproduced gaits (Fig. 3.8) resulted in a similar range of stride lengths as the corresponding from the salamander (robot: $0.21 \pm 0.05 BL$ ($mean \pm s.d.$); salamander: $0.22 \pm 0.04 BL$; $p = 0.55$, $\mu_{robot} = \mu_{salam}$).

Note that the decrease of stride length with frequency in the robot is likely due to an increase of tracking errors that prevent the exact replication of the gaits at higher frequencies (Appendix C, Fig. C.1). This explains why the stride lengths are smaller in the robot at frequencies of 1.18 Hz and 1.28 Hz (blue square and triangle in Fig. 3.8) that would be required for both animal gaits based on the scaling analysis.

We were able to obtain a very similar lateral displacement profile (Inset in Fig. 3.8) showing increasing values from head to tail. Indicating that on the robot, as on its biological counterpart, the lateral movement of the rostral part is kept minimal.
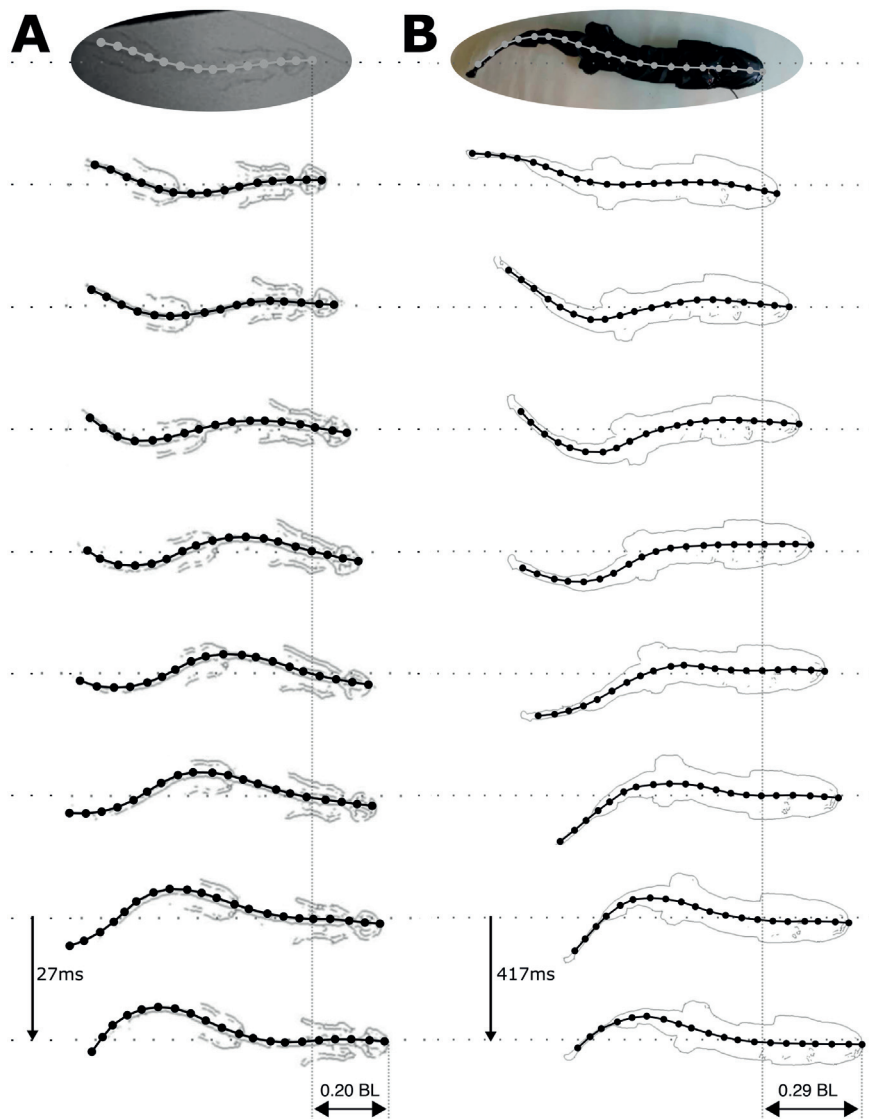
Figure 3.7 – **Comparison of swimming gaits from *P. waltl* and Pleurobot**. (A) shows a *P. waltl* swimming gait cycle at 3.8 Hz from top to bottom divided in 9 snapshots. (B) shows the same gait replayed on Pleurobot at 0.3 Hz. The bold dotted line indicates the midline of robot and animal. The horizontal fine dotted lines indicate the line of locomotion, computed with a linear regression of all the midline points within a gait cycle.
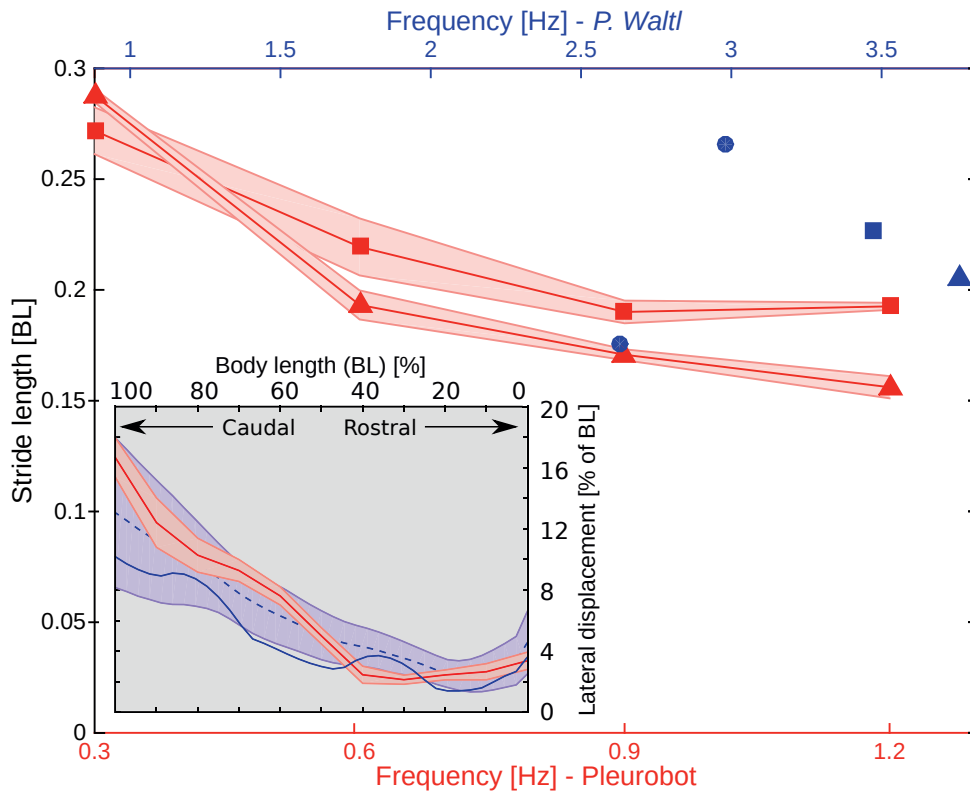
Figure 3.8 – **Similarities in stride length and lateral displacement for swimming**. Stride length for swimming was defined as forward speed divided by the frequency and normalized the body length. Data from *P. waltl* is shown in blue and from Pleurobot in red. The Pleurobot data is represented as mean and standard deviation of 3 runs each at frequencies 0.3, 0.6, 0.9, 1.2 Hz. The observed gait frequencies from *P. waltl* are scaled based on the scaling laws with a factor of 0.34. The blue triangle and square represent the particular gaits that were replayed on Pleurobot represented as red triangles and squares, respectively. The blue circles show two additional trials from *P. waltl*. Inset: Lateral displacement for swimming computed by means of maximal displacement from the line of locomotion. The blue shaded area shows mean (dashed line) and standard deviation of 20 cycles obtained from *P. waltl*. The blue solid line represents a particular *P. waltl* gait that was replayed. The red shaded area is showing mean and standard deviation from 10 runs of the particular gait replayed on Pleurobot at 0.3 Hz.

3.5.5 Ground reaction forces: comparison between salamanders and Pleurobot

We finally asked how the interaction forces between the robot and the environment along with the kinematics relate to *P. waltl* and quantified them by measuring ground reaction forces (GRFs) for a walking gait. Based on the scaling law for speed, equation (1) (dynamic similarity) reduces to the ratio of body weight and the experienced external force. Therefore, we can expect dynamic similarity between Pleurobot and *P. waltl* when the external forces (GRFs) normalized by the body weight are similar.

GRF measurements obtained for Pleurobot were compared to data from Kawano and Blob reported for *Ambystoma tigrinum* (Kawano and Blob, 2013), since measurements were not available for *P. waltl*. Compared to *P. waltl* (mean stride length: 0.75 SVL) similar stride lengths were observed for the *Ambystoma tigrinum* (mean stride length: 0.68 SVL for forelimbs, 0.73 SVL for hind limbs, SVL: 0.1m, BL: 0.187m, (Kawano and Blob, 2013)). The results of the GRF analysis are presented in Fig. 3.9, where the salamander shows characteristic normal peak forces at 60.2% stance for the front limbs and at 24.7% of the stance phase for the hind limbs. It indicates that the front limbs are making a significant effort to push the body weight off the ground in the second half of the stance whereas the hind limbs have to bear most of the vertical load in the beginning of the stance phase. Experiments of walking with the robot showed qualitatively similar normal force profiles, where normal forces peaked at ($61.2 \pm 1.3\ \%$ ($mean \pm s.d.$), $p = 0.1$, $\mu_{robot} = \mu_{animal}$) for forelimbs and ($27.3 \pm 1.5\ \%$, $p = 0.002$, $\mu_{robot} = \mu_{animal}$ [3]) for hind limbs. Furthermore, the *Ambystoma tigrinum* systematically showed GRFs in medial direction (front: -0.047 ± 0.011 %BW ($mean \pm s.d.$), $p = 1$, $\mu < 0$; hind: -0.042 ± 0.02 %BW, $p = 1$, $\mu < 0$) (i.e. external forces with respect to the salamander point medially for both forelimbs and hind limbs), suggesting that the salamander pushes its legs laterally from the body during stance. These characteristics are partially reproduced by the forelimbs of the robot, which in average also produce a positive lateral push (-0.035 ± 0.043 %BW), but not for the hind limbs (-0.003 ± 0.025 %BW) where a mostly neutral trend is observed.

Finally, the data from Kawano and Blob (2013) shows that most of the propulsion in the salamander is generated by its hind limbs indicated by the anteroposterior forces, which are close to zero (-0.011 ± 0.015 %BW) for the front limbs and systematically positive (propulsive) for the hind limbs (0.097 ± 0.042 %BW, $p = 1$, $\mu > 0$). We could find the same characteristics for the corresponding robot gait (front: -0.007 ± 0.040 %BW; hind: 0.077 ± 0.058 %BW, $p = 1$, $\mu > 0$), although showing larger fluctuations in force magnitude in the front limbs.

---

[3]notice that the values differ statistically, however there is a qualitative similarity
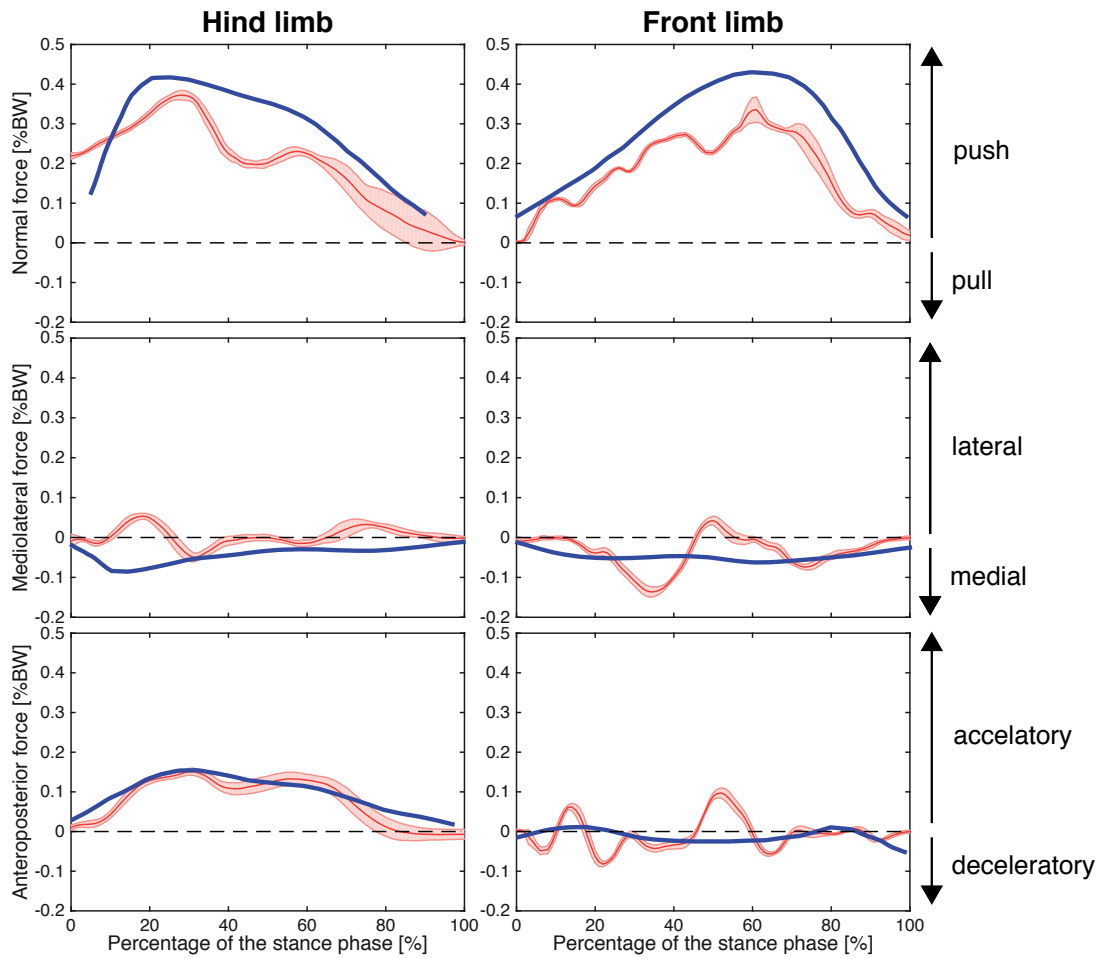
Figure 3.9 – **Comparison of ground reaction forces (GRFs) in the *Ambystoma tigrinum* and Pleurobot**. Hind (left side) and front (right side) limb GRFs were measured and analysed with respect to normal, sideways and forward contribution. Red shaded areas represent Pleurobot experiments (7 cycles for forelimbs and 8 cycles for hind limbs) with mean and standard deviation. The blue solid lines indicate mean data from the *Ambystoma tigrinum* (58). The forces were normalized by means of body weight and only propulsive stance was considered for the analysis. The dashed line indicates zero forces.

3.6 Discussion

We presented a possible way of designing biorobots in a systematic way and outlined the design procedure, which is based on high-speed cineradiographic recordings and numerical optimization, along with kinematic and dynamic validation respecting physics scaling laws. We used the approach to construct Pleurobot, a salamander-like robot with 27 DOFs that can emulate the walking and swimming gaits of the salamander *P. waltl*.

It could be seen as trivial that Pleurobot's locomotion matches that of the real salamander since the robot replays the sequence of animal postures. Moving a robot with predefined joint angle trajectories is indeed trivial in the sense that it will, given a good controller and strong actuators, produce the expected robot postures. However, unlike automatons in amusement parks that are solidly fixed to the ground, Pleurobot's displacements in 3D space are the results of (complex) physical interactions between the robot internal movements and the environment. The robot must be properly designed such that the interaction forces match those of the animal (Aguilar et al., 2015). For instance, during ground locomotion, inaccurate mass distribution could lead to incorrect body orientations and incorrect contacts to the ground (e.g. a limb not touching the ground when it should) and hence different locomotor patterns and locomotion speeds. Similarly, the swimming of the robot could be very different from that of the animal if geometrical and dynamical properties of the robot had not been properly adjusted with the dynamic scaling. The indirect (stride lengths and lateral displacements) and direct (ground reaction forces) comparisons between robot and animal presented here indicate that the interaction dynamics closely correspond.

Our approach results in a physical tool that provides an interface between computational models and the environment on which rich motor skills can be tested in the future. The success of our approach is of course tested with behaviors with slow dynamics like the ones typically seen in salamanders and in particular *P. waltl*. In principle it could be applied to the design of other types of robots that match different animals and modes of locomotion provided that the model is able to capture the dynamic conditions. Cineradiography allows one to observe bone movements, from which detailed and accurate kinematic information can be extracted. This allows one to identify locomotion-relevant joints (active or passive). Compared to motion capture based on markers and cameras, it prevents possible problems of movements of surface markers due to motion of soft tissues (Miranda et al., 2013), and of occlusions. It has however the disadvantages that more work is required to extract the 3D data frame by frame from the biplanar images (either manually, like in our case, or through machine vision algorithms), and that the recording volume is limited.

In our case with *P. waltl*, optimization based on kinematic data was then sufficient to find a good robot design. We were able to replay gaits on the robot without modulating gaits based on feedback. For other animals and other modes of locomotion, similar steps could be taken but additional mechanical design and control steps could be necessary. For instance, it might be needed to use remote actuation with cables in order to obtain the right mass-distribution

as for the cat-like robot Cheetah-Cub (Spröwitz et al., 2013). Different gaits on other robots might also need explicit feedback control (e.g. for balance), whereas we are benefiting from the intrinsically stable sprawling posture of the salamander. The choice of servomotors was convenient in our design of a salamander-like robot. It highly decreases the time and cost to build and transform. However, more generally, other actuators (e.g. with low gear ratio, passive elements, etc.) could be used depending on the type of locomotion and the questions that have to be addressed.

We furthermore applied the scaling laws that have to be respected in order to obtain dynamic similarity between the robot and the animal. For the salamander it was shown that the Froude number had to be used for walking and surface swimming. In other cases such as e.g. deeper 3D swimming (depth larger than a body length), the Reynolds number should be used.

The analysis of footfall patterns and the aquatic stepping experiments revealed limitations in the current design of Pleurobot with respect to its biological counterpart *P. waltl*, indicating that the role of the phalanges is important for stepping locomotion (in terrestrial and aquatic environments). The abstraction of the feet to single contact points is an important simplification which makes Pleurobot less of an anchor than the original aim. However, future versions will focus on integrating as many aspects of the foot as possible given their complexity. Furthermore, actuator limitations in size and power currently restrict the reproduction of some dynamically similar swimming motion, especially at higher frequencies and stride lengths. However, our approach shows promising results for the reproduction of walking patterns of the salamander *P. waltl* that conserve respective characteristics such as stride length, footfall patterns as well as similar ground reaction forces.

One aspect that we did not address is internal dynamics (Ding et al., 2013), i.e. how internal forces and torques generate body deformations (i.e. postures). In the animal, body deformations are due to sets of muscles acting on the joints, while in the robot they are due to torques produced by the PD controllers of the servomotors. There are some similarities between the two types of actuation, since with the proportional P and derivative D gains elasticity and damping can be adjusted to some extent. Nonetheless, there are also important differences: (i) antagonist muscles allow the change of stiffness, and (ii) multi-articular muscles act on more than one joint. Muscle properties can be simulated if the gearboxes are back-drivable (or torque sensors with very fast control loops are available) and when the motors are used to control direct torque output. Given motors with these properties, this will allow us in the future to investigate the role of muscle properties in locomotion and to address questions related to locomotion efficiency (for instance how to obtain a given speed with minimal muscle activation, i.e. minimal metabolic cost). There is also the possibility to add elastic elements in series (Tsagarakis et al., 2013; Spröwitz et al., 2013; Pratt and Williamson, 1995) to provide mechanical elasticity and energy restoration.

In the future, we envision Pleurobot as a useful tool for neuroscience. Locomotion is the result of interaction of many components, and a physical model like Pleurobot can provide the

interface between, on one hand, computational models of the nervous system and of muscles, and, on the other hand, physical interactions with terrestrial and aquatic environments. As a realistic physical model of the salamander capable of emulating basic and complex behaviors, it can serve to test hypotheses about the interactions between the different components underlying locomotion, in particular the interactions between descending modulation, central pattern generation, sensory inputs and interaction forces from the environment. Compared to our previous robots and previous studies, the robot will for instance allow us to investigate (i) the organization of the limb CPGs with multiple neuronal oscillators (similarly to what has been found in the salamander (Cheng et al., 1998)), (ii) the effect of adding more descending pathways to our spinal cord models, and (iii) the generation of a larger variety of motor behaviors such as turning, walking backwards, scratching, paddling, etc.

Obviously, it is by performing these future studies that we will really validate the design methodology presented in this article and its usefulness for neuroscience. It is possible that additional design iterations might be needed (for instance with the addition of more degrees of freedom, the replacement of motors with stronger ones, the use of cables for remote actuation, the addition of sensors, etc), but the current robot already opens the door to many investigations.

Furthermore, other fields, including functional morphology, paleontology and field robotics, might benefit from the robot or its design methodology. In terms of robotics, an amphibious salamander-like robot capable of locomotion in different environments could find useful applications for inspection or search-and-rescue operations.

3.7 Conclusion

In summary, we proposed a design method to create physical robotic models which can be used to investigate locomotion. We showed the importance of dynamical scaling for this model and the corresponding movement patterns in a bimodal environment. Validation in walking and swimming experiments showed that the imposed body movements resulted in similar locomotion performances compared to the biological counterpart. Measurements of the reaction forces during walking revealed similar corresponding characteristics.

Nevertheless, we encountered also limitations in locomotor performance (e.g. for higher frequency swimming, or lateral ground reaction forces during walking), which is highly expected as our approach to control the physical model was very simple by just imposing overall body postures. No control link (sensors!) between the environment and the pattern generation was implemented yet, which we showed in the previous chapter, can greatly help to improve locomotion. Together with this, ideally, a physical model as presented here can be used to test future mechanisms for movement generation (chapter 2), that explain how these movement patterns can be generated and adapted with respect to the environment.

3.8 Acknowledgments and Contributions

4 Conclusion

We investigated and analyzed various types of locomotion in the course of this thesis. The principal questions focused on the role and influence of the environment on how movements emerge and movement patterns are generated.

In the first chapter of this thesis we had a closer look at insect walking and asked to what extent the environment shapes fast gaits for six-legged locomotion. An *in-silico* model of *Drosophila* was created and enabled to explore a variety of inter-leg coordination patterns. Using a Particle Swarm Optimization we derived speed-optimal gait patterns in different environmental conditions. Environmental constraints for fast climbing movements, which are adhesion to the ground and walking against gravity, resulted in the tripod gait as optimal solution. Relaxing those environmental constraints to fast walking on flat ground, where adhesion is not required and gravity is acting normally to the moving direction, a different optimal gait pattern was found, namely a bipod gait.

The second chapter investigated environmental influences on a different level. Rather than focusing on the performance of a variety of gait patterns in different environmental conditions, we asked which particular mechanisms (feedfoward vs feedback control) for pattern generation are actually necessary to exploit a specific given environment. This was explored for undulatory swimming, where we introduced pressure sensing as the means to obtain a genuine link between movement generation and resulting reaction forces with the surrounding water. Using local sensory pressure feedback loops we proposed three distinct control paradigms. They revealed how the sensor link to the environment could 1) adapt traveling wave patterns towards faster and more energy-efficient locomotion, 2) could be used to establish coordinated traveling waves in a decentralized local control scheme and 3) could even be used as a means to generate purely sensory-driven rhythms for undulatory locomotion. The findings are intriguing from a biological point of view. It indicates that there are two redundant mechanisms for generating coordinated wave patterns: central coupling and sensory feedback. This implies a good robustness of the locomotor system, for instance, to handle lesions along the spinal cord.

Chapter 3 investigated the role of real-world models that in contrast to computational simulated models have a great potential to emulate realistic reaction forces between body and environment. Physical models can be placed in the real environment and do not rely on models of reaction forces. In the example of the salamander-like robot Pleurobot, we highlighted challenges, as the physical model has to respect dynamical scaling constraints in order to be a valid tool for investigations of locomotion. Based on our design methodology and experiments in terrestrial and aquatic environments we showed that the model can emulate similar characteristics in terms of overall locomotion (stride lengths, footfall patterns) and reaction forces on ground.

A central aspect of the presented work has been the use of mathematical models and robots to investigate locomotion. As we showed, they proved to be very fruitful to understand and discover new locomotion-relevant mechanisms. Traditional methods such as neurophysiological or biomechanical experiments provide detailed measurements of the nervous system (neural activity), muscle apparatus (EMGs) or about body movements (ground reaction forces, kinematics). Although these measurements contribute to valuable insights into the functions of those components, a key limitation lies in the ability to modify characteristic parameters (e.g. neural coupling or muscle properties) in these subsystems. It is much easier, however, to do so if models of the respective locomotor components are available. We could draw the abstract analogy to a black box vs a parametrized model. It is of course possible to characterize a black box system based on recordings of different inputs and outputs, however it is much harder to link the corresponding data to internal properties and dynamics of the system. Using a parametrized model, however gives us the freedom not only to look at responses to different stimuli, but additionally to investigate the characteristics of the system with regard to changing parameters. Of course we have to be aware that no perfect models exist, so there is always a trade-off between the explanatory power and the constraints based on assumptions under which a model is valid. Nevertheless, I believe that our results in this work encourage the use of models for investigations of locomotion. Ideally, they should be combined with traditional methods, which can serve as an additional validation of corresponding model-derived findings.

As part of the modeling, robots were used to validate the concepts derived in simulated environments. This can help to validate them with respect to real-world reaction forces as shown in the last study. Besides the validation aspect, we could also draw beneficial conclusions for engineering applications. Locomotion is of great importance, as mobility is a key ability to communicate and excel in our modern societies. In different marine, urban or aerial environments, mobility and thus to some extent locomotion is required to transport goods, to explore surroundings or to interact with people. Our studies did certainly not target such explicit applications to serve for, however some general principles could still be valuable in this context. Legged locomotion is especially beneficial in cluttered environments, where wheeled vehicles have more difficulties. Stability in these environments becomes a great challenge, which is why researchers have turned to legged robots with six legs, where the tripod gait offers a statically stable gait with three contact points on the ground at any time.

As an outcome of our first study, we proposed a faster bipod gait that can be used with six legs. Although less stable (dynamic instead of static stability), this gait could serve as an alternative in situations where higher speeds are desired. The results in the second chapter also contributed to potentially more efficient swimming robots, which could highly benefit from energy recovery mechanisms. Furthermore, ideas of decentralized distributed control could reduce control complexity of undulatory swimming robots, increase modularity and reconfigurability of such robots, as well as self-tuning of locomotion patterns for robots with different properties (e.g. different joint friction or damping).

Looking back at the beginning of this manuscript, three important aspects for locomotion were postulated: *reaction forces between body and environment, inherent movement generation in the body, and adaptation / synchronization of body and environment.* In this thesis, we used them as main components of our models and depending on the questions that were investigated, these aspects were explored and exploited with the corresponding necessary levels of abstraction. Throughout all the chapters we highlighted the importance of the environment, which has a major influence in imposing and shaping corresponding gait patterns of moving bodies, to the extreme, where body movements can be generated through purely sensory driven loops. Using these models in combination with robots also led us to interesting conclusions for engineering applications.

4.1 Future Work

This section of the manuscript is probably the most rewarding to write in my opinion. Although, we almost reached the end, I see the work that has been presented here as a starting point. Many interesting topics have been introduced and I believe that there is a lot more worth exploring.

In the first study about insect walking, we explored environmental constraints that led to tripod and bipod gaits as speed optimal solutions, as an outcome of our extensive gait exploration. In a next step, it would be worth investigating how these gait patterns are created, and ask which mechanisms for the generation of body movements could be responsible for the emergence of the respective gaits. Integration of feedback loops could provide relevant mechanisms for adaptations within specific environments prone to changing conditions. This could, on the one hand, suggest robust ways how to tackle different environments with hexapod robots and on the other hand, lead to valuable insights into the neural organization responsible for walking in insects.

Obviously, the main aspect that was missing in the undulatory swimming study is a validation of the results in a real-world environment. Our model relies on simulated hydrodynamics. Although, validated for a selection of open loop patterns in the past (Porez et al., 2014), final evidence that the local sensory feedback loops enable movement generation and adaptation in water needs to be provided. Initial experiments with a swimming robot proved to be promising, which encourages a detailed evaluation and hopefully validation of the key findings. Moreover,

based on the simulation results in terms of speed and energy consumption, along with a potential recovery strategy based on restoration of negative work, there seems to be great potential for a highly efficient swimming robot. Using the findings from decoupled oscillators that coordinate via pressure feedback, the robot could furthermore be controlled with such a strategy. The self-organizing property would enable a high modularity, where as a result, the control of the robot becomes independent of the number of segments, as each segment would be programmed identically. Going even a step further one could imagine having a very long chain of segments that, if needed, could be split into several independent swimmers. Using ideas from distributed intelligent systems, one could further coordinate them depending on the given tasks.

From a more modeling point of view, it will be important to asses the robustness of the different control schemes to external perturbations, such as variable flow streams, sensor noise or obstacles. Also the scalability of the results to other Reynolds regimes (e.g. viscous swimming) would be an interesting direction to investigate, however one could expect different results as the dynamics and thus the types of reaction forces will change.

Our proposition for the development of a physical model that can be tested in a real world environment with real physics and interaction forces led us to the salamander-like robot Pleurobot. So far we managed to show and validate its use for walking and swimming locomotion. The salamander, however, has a very rich repertoire of locomotor skills which include among others also aquatic stepping, where limbs are actively used in water. Initial data showed that this gait is efficient in terms of transferring movements into forward propulsion (stride length). This particular gait is also interesting from an evolutionary point of view, where it is assumed that animals transitioned from water to land. One key aspect that could have made this transition possible is the development of limbs. Even more it has been hypothesized that limbs encouraged and facilitated the transition to terrestrial habitats as they already proved to be advantageous in water (Clack, 2002a,b). A robotic platform similar to Pleurobot could help to systematically test this hypothesis in controlled experiments. A second important improvement involves the actuation of the developed salamander-like robot. So far the motors that we used, operate in high gain position control. This makes it difficult to test and validate neuromechanical control models, as these models rely on torque as output of the motors (muscles produce forces). Future upgrades of motors and additional torque sensors could resolve these issues.

4.2 Final words

The ability to locomote, meaning to move its own body from one place to another, is crucial for almost all living creatures, that need to survive in their immediate environment. Catching prey, procreation or relocation depending on environmental constraints are a few basic examples. Locomotion is a very diverse phenomenon and we can find plenty of varieties thereof in nature. Each one of them is adapted with respect to animal body morphologies and to the corresponding environments they live in. In this thesis, we developed specific computational and physical models and investigated different types of locomotion based on different aspects such as 1) reaction forces between body and environment, 2) generation of body movements and 3) adaptation / synchronization between body and environment. Our main findings explain the prevalence of tripod gaits in insects, the discovery of a new bipod gait for hexapedal walkers, generation of spontaneous traveling waves in undulatory swimmers based on decoupled oscillator networks influenced by local sensory feedback, as well as based on purely sensory-driven control without neural oscillators. Moreover, we presented a generic methodology to design physical models to explore locomotion based on cineradiography and dynamical scaling laws on the example of a salamander-like robot. The general work in this thesis dealt with highly abstracted models to capture the most important features of particular locomotion patterns and enabled both insights into biological aspects as well as interesting considerations for engineering systems.
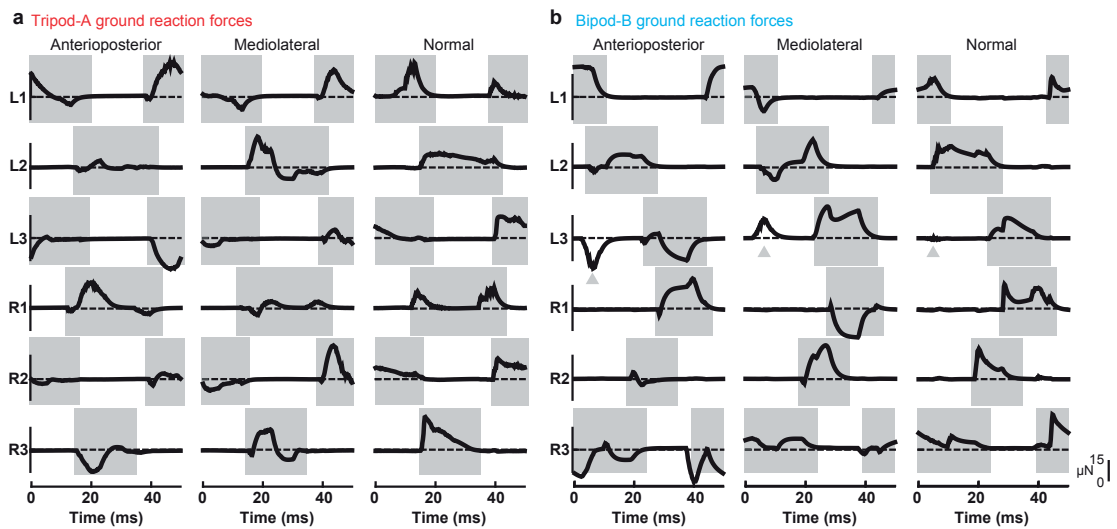
A Supplementary Figures: Insect walking

Figure A.1 – **Ground reaction forces for the insect model.** Ground reaction forces (GRFs) for ideal **(a)** tripod-A and **(b)** bipod-B gaits. Shown are GRFs for each leg along the anterioposterior axis (left; positive values indicate GRFs pointing in the forward direction – propulsive forces), mediolateral axis (middle; positive values indicate GRFs pointing medially), and normal axis (right; positive values indicate GRFs pointing away from the surface). Gray boxes highlight stance epochs for each leg during tripod-A and bipod-B locomotion. Gray arrowheads indicate an instance of ground contact with minimal normal force.
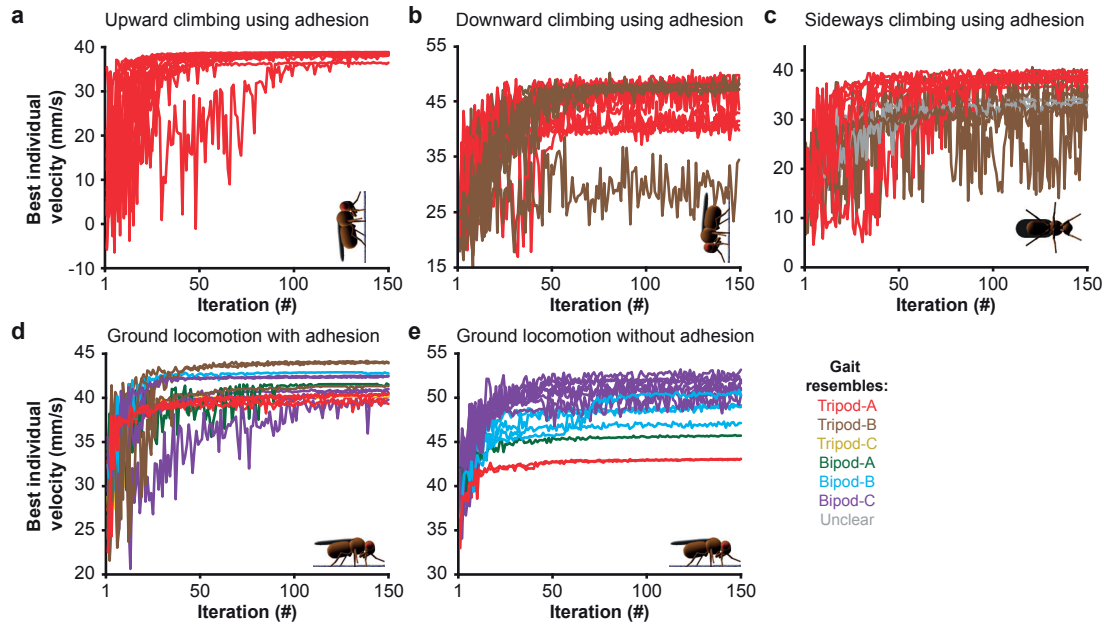
Figure A.2 – **Convergence of fastest forward locomotor velocities during gait optimization.** Forward velocities of the fastest individuals for each iteration during gait optimization for forward velocity while **(a)** climbing upward, **(b)** downward, **(c)** or sideways on a vertical surface using leg adhesion, **(d)** walking on the ground with leg adhesion, or **(e)** walking on the ground without leg adhesion. N = 15 experiments per condition. Each trace represents a single experiment and is color-coded according to the gait class of the experiment's fastest individual.
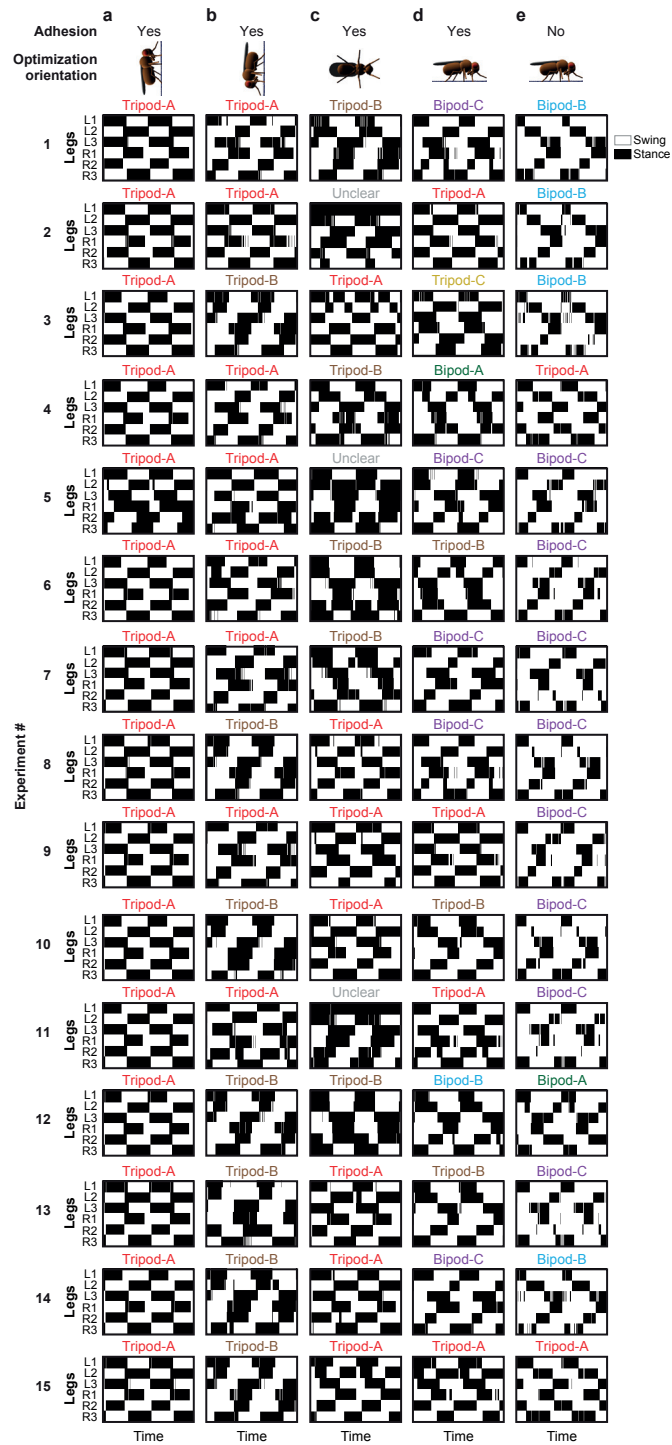
Figure A.3 – **Footfall diagrams for each optimized gait.** Footfall diagrams showing stance (black) and swing (white) periods for each experiment. Shown are results for gait optimization of forward velocity while **(a)** climbing upward, **(b)** climbing downward, **(c)** or climbing sideways on a vertical surface using leg adhesion, **(d)** walking on the ground with leg adhesion, or **(e)** walking on the ground without leg adhesion.
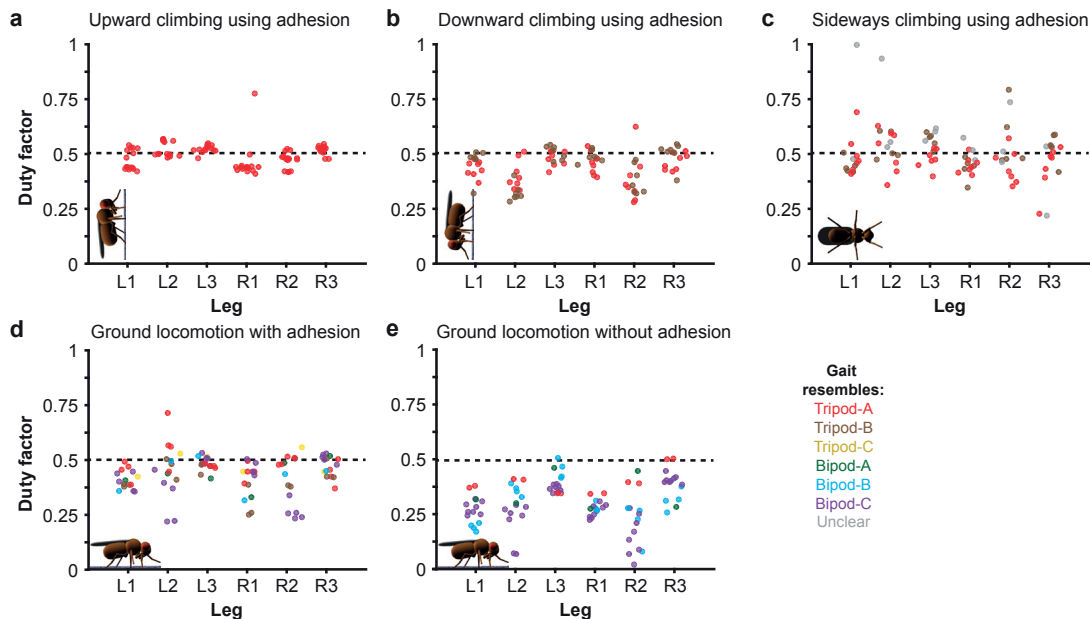
Figure A.4 – **Duty factors for each optimized gait.** The duty factor or fraction of time each leg is in contact with the substrate relative to the stride period for all optimized gaits. Shown are duty factors of gaits optimized for **(a)** climbing upward, **(b)** climbing downward, **(c)** or climbing sideways on a vertical surface using leg adhesion, **(d)** walking on the ground with leg adhesion, or **(e)** walking on the ground without leg adhesion. A dashed black line indicates 50% time in contact with the substrate. Optimized gaits are color-coded by class. Data points are randomly scattered along the x-axis for clarity. N = 15 for each condition.

Figure A.5 – **Cost of transport for optimized gaits.** The cost of transport (dimensionless) of gaits optimized for forward velocity while climbing upward (left), climbing downward (center-left), or climbing sideways (center) on a vertical surface using leg adhesion, walking on the ground with leg adhesion (center-right), or walking on the ground without leg adhesion (right). Optimized gaits are color-coded by class. Data points are randomly scattered along the x-axis for clarity. N = 15 for each condition.
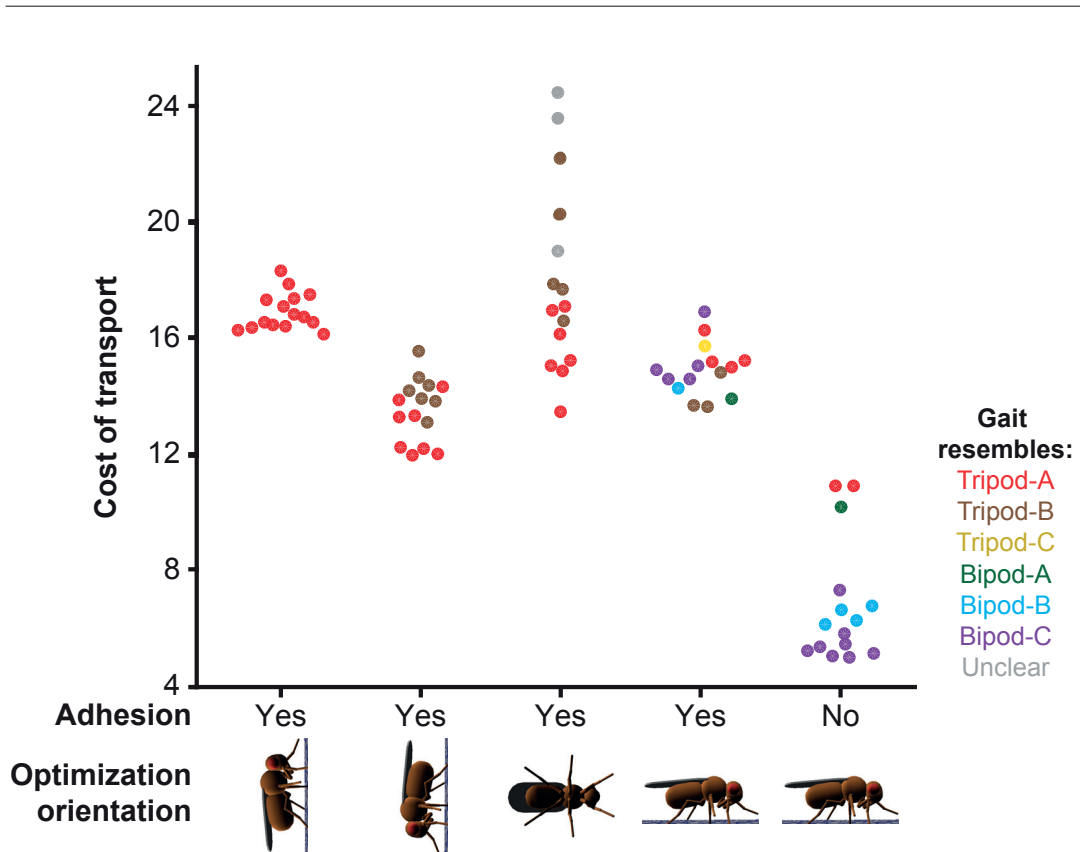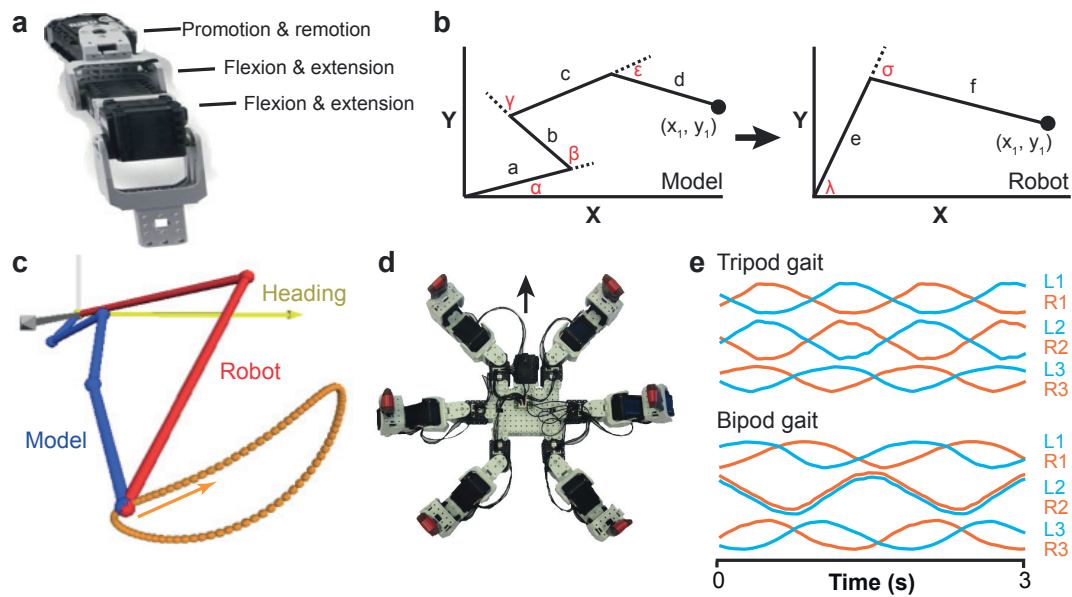
Figure A.6 – **Transferring bipod and tripod gaits to a hexapod robot. (a)** Image of the robot's leg. Degrees of freedom for each joint are labeled in black text. **(b)** Inverse kinematics approach for mapping the position of the robot's pretarsus (x1,y1) to the model's pretarsus despite a reduction from four to two flexion/extension joints. Joint angles are indicated in red. Leg segment lengths are shown in black. **(c)** Visualization of a matched leg trajectory (orange) for the right middle leg pretarsus of the robot (red) and the model (blue). A yellow arrow indicates the direction of heading. **(d)** To track the robot's legs automatically, red tape was affixed to their tips. A black arrow indicates the direction of heading. **(e)** The forward displacement of each of the robot's legs during tripod (top), or bipod-B (bottom) locomotion. Scale bar is 6 cm.
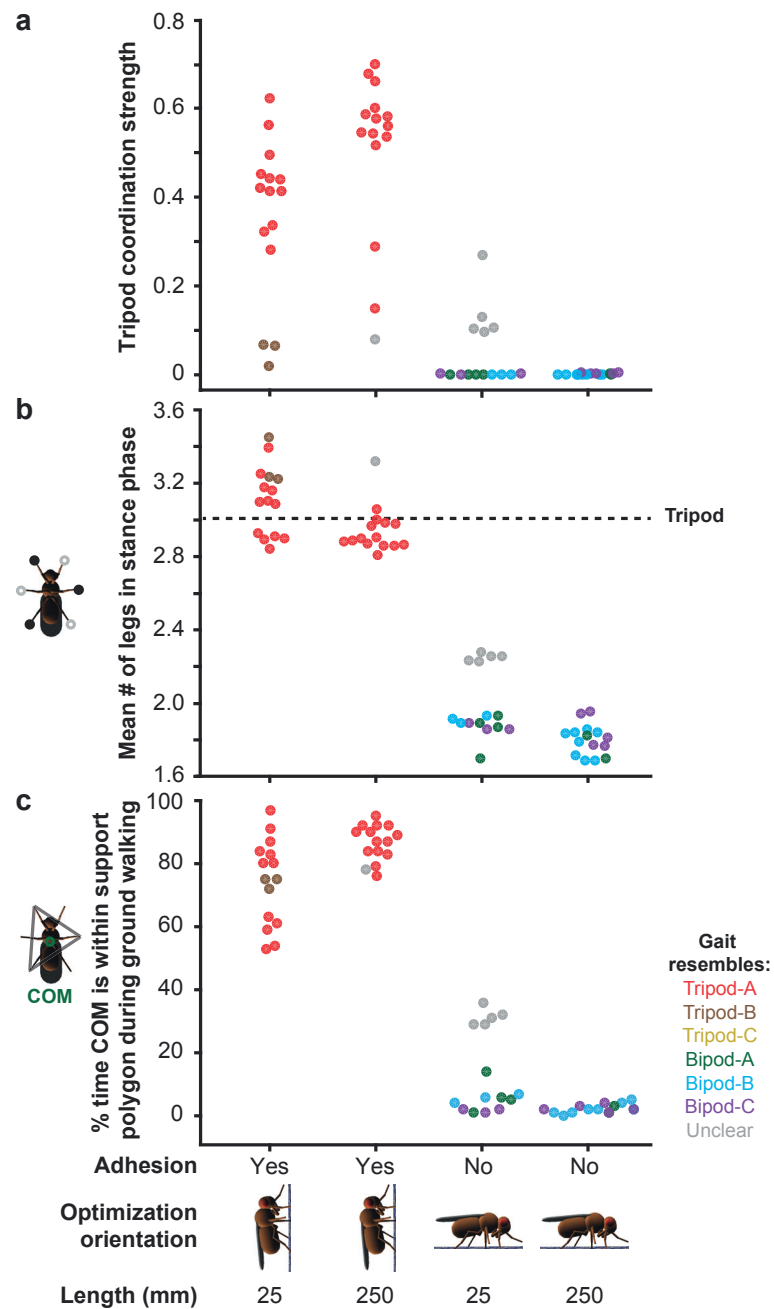
Figure A.7 – **Optimized gaits for models of different sizes.** Gaits were optimized for 25 mm, or 250 mm long models for forward velocity while climbing upward (left and middle-left), or walking on the ground without leg adhesion (middle-right and right). **(a)** Tripod coordination strength (TCS) values indicating the degree of similarity to the classic tripod gait footfall diagram (tripod-A). **(b)** The average number of legs in stance phase over five walking cycles. A dashed black line indicates three legs in stance phase as expected for the classic tripod-A gait. **(c)** The percentage of time that the model's Center-of-Mass (COM) lies within a polygon of support delineated by each leg in stance phase when the gait is tested during ground walking. Optimized gaits are color-coded by class. Data points are randomly scattered along the x-axis for clarity. N = 15 for each condition.

B Supplementary Figures: Undulatory Swimming
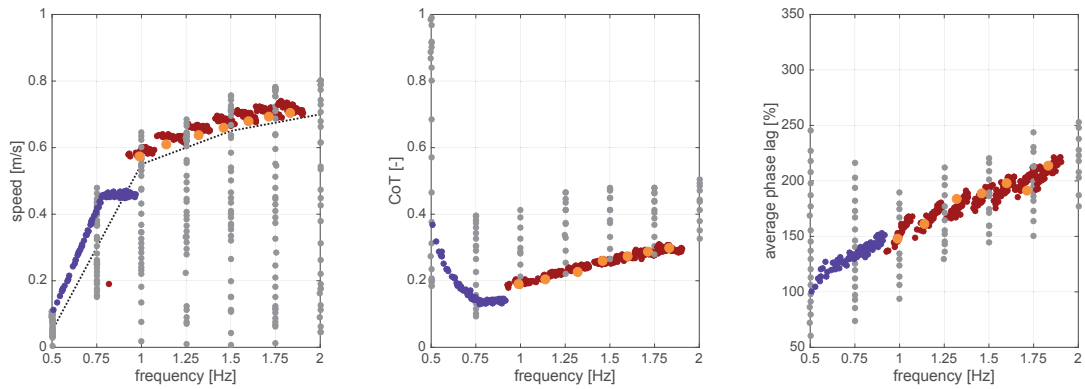
Figure B.1 – **Comparison of models I, II, II and open loop - 20 joint model**. Open loop patterns (gray), *Combined model* I (red), *Decoupled model* II (orange) and *Sensory-driven model* III (purple). Muscle parameters for Open loop, model I, II and III correspond to $\alpha = 1$ Nm and $\gamma = 2$ Nm/rad, $\delta = 0.1$ Nms/rad and $w_{fb} = 1$. For Model III nominal phase lags as well as feedback gains were varied. Based on a threshold minimum speed for different frequencies (dashed line), only COT and average phase lags above this threshold are presented. (**left**) Mean speed (**middle**) Cost of transport (**right**) Emerged average phase lag.
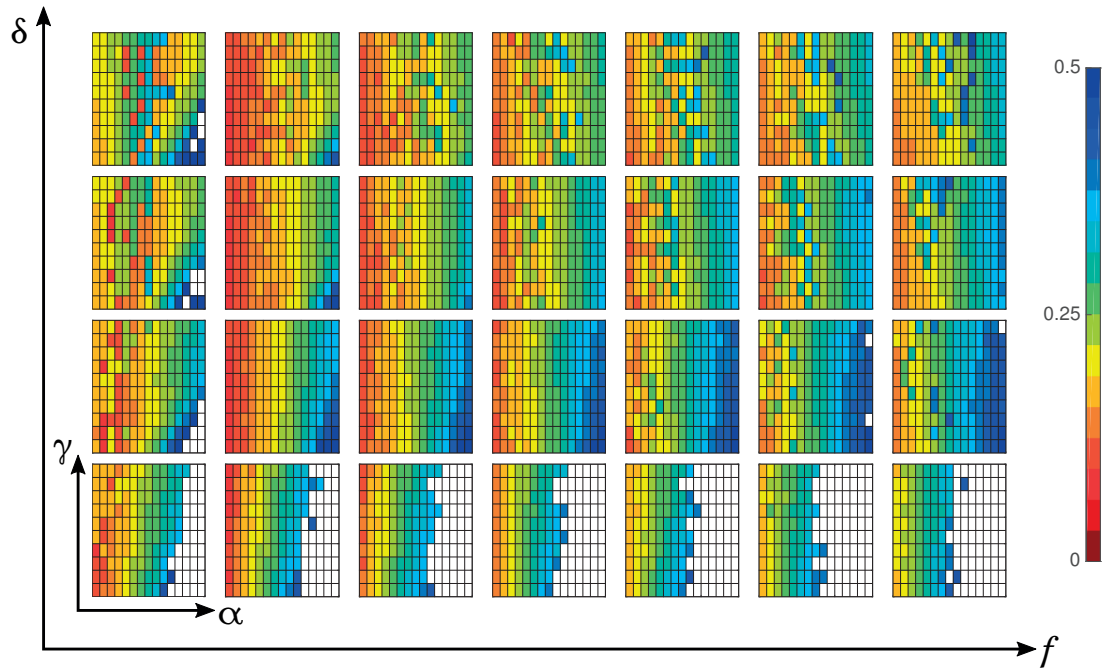
(a) Cost of Transport
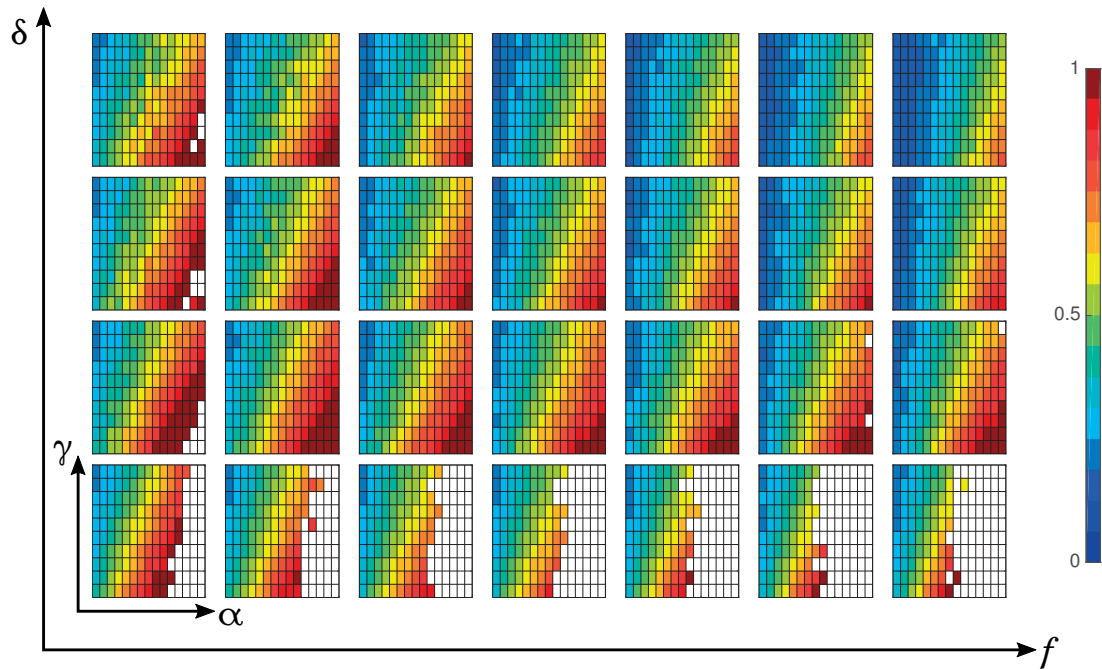
(b) Amplitude

Figure B.2 – **Parameter exploration for the *Combined model*.** Uniform variation of intrinsic oscillator frequency ($f = [0.5, 2.0]$ Hz), activation gain ($\alpha = [0.5, 2.0]$ Nm), stiffness ($\gamma = [1.0, 2.0]$ Nm/rad) and damping ($\delta = [0.05, 0.2]$ Nms/rad). Nominal phase lag is set to 200% (2 body waves). White areas indicate non-periodic solutions. Amplitude is represented by average amplitude of the 4-th joint.
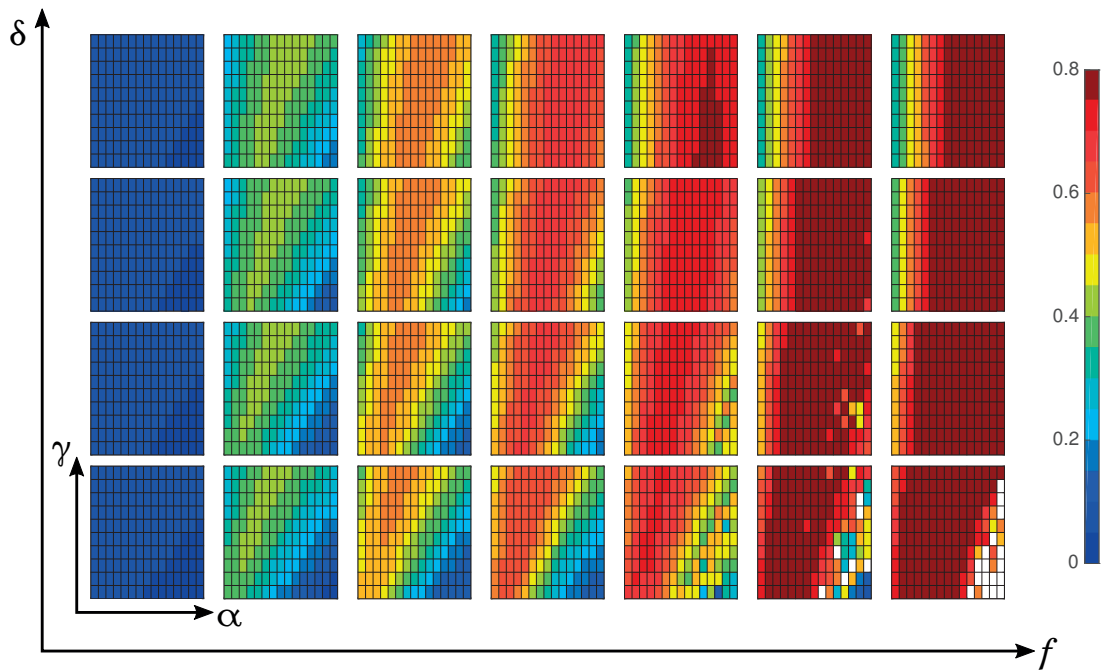
(a) Speed
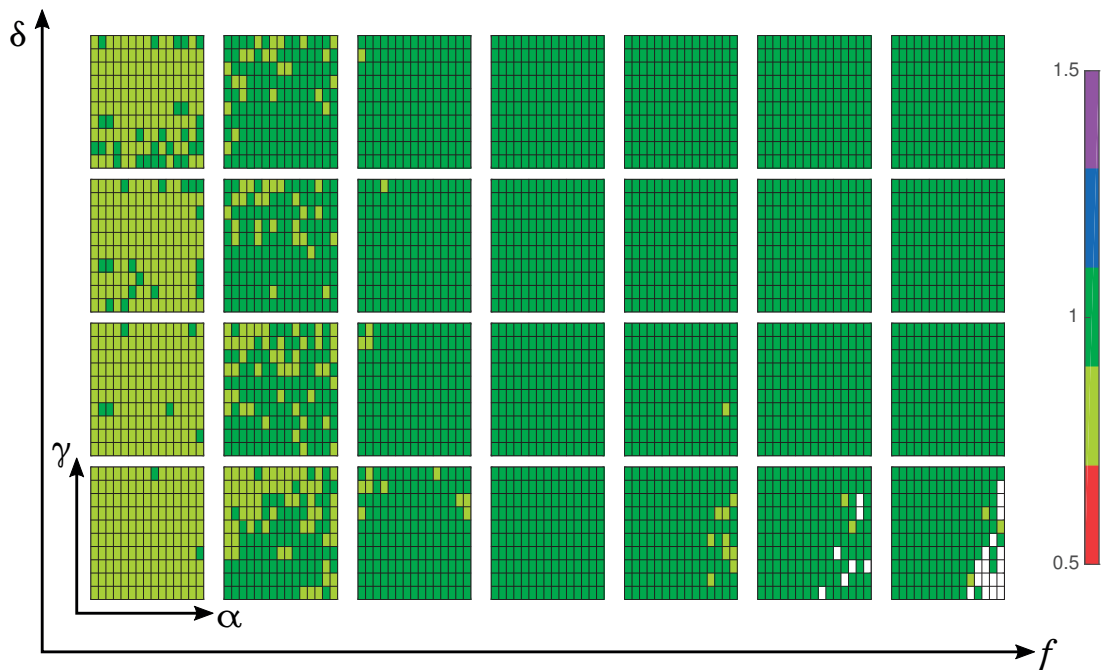
(b) Phase lag

Figure B.3 – **Parameter exploration for the Open loop case**. Uniform variation of frequency (f = [0.5, 2.0] Hz), activation gain (α = [0.5, 2.0] Nm), stiffness (γ = [1.0, 2.0] Nm/rad) and damping (δ = [0.05, 0.2] Nms/rad). Phase lags are given in terms of number of body waves. Nominal phase lag is set to 100 % (1 body wave). White areas indicate non-periodic solutions.

(a) Cost of Transport

(b) Amplitude

Figure B.4 – **Parameter exploration for the Open loop case**. Uniform variation of frequency ($f = [0.5, 2.0]$ Hz), activation gain ($\alpha = [0.5, 2.0]$ Nm), stiffness ($\gamma = [1.0, 2.0]$ Nm/rad) and damping ($\delta = [0.05, 0.2]$ Nms/rad). Nominal phase lag is set to 100 % (1 body wave). White areas indicate non-periodic solutions. Amplitude is represented by average amplitude of the 4-th joint.

C Supplementary Figures and Tables: Bimodal Locomotion
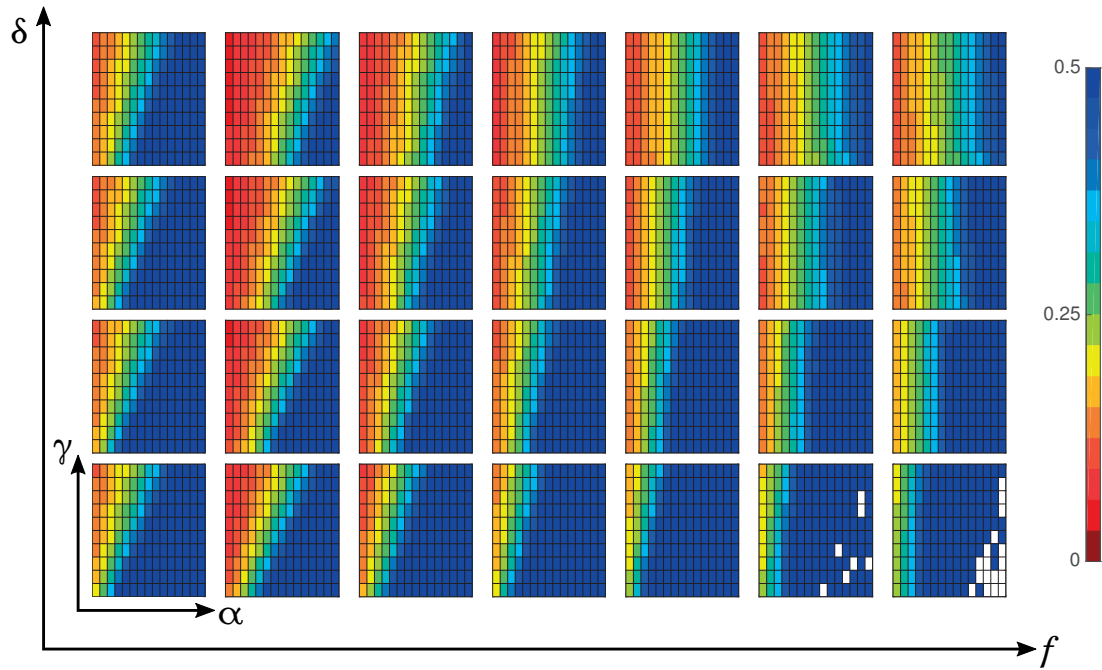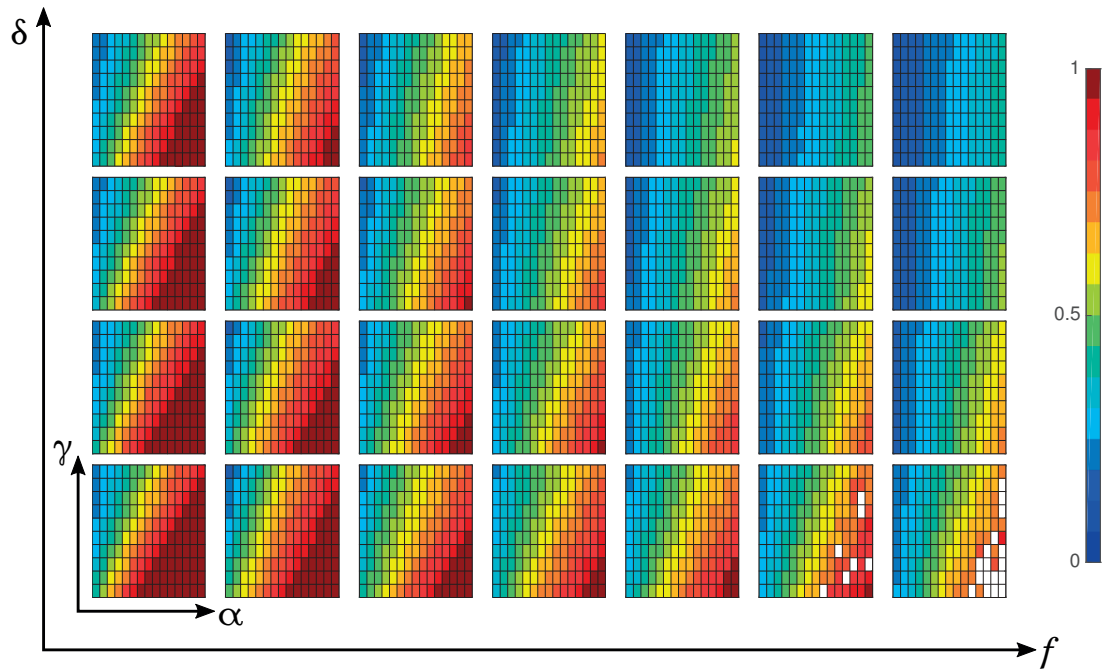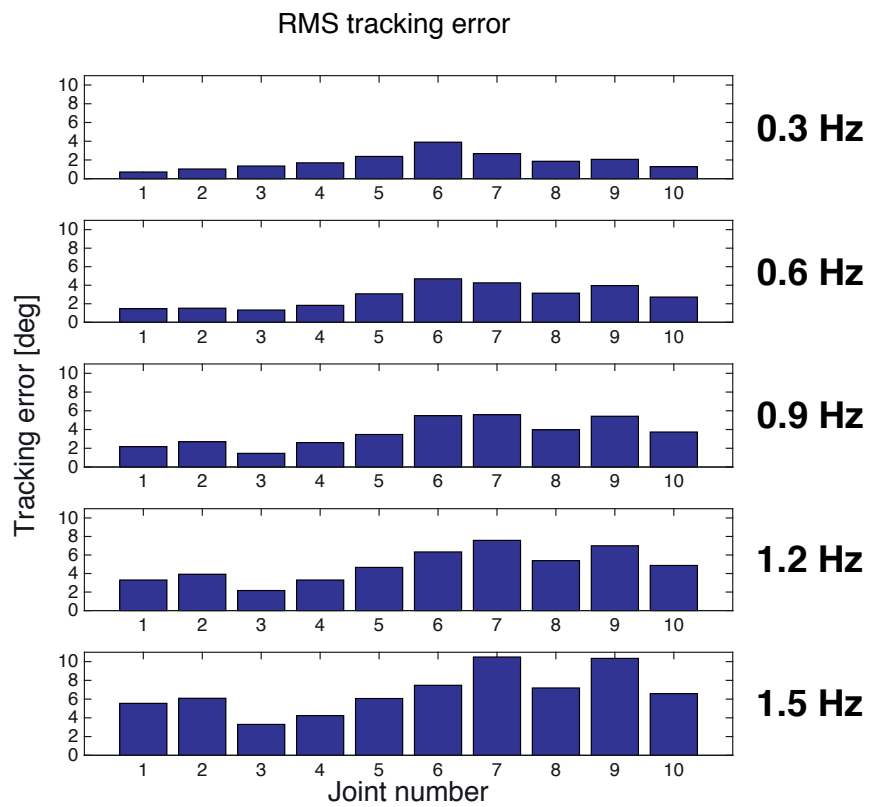
RMS tracking error

Figure C.1 – **Tracking error of servomotors** Defined as root mean square (RMS) error of desired and actual robot trajectories, for a swimming gait replayed at different frequencies are shown.
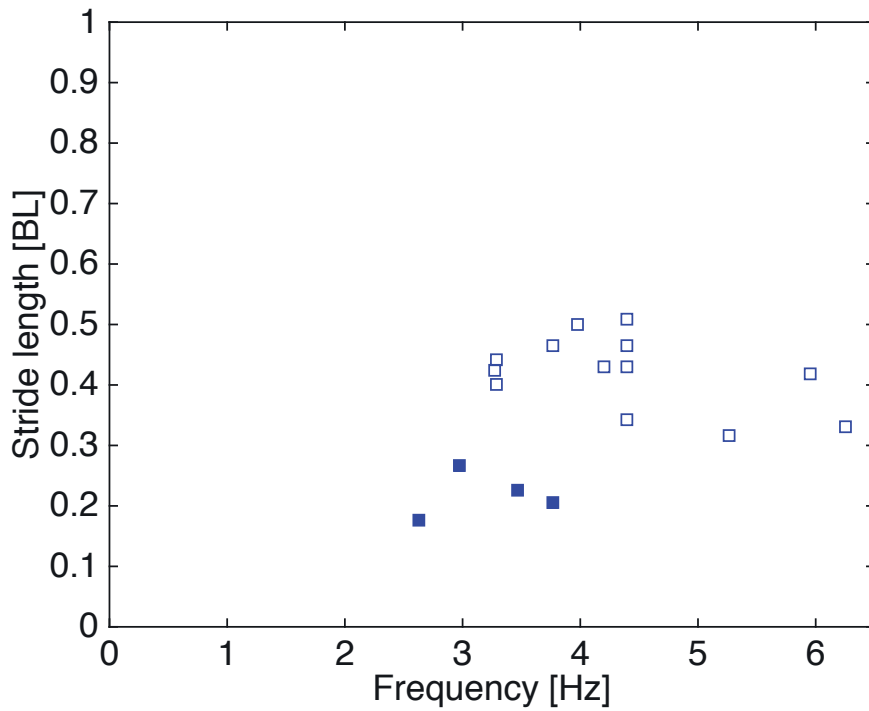
Figure C.2 – *Pleurodeles waltl* **stride lengths for swimming.** All stride lengths for swimming of the *Pleurodeles waltl* gait cycles are shown. Filled squares indicate gaits with lower stride lengths.

Component	Specifications
Control board	SBC-TITPC2i Single Board Computer
Suit material	Lycra® Nylon laminated with Polyurethane (PU)
Waterproof zipper	TIZIP, MasterSeal 10, 500mbar pressure proof
3D printed head	Material: Natural polyamide
3D printed spinal elements	Material: Glass-filled polyamide
3D printed limb elements	Material: Aluminum-filled polyamide
Silicone rubber feet	Material: RTV-Silikon SCS-SN 2888
Head motor	Dynamixel MX-28
Remaining motors	Dynamixel MX-64R

Table C.1 – Pleurobot hardware components

Bibliography

M. Ackermann and A. J. Van den Bogert. Predictive simulation of gait at low gravity reveals skipping as the preferred locomotion strategy. *Journal of biomechanics*, 45(7):1293–1298, 2012.

J. Aguilar, T. Zhang, F. Quian, M. Kingsbury, B. McInroe, N. Mazouchova, C. Li, R. Maladen, C. Gong, M. Travers, R. L. Hatton, H. Choset, P. B. Umbanhowar, and D. I. Goldman. Locomotion robophysics: the study of movement at the intersection of robotics, soft matter and dynamical systems. *Reports on Progress in Physics*, 2015. under review.

R. M. Alexander. Walking and running: Legs and leg movements are subtly adapted to minimize the energy costs of locomotion. *American Scientist*, pages 348–354, 1984.

R. M. Alexander. *Principles of animal locomotion.* Princeton University Press, 2003.

L. S. Andersson, M. Larhammar, F. Memic, H. Wootz, D. Schwochow, C.-J. Rubin, K. Patra, T. Arnason, L. Wellbring, G. Hjälm, and others. Mutations in DMRT3 affect locomotion in horses and spinal circuit function in mice. *Nature*, 488(7413):642–646, 2012.

E. Andrada, J. Mämpel, A. Schmidt, M. S. Fischer, and H. Witte. From biomechanics of rats' inclined locomotion to a climbing robot. *Int. J. Des. Nat. Ecodyn.*, 8:191–212, 2013.

E. Arzt, S. Gorb, and R. Spolenak. From micro to nano contacts in biological attachment devices. *Proceedings of the National Academy of Sciences*, 100(19):10603–10606, 2003.

M. A. Ashley-Ross. Hindlimb kinematics during terrestrial locomotion in a salamander (*Dicamptodon Tenebrosus*). *Journal of experimental biology*, 193:255–283, April 1994.

A. T. Baisch, C. Heimlich, M. Karpelson, and R. J. Wood. HAMR3: An autonomous 1.7 g ambulatory robot. In *2011 IEEE/RSJ International Conference on Intelligent Robots and Systems*, pages 5073–5079. IEEE, 2011.

O. R. Barclay. The mechanics of amphibian locomotion. *J. exp. Biol*, 23:177–203, 1946.

B. Bayat, A. Crespi, and A. J. Ijspeert. Envirobot: A bio-inspired environmental monitoring platform. In *Autonomous Underwater Vehicles (AUV), 2016 IEEE/OES*, pages 381–386. IEEE, 2016.

Bibliography

R. D. Beer and J. C. Gallagher. Evolving dynamical neural networks for adaptive behavior. *Adaptive behavior*, 1(1):91–122, 1992.

J. A. Bender, E. M. Simpson, B. R. Tietz, K. A. Daltorio, R. D. Quinn, and R. E. Ritzmann. Kinematic and behavioral evidence for a distinction between trotting and ambling gaits in the cockroach Blaberus discoidalis. *Journal of Experimental Biology*, 214(12):2057–2064, 2011.

A. Bicanski, D. Ryczko, J.-M. Cabelguen, and A. J. Ijspeert. From Lamprey to Salamander: an exploratory modeling study on the architecture of the spinal locomotor networks in the salamander. *Biological cybernetics*, pages 1–23, 2013.

A. Billard and A.J. Ijspeert. Biologically inspired neural controllers for motor control in a quadruped robot. In *Neural Networks, 2000. IJCNN 2000, Proceedings of the IEEE-INNS-ENNS International Joint Conference on*, volume 6, pages 637–641. IEEE, 2000.

R. Blickhan and R. J. Full. Similarity in multilegged locomotion: bouncing like a monopode. *Journal of Comparative Physiology A*, 173(5):509–517, 1993.

F. P. Bowden and D. Tabor. *The friction and lubrication of solids.* Oxford Clarendon Press, 1950.

E. L. Brainerd, D. B. Baier, S. M. Gatesy, T. L. Hedrick, K. A. Metzger, S. L. Gilbert, and J. J. Crisco. X-ray reconstruction of moving morphology (XROMM): precision, accuracy and applications in comparative biomechanics research. *Journal of Experimental Zoology Part A: Ecological Genetics and Physiology*, 313(5):262–279, 2010.

R. Burcher and L. J. Rydill. *Concepts in submarine design.* The press syndicate of the University of Cambridge., Cambridge university press, 1998.

U. Bässler and A. Büschges. Pattern generation for stick insect walking movements—multisensory control of a locomotor program. *Brain Research Reviews*, 27(1): 65–88, 1998.

M. Béguer-Pon, M. Castonguay, S. Shan, J. Benchetrit, and J. Dodson. Direct observations of American eels migrating across the continental shelf to the Sargasso Sea. *Nature Communications*, 6:8705, October 2015.

J.-M. Cabelguen, C. Bourcier-Lucas, and R. Dubuc. Bimodal Locomotion Elicited by Electrical Stimulation of the Midbrain in the Salamander *Notophthalmus viridescens. The Journal of Neuroscience*, 23:2434–2439, March 2003.

J. Cang and W. O. Friesen. Sensory modification of leech swimming: rhythmic activity of ventral stretch receptors can change intersegmental phase relationships. *The Journal of Neuroscience*, 20(20):7822–7829, 2000.

J. Cang and W. O. Friesen. Model for Intersegmental Coordination of Leech Swimming: Central and Sensory Mechanisms. *Journal of Neurophysiology*, 87(6):2760–2769, June 2002.

R. L. Carroll. *Vertebrate paleontology and evolution*. Freeman, 1988.

J. Cheng, R. B. Stein, K. Jovanovic, K. Yoshida, D. J. Bennett, and Y. Han. Identification, localization, and modulation of neural networks for walking in the mudpuppy (*Necturus Maculatus*) spinal cord. *The Journal of Neuroscience*, 18(11):4295–4304, 1998.

S. Chevallier, A. J. Ijspeert, D. Ryczko, F. Nagy, and J.-M. Cabelguen. Organisation of the spinal central pattern generators for locomotion in the salamander: biology and modelling. *Brain Res Rev*, 57(1):147–61, January 2008.

Y.-C. Chou, W.-S. Yu, K.-J. Huang, and P.-C. Lin. Bio-inspired step-climbing in a hexapod robot. *Bioinspiration & Biomimetics*, 7(3):036008, 2012.

J. A. Clack. An early tetrapod from 'Romer's Gap'. *Nature*, 418(6893):72–76, 2002a.

J. A. Clack. *Gaining ground: the origin and evolution of tetrapods*. Indiana University Press, 2002b.

F. Clarac and E. Pearlstein. Invertebrate preparations and their contribution to neurobiology in the second half of the 20th century. *Brain research reviews*, 54(1):113–161, 2007.

M. Clerc and J. Kennedy. The particle swarm - explosion, stability, and convergence in a multidimensional complex space. *Evolutionary Computation, IEEE Transactions on*, 6(1):58 –73, February 2002.

A. H. Cohen, G. B. Ermentrout, T. Kiemel, N. Kopell, K. A. Sigvardt, and T. L. Williams. Modelling of intersegmental coordination in the lamprey central pattern generator for locomotion. *Trends in Neurosciences*, 15(11):434–438, November 1992. doi: 10.1016/0166-2236(92) 90006-T.

N. Cohen and J. H. Boyle. Swimming at low Reynolds number: a beginners guide to undulatory locomotion. *Contemporary Physics*, 51(2):103–123, March 2010.

A. Crespi and A. J. Ijspeert. Online Optimization of Swimming and Crawling in an Amphibious Snake Robot. *IEEE Transactions on Robotics*, 24(1):75–87, February 2008.

A. Crespi, K. Karakasiliotis, A. Guignard, and A. J. Ijspeert. Salamandra Robotica II: An Amphibious Robot to Study Salamander-Like Swimming and Walking Gaits. *IEEE Transactions on Robotics*, 29(2):308–320, April 2013.

H. Cruse. What mechanisms coordinate leg movement in walking arthropods? *Trends in neurosciences*, 13(1):15–21, 1990.

H. Cruse, V. Dürr, and J. Schmitz. Insect walking is based on a decentralized architecture revealing a simple and robust controller. *Philosophical Transactions of the Royal Society of London A: Mathematical, Physical and Engineering Sciences*, 365(1850):221–250, 2007.

Bibliography

M. A. Daley and A. A. Biewener. Running over rough terrain reveals limb control for intrinsic stability. *Proceedings of the National Academy of Sciences*, 103(42):15681, 2006.

C. J. Dallmann, V. Dürr, and J. Schmitz. Joint torques in a freely walking insect reveal distinct functions of leg joints in propulsion and posture control. In *Proc. R. Soc. B*, volume 283, pages 1–9. The Royal Society, 2016.

H. Dankert, L. Wang, E. D. Hoopfer, D. J. Anderson, and P. Perona. Automated monitoring and analysis of social behavior in *Drosophila*. *Nature methods*, 6(4):297–303, 2009.

K. D'Août and P. Aerts. Kinematics and efficiency of steady swimming in adult axolotls (*Ambystoma mexicanum*). *The Journal of experimental biology*, 200(13):1863–1871, 1997.

S. Daun-Gruhn and A. Büschges. From neuron to behavior: dynamic equation-based prediction of biological processes in motor control. *Biological cybernetics*, 105(1):71–88, 2011.

K. Deb and N. Padhye. Development of efficient particle swarm optimizers by using concepts from evolutionary algorithms. In *Proceedings of the 12th annual conference on Genetic and evolutionary computation*, pages 55–62. ACM, 2010.

F. Delcomyn. Insect walking and robotics. *Annual Reviews in Entomology*, 49(1):51–70, 2004.

I. Delvolvé, T. Bem, and J.-M. Cabelguen. Epaxial and limb muscle activity during swimming and terrestrial stepping in the adult newt, *Pleurodeles Waltl. Journal of Neurophysiology*, 78: 638–650, 1997.

I. Delvolvé, P. Branchereau, R. Dubuc, and J.-M. Cabelguen. Fictive Rhythmic Motor Patterns Induced by NMDA in an In Vitro Brain Stem-Spinal Cord Preparation From an Adult Urodele. *Journal of Neurophysiology*, 82:1074–1077, 1999.

M. H. Dickinson, F.-O. Lehmann, and S. P. Sane. Wing rotation and the aerodynamic basis of insect flight. *Science*, 284(5422):1954–1960, 1999.

M. H. Dickinson, C. T. Farley, R. J. Full, M. A. R. Koehl, R. Kram, and S. Lehman. How animals move: an integrative view. *Science*, 288(5463):100–106, 2000.

Y. Ding, S. S. Sharpe, K. Wiesenfeld, and D. I. Goldman. Emergence of the advancing neuromechanical phase in a resistive force dominated medium. *Proceedings of the National Academy of Sciences*, 110(25):10123–10128, June 2013.

J. L. Edwards. Two Perspectives on the Evolution of the Tetrapod Limb. *American Zoologist*, 29 (1):235–254, January 1989.

T. Eisner and D. J. Aneshansley. Defense by foot adhesion in a beetle (*Hemisphaerota cyanea*). *Proceedings of the National Academy of Sciences*, 97(12):6568–6573, 2000.

Ö. Ekeberg. A combined neuronal and mechanical model of fish swimming. *Biological Cybernetics*, 69(5-6):363–374, 1993.

140

H. El Daou, P.-A. Libourel, S. Renoust, V. Belst, and J.-C. Guinot. *Motion and Force measures on tortoises to design and control a biomimetic quadruped robot.* Springer, 2010.

T. Endlein and W. Federle. Walking on smooth or rough ground: passive control of pretarsal attachment in ants. *Journal of Comparative Physiology A*, 194(1):49–60, 2008.

I. Engberg and A. Lundberg. An Electromyographic Analysis of Muscular Activity in the Hindlimb of the Cat during Unrestrained Locomotion. *Acta Physiologica Scandinavica*, 75 (4):614–630, April 1969.

W. Federle and T. Endlein. Locomotion and adhesion: dynamic control of adhesive surface contact in ants. *Arthropod Structure & Development*, 33(1):67–75, 2004.

W. Federle, M. Riehle, A. S. G. Curtis, and R. J. Full. An integrative study of insect adhesion: mechanics and wet adhesion of pretarsal pads in ants. *Integrative and Comparative Biology*, 42(6):1100–1106, 2002.

H. Fischer, J. Schmidt, R. Haas, and A. Büschges. Pattern Generation for Walking and Searching Movements of a Stick Insect Leg. I. Coordination of Motor Activity. *Journal of Neurophysiology*, 85(1):341–353, January 2001.

M. S. Fischer and R. Lehmann. Application of cineradiography for the metric and kinematic study of in-phase gaits during locomotion of the Pika (Ochotona Rufescens, Mammalia: Lago Morpha). *Zoology*, 101(3):148–173, 1998.

D. Floreano and L. Keller. Evolution of adaptive behaviour in robots by means of Darwinian selection. *PLoS Biol*, 8(1):e1000292, 2010.

D. Floreano and C. Mattiussi. *Bio-inspired artificial intelligence: theories, methods, and technologies.* MIT press, 2008.

D. Floreano, A. J. Ijspeert, and S. Schaal. Robotics and Neuroscience. *Current Biology*, 24(18): R910–R920, 2014.

H. Forssberg. Stumbling corrective reaction: a phase-dependent compensatory reaction during locomotion. *Journal of Neurophysiology*, 42(4):936–953, July 1979.

V. French, M. Feast, and L. Partridge. Body size and cell size in *Drosophila*: the developmental response to temperature. *Journal of Insect Physiology*, 44(11):1081–1089, 1998.

W. O. Friesen and J. Cang. Sensory and central mechanisms control intersegmental coordination. *Current Opinion in Neurobiology*, 11(6):678–683, December 2001.

R. J. Full. Invertebrate locomotor systems. *Comprehensive Physiology*, 1997.

R. J. Full and D. E. Koditschek. Templates and anchors: neuromechanical hypotheses of legged locomotion on land. *Journal of Experimental Biology*, 202(23):3325–3332, 1999.

Bibliography

R. J. Full and M. S. Tu. Mechanics of six-legged runners. *Journal of experimental biology*, 148 (1):129–146, 1990.

R. J. Full and M. S. Tu. Mechanics of a rapid running insect: two-, four-and six-legged locomotion. *Journal of Experimental Biology*, 156(1):215–231, 1991.

R. J. Full, R. Blickhan, and L. H. Ting. Leg design in hexapedal runners. *Journal of Experimental Biology*, 158(1):369–390, 1991.

K.-Q. Gao and N. H. Shubin. Late Jurassic salamanders from northern China. *Nature*, 410 (6828):574–577, 2001.

S. M. Gatesy and A. A. Biewener. Bipedal locomotion: effects of speed, size and limb posture in birds and humans. *Journal of Zoology*, 224(1):127–147, 1991.

B. J. Gemmell, S. P. Colin, J. H. Costello, and J. O. Dabiri. Suction-based propulsion as a basis for efficient animal swimming. *Nature Communications*, 6, November 2015.

H. Geyer and H. Herr. A Muscle-Reflex Model That Encodes Principles of Legged Mechanics Produces Human Walking Dynamics and Muscle Activities. *Neural Systems and Rehabilitation Engineering, IEEE Transactions on*, 18(3):263–273, 2010.

T. C. Gillmer. *Introduction to naval architecture*. Springer Science & Business Media, 2012.

V. v. Ginneken, E. Antonissen, U. K. Müller, R. Booms, E. Eding, J. Verreth, and G. v. d. Thillart. Eel migration to the Sargasso: remarkably high swimming efficiency and low energy costs. *Journal of Experimental Biology*, 208(7):1329–1335, April 2005.

D. I. Goldman, T. S. Chen, D. M. Dudek, and R. J. Full. Dynamics of rapid vertical climbing in cockroaches reveals a template. *Journal of Experimental Biology*, 209(15):2990–3000, 2006.

D. Graham. A behavioural analysis of the temporal organisation of walking movements in the 1st instar and adult stick insect (*Carausius morosus*). *Journal of Comparative Physiology*, 81 (1):23–52, 1972.

J. Gray. *Animal locomotion*. Weidenfeld & Nicolson London, 1968.

S. Grillner and P. Wallén. Central Pattern Generators for Locomotion, with Special Reference to Vertebrates. *Annual Review of Neuroscience*, 8(1):233–261, 1985.

S. Grillner, A. McClellan, K. Sigvardt, P. Wallén, and M. Wilen. Activation of NMDA-receptors elicits "Fictive locomotion" in lamprey spinal cord in vitro. *Acta physiologica Scandinavica*, 113(4):549–551, 1981.

S. Grillner, T. Williams, and P. A. Lagerback. The edge cell, a possible intraspinal mechanoreceptor. *Science*, 223(4635):500–503, February 1984.

S. Grillner, T. Degliana, Ö. Ekeberg, A. El Manira, A. Lansner, G. N. Orlovsky, and P. Wallén. Neural networks that co-ordinate locomotion and body orientation in lamprey. *Trends in Neuroscience*, 18(6):270–279, 1995.

J. A. Grimes and J. W. Hurst. The design of ATRIAS 1.0 a unique monopod, hopping robot. In *Proceedings of the Fifteenth International Conference on Climbing and Walking Robots and the Support Technologies for Mobile Machines*, pages 548–554, Baltimore, MD, USA, July 2012.

Z. V. Guo and L. Mahadevan. Limbless undulatory propulsion on land. *Proceedings of the National Academy of Sciences*, 105(9):3179–3184, March 2008.

F. Haas and S. Gorb. Evolution of locomotory attachment pads in the Dermaptera (Insecta). *Arthropod structure & development*, 33(1):45–66, 2004.

M. Haehnel-Taguchi, O. Akanyeti, and J. C. Liao. Afferent and motoneuron activity in response to single neuromast stimulation in the posterior lateral line of larval zebrafish. *Journal of Neurophysiology*, 112(6):1329–1339, September 2014.

N. C. Heglund, C. R. Taylor, and T. A. McMahon. Scaling stride frequency and gait to animal size: mice to horses. *Science*, 186(4169):1112–1113, 1974.

M. Hildebrand. Symmetrical Gaits of Horses. *Science*, 150(3697):701–708, 1965.

S. F. Hoerner. *Fluid-dynamic drag: practical information on aerodynamic drag and hydrodynamic resistance*. Hoerner Fluid Dynamics Midland Park, NJ, 1965.

P. Holmes, R. J. Full, D. Koditschek, and J. Guckenheimer. The dynamics of legged locomotion: Models, analyses, and challenges. *Siam Review*, 48(2):207–304, 2006.

A. M. Hoover, E. Steltz, and R. S. Fearing. RoACH: An autonomous 2.4 g crawling hexapod robot. In *2008 IEEE/RSJ International Conference on Intelligent Robots and Systems*, pages 26–33. IEEE, 2008.

A. B. Howell. Speed in animals. 1944. URL http://agris.fao.org/agris-search/search.do?recordID=US201300223136.

D. F. Hoyt and C. R. Taylor. Gait and the energetics of locomotion in horses. *Nature*, 292: 239–240, 1981.

L.-J. Hsu, P. V. Zelenin, S. Grillner, G. N. Orlovsky, and T. G. Deliagina. Intraspinal stretch receptor neurons mediate different motor responses along the body in lamprey. *Journal of Comparative Neurology*, 521(16):3847–3862, 2013.

D. L. Hu, B. Chan, and J. W. M. Bush. The hydrodynamics of water strider locomotion. *Nature*, 424(6949):663–666, 2003.

Bibliography

G. M. Hughes. The co-ordination of insect movements. *Journal of Experimental Biology*, 29(2): 267–285, 1952.

M. Hüsken, K. Hufnagel, K. Mende, E. Appel, H. Meyer, H. Peisker, M. Tögel, S. Wang, J. Wolff, S. N. Gorb, and Paululat, A. Adhesive pad differentiation in *Drosophila melanogaster* depends on the Polycomb group gene Su (z) 2. *Journal of Experimental Biology*, 218(8): 1159–1165, 2015.

A. J. Ijspeert. A connectionist central pattern generator for the aquatic and terrestrial gaits of a simulated salamander. *Biological Cybernetics*, 84(5):331–348, 2001.

A. J. Ijspeert. Biorobotics: Using robots to emulate and investigate agile locomotion. *Science*, 346(6206):196–203, 2014.

A. J. Ijspeert, A. Crespi, D. Ryczko, and J.-M. Cabelguen. From swimming to walking with a salamander robot driven by a spinal cord model. *Science*, 315(5817):1416–20, March 2007.

D. G. Ivashko, B. I. Prilutsky, S. N. Markin, J. K. Chapin, and I. A. Rybak. Modeling the spinal cord neural circuitry controlling cat hindlimb movement during locomotion. *Neurocomputing*, 52:621–629, 2003.

T. Iwasaki, J. Chen, and W. O. Friesen. Biological clockwork underlying adaptive rhythmic movements. *Proceedings of the National Academy of Sciences*, 111(3):978–983, 2014.

R. Jander. Insect orientation. *Annual Review of Entomology*, 8(1):95–114, 1963.

L. C. Johansson and G. V. Lauder. Hydrodynamics of surface swimming in leopard frogs (*Rana pipiens*). *Journal of experimental biology*, 207(22):3945–3958, 2004.

K. Karakasiliotis. *Legged locomotion with spinal undulations*. PhD thesis, École polytechnique fédérale de Lausanne EPFL, 2013. URL http://infoscience.epfl.ch/record/182934?ln=en.

K. Karakasiliotis and A. J. Ijspeert. Analysis of the terrestrial locomotion of a salamander robot. In *IEEE/RSJ International Conference on Intelligent Robots and Systems, 2009. IROS 2009*, pages 5015–5020, October 2009. doi: 10.1109/IROS.2009.5354220.

K. Karakasiliotis, N. Schilling, J.-M. Cabelguen, and A. J. Ijspeert. Where are we in understanding salamander locomotion: biological and robotic perspectives on kinematics. *Biol Cybern*, December 2012.

S. M. Kawano and R. W. Blob. Propulsive forces of mudskipper fins and salamander limbs during terrestrial locomotion: implications for the invasion of land. *Integrative and comparative biology*, 53(2):283–294, 2013.

D. Kennedy and W. J. Davis. Organization of invertebrate motor systems. *Comprehensive Physiology*, 1977.

J. Knuesel. *Modeling a diversity of salamander motor behaviors with coupled abstract oscillators and a robot.* Doctoral thesis, Ecole Polytechnique Federale de Lausanne (EPFL), 2013.

J. Knüsel, A. Bicanski, D. Ryczko, J.-M. Cabelguen, and A. J. Ijspeert. A salamander's flexible spinal network for locomotion, modeled at two levels of abstraction. *Integrative and Comparative Biology*, 2013.

J. Korta, D. A. Clark, C. V. Gabel, L. Mahadevan, and A. D. T. Samuel. Mechanosensation and mechanical load modulate the locomotory gait of swimming *C. elegans* . *Journal of Experimental Biology*, 210(13):2383–2389, 2007.

M. Kragl, D. Knapp, E. Nacu, S. Khattak, M. Maden, H. H. Epperlein, and E. M. Tanaka. Cells keep a memory of their tissue origin during axolotl limb regeneration. *Nature*, 460(7251): 60–65, July 2009.

A. Kumar and A. Simon, editors. *Salamanders in Regeneration Research*, volume 1290 of *Methods in Molecular Biology*. Springer New York, New York, NY, 2015. ISBN 978-1-4939-2494-3 978-1-4939-2495-0.

A. D. Kuo. The Relative Roles of Feedforward and Feedback in the Control of Rhythmic Movements. *Motor Control*, 6(2):129–145, April 2002.

J. C. Liao. Neuromuscular control of trout swimming in a vortex street: implications for energy economy during the Kármán gait. *Journal of Experimental Biology*, 207(20):3495–3506, September 2004.

J. C. Liao, D. N. Beal, G. V. Lauder, and M. S. Triantafyllou. Fish Exploiting Vortices Decrease Muscle Activity. *Science*, 302(5650):1566–1569, November 2003.

T. Libby, T. Y. Moore, E. Chang-Siu, D. Li, D. J. Cohen, A. Jusufi, and R. J. Full. Tail-assisted pitch control in lizards, robots and dinosaurs. *Nature*, 481(7380):181–184, 2012.

M. J. Lighthill. Large-amplitude elongated-body theory of fish locomotion. *Proceedings of the Royal Society of London B: Biological Sciences*, 179(1055):125–138, 1971.

R. D. Maladen, Y. Ding, C. Li, and D. I. Goldman. Undulatory swimming in sand: subsurface locomotion of the sandfish lizard. *Science*, 325(5938):314–318, 2009.

H. Marvi, C. Gong, N. Gravish, H. Astley, M. Travers, R. L. Hatton, J. R. Mendelson, H. Choset, D. L. Hu, and D. I. Goldman. Sidewinding with minimal slip: Snake and robot ascent of sandy slopes. *Science*, 346(6206):224–229, 2014.

T. Matsushima and S. Grillner. Neural mechanisms of intersegmental coordination in lamprey: local excitability changes modify the phase coupling along the spinal cord. *Journal of Neurophysiology*, 67(2):373–388, February 1992.

Bibliography

T. McMillen, T. Williams, and P. Holmes. Nonlinear Muscles, Passive Viscoelasticity and Body Taper Conspire To Create Neuromechanical Phase Lags in Anguilliform Swimmers. *PLOS Computational Biology*, 4(8):e1000157, August 2008.

C. S. Mendes, I. Bartos, T. Akay, S. Márka, and R. S. Mann. Quantification of gait parameters in freely walking wild type and sensory deprived *Drosophila melanogaster* . *eLife*, 2, 2013.

C. S. Mendes, S. V. Rajendren, I. Bartos, S. Márka, and R. S. Mann. Kinematic responses to changes in walking orientation and gravitational load in *Drosophila melanogaster*. *PloS one*, 9(10):e109204, 2014.

T. Merton. On a barrier against insect pests. *Proceedings of the Royal Society of London. Series A, Mathematical and Physical Sciences*, pages 218–220, 1956.

O. Michel. Webots: Professional Mobile Robot Simulation. *International Journal of Advanced Robotic Systems*, 1:39–42, 2004.

D. L. Miranda, M. J. Rainbow, J. J. Crisco, and B. C. Fleming. Kinematic differences between optical motion capture and biplanar videoradiography during a jump–cut maneuver. *Journal of Biomechanics*, 46(3):567–573, February 2013.

M. Moonesun, M. Javadi, P. Charmdooz, and K. U. Mikhailovich. Evaluation of submarine model test in towing tank and comparison with CFD and experimental formulas for fully submerged resistance. *Indian Journal of Geo-Marine Sciences*, 42(8):1049–1056, 2013.

P. Moretto, P. Pelayo, and M. A. Lafortune. The use of Froude's numbers to normalize human gait. In *Proceedings Of The Ninth Biennial Conference And Symposia: Simon Fraser University*, page 274, 1996.

E. Muybridge. *Animal Locomotion: An Electrophotographic Investigation of Consecutive Phases of Animal Movements*. University of Pennsylvania, 1887.

E. Niebur and P. Erdös. Theory of the locomotion of nematodes: dynamics of undulatory progression on a surface. *Biophysical journal*, 60(5):1132, 1991.

D. Owaki, T. Kano, K. Nagasawa, A. Tero, and A. Ishiguro. Simple robot suggests physical interlimb communication is essential for quadruped walking. *Journal of The Royal Society Interface*, 10(78), 2013.

F. M. Petti, M. Bernardi, M. A. Ashley-Ross, F. Berra, A. Tessarollo, and M. Avanzini. Transition between terrestrial-submerged walking and swimming revealed by Early Permian amphibian trackways and a new proposal for the nomenclature of compound trace fossils. *Palaeogeography, Palaeoclimatology, Palaeoecology*, 410:278–289, 2014.

C. Phelan, J. Tangorra, G. Lauder, and M. Hale. A biorobotic model of the sunfish pectoral fin for investigations of fin sensorimotor control. *Bioinspiration & biomimetics*, 5(3), 2010.

M. Porez, F. Boyer, and A. J. Ijspeert. Improved Lighthill fish swimming model for bio-inspired robots: Modeling, computational aspects and experimental comparisons. *The International Journal of Robotics Research*, 33(10):1322–1341, September 2014.

G. Pratt and M. M. Williamson. Series elastic actuators. In *Intelligent Robots and Systems 95.'Human Robot Interaction and Cooperative Robots', Proceedings. 1995 IEEE/RSJ International Conference on*, volume 1, pages 399–406. IEEE, 1995.

P. Ramdya, P. Lichocki, S. Cruchet, L. Frisch, W. Tse, D. Floreano, and R. Benton. Mechanosensory interactions drive collective behaviour in *Drosophila*. *Nature*, 519(7542):233–236, 2015.

L. Reinhardt and R. Blickhan. Level locomotion in wood ants: evidence for grounded running. *Journal of Experimental Biology*, 217(13):2358–2370, 2014.

L. Reinhardt, T. Weihmann, and R. Blickhan. Dynamics and kinematics of ant locomotion: do wood ants climb on level surfaces? *Journal of Experimental Biology*, 212(15):2426–2435, 2009.

L. Ristroph, J. C. Liao, and J. Zhang. Lateral Line Layout Correlates with the Differential Hydrodynamic Pressure on Swimming Fish. *Physical Review Letters*, 114(1):018102, January 2015.

A. S. Romer and F. Byrne. The pes of *Diadectes*: notes on the primitive tetrapod limb. *Palaeobiologica*, 4:25–48, 1931.

I. A. Rybak, D. G. Ivashko, B. I. Prilutsky, M. A. Lewis, and J. K. Chapin. Modeling neural control of locomotion: integration of reflex circuits with CPG. In *International Conference on Artificial Neural Networks*, pages 99–104. Springer, 2002.

D. Ryczko, V. Charrier, A. J. Ijspeert, and J.-M. Cabelguen. Segmental oscillators in axial motor circuits of the salamander: distribution and bursting mechanisms. *J Neurophysiol*, 104(5): 2677–92, November 2010. doi: 10.1152/jn.00479.2010.

D. Ryczko, J. Knüsel, A. Crespi, S. Lamarque, A. Mathou, A. J. Ijspeert, and J. M. Cabelguen. Flexibility of the axial central pattern generator network for locomotion in the salamander. *Journal of Neurophysiology*, 113(6):1921–1940, March 2015.

U. Saranli, M. Buehler, and D. E. Koditschek. RHex: A simple and highly mobile hexapod robot. *The International Journal of Robotics Research*, 20(7):616–631, 2001.

P. L. Schaefer, G. V. Kondagunta, and R. E. Ritzmann. Motion analysis of escape movements evoked by tactile stimulation in the cockroach *Periplaneta americana*. *Journal of experimental biology*, 190(1):287–294, 1994.

B. Schaeffer. The morphological and functional evolution of the tarsus in amphibians and reptiles. *Bulletin of the American Museum of Natural History*, 78(article 6.), 1941.

Bibliography

M. Schilling, T. Hoinville, J. Schmitz, and H. Cruse. Walknet, a bio-inspired controller for hexapod walking. *Biological cybernetics*, 107(4):397–419, 2013.

J. Schmidt. The Breeding Places of the Eel. *Philosophical Transactions of the Royal Society of London. Series B, Containing Papers of a Biological Character*, 211:179–208, 1923.

J. Schmitt and P. Holmes. Mechanical models for insect locomotion: active muscles and energy losses. *Biological cybernetics*, 89(1):43–55, 2003.

J. Schmitz, J. Dean, T. Kindermann, M. Schumm, and H. Cruse. A biologically inspired controller for hexapod walking: simple solutions by exploiting physical properties. *The biological bulletin*, 200(2):195–200, 2001.

A. Schneider, H. Cruse, and J. Schmitz. Decentralized control of elastic limbs in closed kinematic chains. *The International Journal of Robotics Research*, 25(9):913–930, 2006.

J. S. Schwarz, T. Reichenbach, and A. J. Hudspeth. A hydrodynamic sensory antenna used by killifish for nocturnal hunting. *Journal of Experimental Biology*, 214(11):1857–1866, 2011.

M. Sfakiotakis, D. M. Lane, and J. B. C. Davies. Review of fish swimming modes for aquatic locomotion. *Oceanic Engineering, IEEE Journal of*, 24(2):237–252, 1999.

K. Sims. Evolving 3d Morphology and Behavior by Competition. *Artificial Life*, 1(4):353–372, July 1994.

H. Sink. *Muscle Development in Drosophilia*. Springer, 2007.

J. Smolka, M. J. Byrne, C. H. Scholtz, and M. Dacke. A new galloping gait in an insect. *Current Biology*, 23(20):R913–R915, 2013.

R. E. Snodgrass. Principles of insect morphology. *McGraw-Hill Book Co.*, 1935.

C. Soler, M. Daczewska, J. P. Da Ponte, B. Dastugue, and K. Jagla. Coordinated development of muscles and tendons of the *Drosophila* leg. *Development*, 131(24):6041–6051, 2004.

A. J. Spence. Scaling in biology. *Current Biology*, 19(2):R57–R61, 2009.

A. Spröwitz, A. Tuleu, M. Vespignani, M. Ajallooeian, E. Badri, and A. J. Ijspeert. Towards dynamic trot gait locomotion: Design, control, and experiments with Cheetah-cub, a compliant quadruped robot. *The International Journal of Robotics Research*, 32(8):932–950, 2013.

M. Srinivasan and A. Ruina. Computer optimization of a minimal biped model discovers walking and running. *Nature*, 439:72–75, 2005.

R. Strauss and M. Heisenberg. Coordination of legs during straight walking and turning in Drosophila melanogaster. *Journal of comparative physiology a: neuroethology, sensory, neural, and behavioral physiology*, 167(3):403–412, 1990.

N. S. Szczecinski, A. E. Brown, J. A. Bender, R. D. Quinn, and R. E. Ritzmann. A neuromechanical simulation of insect walking and transition to turning of the cockroach *Blaberus discoidalis*. *Biological cybernetics*, 108(1):1–21, 2014.

J. Sznitman, P. K. Purohit, P. Krajacic, T. Lamitina, and P. E. Arratia. Material Properties of Caenorhabditis elegans Swimming at Low Reynolds Number. *Biophysical Journal*, 98(4): 617–626, February 2010.

A. E. Talpalar, J. Bouvier, L. Borgius, G. Fortin, A. Pierani, and O. Kiehn. Dual-mode operation of neuronal networks involved in left-right alternation. *Nature*, 500(7460):85–88, 2013.

G. K. Taylor, R. L. Nudds, and A. L. R. Thomas. Flying and swimming animals cruise at a Strouhal number tuned for high power efficiency. *Nature*, 425(6959):707–711, 2003.

L. H. Ting, R. Blickhan, and R. J. Full. Dynamic and static stability in hexapedal runners. *Journal of Experimental Biology*, 197(1):251–269, 1994.

M. S. Triantafyllou and G. S. Triantafyllou. An efficient swimming machine. *Scientific american*, 272(3):64–71, 1995.

N. G. Tsagarakis, S. Morfey, G. M. Cerda, L. Zhibin, and D. G. Caldwell. Compliant humanoid coman: Optimal joint stiffness tuning for modal frequency control. In *Robotics and Automation (ICRA), 2013 IEEE International Conference on*, pages 673–678. IEEE, 2013.

E. D. Tytell, C.-Y. Hsu, T. L. Williams, A. H. Cohen, and L. J. Fauci. Interactions between internal forces, body stiffness, and fluid environment in a neuromechanical model of lamprey swimming. *Proc Natl Acad Sci U S A*, 107(46):19832–7, November 2010.

R. Venturelli, O. Akanyeti, F. Visentin, J. Ježov, L. D. Chambers, G. Toming, J. Brown, M. Kruusmaa, W. M. Megill, and P. Fiorini. Hydrodynamic pressure sensing with an artificial lateral line in steady and unsteady flows. *Bioinspiration & biomimetics*, 7(3):036004, 2012.

V. Wahl, S. E. Pfeffer, and M. Wittlinger. Walking and running in the desert ant *Cataglyphis fortis*. *Journal of Comparative Physiology A*, 201(6):645–656, 2015.

Q. Wen, M. D. Po, E. Hulme, S. Chen, X. Liu, S. W. Kwok, M. Gershow, A. M. Leifer, V. Butler, C. Fang-Yen, and others. Proprioceptive coupling within motor neurons drives C. elegans forward locomotion. *Neuron*, 76(4):750–761, 2012.

A. J. Wiens. *Gait optimization for a multilink anguilliform swimmer*. Master Thesis, McGill University, Montreal, 2013.

D. M. Wilson. Insect walking. *Annual review of entomology*, 11(1):103–122, 1966.

S. Wischmann, D. Floreano, and L. Keller. Historical contingency affects signaling strategies and competitive abilities in evolving populations of simulated robots. *Proceedings of the National Academy of Sciences*, 109(3):864–868, 2012.

Bibliography

R. D. Worthington and D. B. Wake. Patterns of regional variation in the vertebral column of terrestrial salamanders. *Journal of Morphology*, 137(3):257–277, 1972.

A. Wosnitza, T. Bockemühl, M. Dübbert, H. Scholz, and A. Büschges. Inter-leg coordination in the control of walking speed in *Drosophila. Journal of experimental biology*, 216(3):480–491, 2013.

X. Yu, B. Nguyen, and W. O. Friesen. Sensory Feedback Can Coordinate the Swimming Activity of the Leech. *The Journal of Neuroscience*, 19(11):4634–4643, June 1999.

C. Zollikofer. Stepping patterns in ants-influence of body morphology. *Journal of experimental biology*, 192(1):107–118, 1994.

ROBIN THANDIACKAL

Contact Info

Address:	Route de la Plaine 5, 1022 Chavannes/Renens, Switzerland
Phone:	+41 76 399 32 76
Email:	rthandiackal@gmail.com

Fields of Interest

Robotics, Optimization, Decentralized control, Central Pattern Generators, Undulatory swimming

Education

ETH Lausanne, Switzerland – PhD, 2012-2017

Biorobotics Laboratory, Focus: Robotics, Optimization

Exploring topics of locomotion control in different environments, optimizations for gait patterns of a simulated insect model, implementation of pressure feedback mechanisms for a swimming robot, and contributions on the design and evaluation of an amphibious robot. Keywords: Optimization, mathematical modelling, programming, experimental design

ETH Zürich, Switzerland – MSc, 2010-2012

Mechanical Engineering, Focus: Robotics, Image segmentation

Semester thesis on class-based image segmentation algorithm, Master thesis on (energy) optimal control strategy for a throwing task. Keywords: Image segmentation, optimal control

ETH Zürich, Switzerland – BSc, 2007-2010

Mechanical Engineering, Focus: Robotics

Bachelor project involving strain gauge control for improvement of climbing abilities of an autonomous magnetic-wheeled robot. Keywords: Sensor characterization, programming

Professional Experience

Developer, Sensirion AG, Stäfa, Switzerland – June-September 2010

Data analysis software: Extension and maintenance of a Python framework for the evaluation of humidity and temperature sensors. Implementation of visualization tools to identify and improve sensor characteristics. Keywords: Python-programming, Data evaluation and visualization.

Teaching Experience

Main research assistant, EPFL, Switzerland – 2014, 2015, 2016

Teaching: Preparation of course material including a simulation environment with corresponding optimization tools and assistance of students during the practical sessions. Keywords: Code debugging, Project design and evaluation

Semester and Bachelor projects, EPFL, Switzerland – 2012-2016

Supervision: Assistance and supervision of 5 Semester projects and 1 Bachelor project.

Competences

Programming, Data analysis, Optimization, mathematical modelling, estimation, Rigid body simulation, Image segmentation, Computer vision, public speaking, team leading

List of publications

P. Ramdya, <u>R. Thandiackal*</u>, R. Cherney, T. Asselborn, R. Benton, A. J. Ijspeert, D. Floreano. Climbing favours the tripod gait over alternative faster insect gaits. Nature Communications, 2017

D. Ryczko, <u>R. Thandiackal</u> and A. Ijspeert. Interfacing a salamander brain with a salamander-like robot: Control of speed and direction with calcium signals from brainstem reticulospinal neurons. 2016 6th IEEE International Conference on Biomedical Robotics and Biomechatronics (BioRob), Singapore, Singapore, 2016.

K. Karakasiliotis, <u>R. Thandiackal</u>, K. Melo, T. Horvat and N. K. Mahabadi et al. From cineradiography to biorobots: an approach for designing robots to emulate and study animal locomotion, in Journal of The Royal Society Interface, vol. 13, num. 119, 2016.

T. Horvat, K. Karakasiliotis, K. Melo, L. Fleury and <u>R. Thandiackal</u> et al. Inverse kinematics and reflex based controller for body-limb coordination of a salamander-like robot walking on uneven terrain. 2015 IEEE/RSJ International Conference on Intelligent Robots and Systems (IROS), Hamburg, Germany, 2015.

<u>R. Thandiackal</u>, C. Brandle, D. Leach, A. Jafari and F. Iida. Exploiting passive dynamics for robot throwing task. 2012 IEEE/RSJ International Conference on Intelligent Robots and Systems (IROS 2012), Vilamoura-Algarve, Portugal, 2012.

<u>R. Thandiackal</u>, M. Prasad and V. Ferrari (Dirs.). Deformable shape models for 2D object segmentation, 2011.

Achievements

2015: Participation at TED Global event Geneva with Prof. Ijspeert
2015: Presenter at Bay Area Science Festival San Francisco to promote Robotics from Switzerland
2013: Presenter at Robot Safari in London Science Museum
2001: Passed entrance exam for Untergymnasium (50 places numerus clausus)

Extracurricular activities

Sports: Co-founder of a football club, running, basketball, squash, handball, frisbee; playing the guitar, engaging in discussions about movies and TV-shows

Programming

C, C++, Matlab, Python, SQL

Tools

Git, SVN, Webots, Solidworks, NX, Latex, Inkscape, Adobe Premier Pro

Languages

German: native,
English: fluent,
French: good,
Malayalam: good (spoken)

Personal

Born November 1988, Swiss